

**Non-collinear  
optical parametric oscillator  
for stimulated Raman spectroscopy  
in real-time**

Von der Fakultät für Mathematik und Physik  
der Gottfried Wilhelm Leibniz Universität Hannover

zur Erlangung des akademischen Grades  
**Doktor der Naturwissenschaften**

– Dr. rer. nat. –

genehmigte Dissertation von

**Luise Beichert**

2023



Referent	Prof. Dr. Uwe Morgner
Korreferent	Prof. Dr. Bernhard Roth
Korreferent	Associate Professor Dario Polli
Tag der Promotion	14.04.2023



# Kurzfassung

Luise Beichert

## Stimulierte Ramanspektroskopie in Echtzeit mit einem nicht-kollinearem optisch parametrischen Oszillator

Die stimulierte Ramanspektroskopie ist ein leistungsfähiges, chemisches Analyseverfahren, welches durch gezielte Anregung eines molekularen Vibrationsübergangs Informationen über die zu untersuchende Materialzusammensetzung liefert. Wie ein Fingerabdruck unterscheiden sich die Ramanspektren verschiedener Moleküle. Im Gegensatz zur spontanen Ramanspektroskopie, welche auf inelastischer Streuung mit geringem Wirkungsgrad basiert, handelt es sich bei der stimulierten Ramanspektroskopie um einen kohärenten, physikalischen Prozess. Durch die gleichzeitige Einstrahlung zweier Laserstrahlen und der Bedingung, dass deren Differenzfrequenz genau der Übergangsfrequenz des Moleküls entspricht, wird der Vibrationszustand mit hoher Wahrscheinlichkeit angeregt. Die Intensitätsänderung der Eingangsstrahlung gibt Aufschluss über die Stärke des Ramanübergangs. Zum Abfragen breiter Spektralbereiche wird eine Lichtquelle mit verstimmbarer Wellenlänge benötigt.

Im Rahmen dieser Dissertation wird ein nicht-kollinearer optisch parametrischer Oszillator (NOPO) für die stimulierte Ramanspektroskopie erprobt. Die Lichtquelle zeichnet sich durch ihr besonders schnelles und schmalbandiges Durchstimmverhalten aus. Sie erlaubt die Echtzeitaufnahme von Ramanspektren über einen großen Wellenzahlbereich von mehr als  $2000\text{ cm}^{-1}$  in 8 ms. Die erforderlichen Phasenanpassungsbedingungen im nichtlinearen Kristall, sowie der Einfluss der Dispersion auf die Ausgangsspektren werden detailliert in dieser Arbeit behandelt.

Darüber hinaus erlaubt der NOPO in Kombination mit der stimulierten Ramanspektroskopie die Echtzeitbeobachtung von Stoffgemischen. So wird die Veränderung eines Wasser-Alkohol-Gemisches live überwacht. Ferner können Mikroplastikpartikel nachgewiesen werden. Die winzigen Plastikteilchen sind in unserer modernen Gesellschaft allgegenwärtig. Trotzdem fehlt es an zuverlässigen und einheitlichen Detektionsmethoden. Der NOPO erweist sich als vielversprechende Lichtquelle, um Proben ohne große Aufbereitung in Echtzeit auf Mikroplastik zu untersuchen. Im Rahmen dieser Arbeit wurden neben makroskopischen Plastikproben sich bewegende  $50\text{ }\mu\text{m}$  bis  $160\text{ }\mu\text{m}$  große Polyamidpartikel direkt in einer wassergefüllten Küvette detektiert.

**Schlagwörter:** Optisch parametrische Oszillatoren, stimulierte Ramanspektroskopie, Mikroplastik

## Abstract

Luise Beichert

### **Stimulated Raman scattering spectroscopy in real-time with a non-collinear optical parametric oscillator**

Stimulated Raman spectroscopy is a powerful chemical analysis technique that provides information about the investigated material composition by selectively stimulating a molecular vibrational transition. Like a fingerprint, the Raman spectra of various molecules differ. In contrast to spontaneous Raman spectroscopy, which is based on inelastic scattering with low efficiency, stimulated Raman spectroscopy is a coherent process. The simultaneous irradiation of two laser beams under the condition that their difference frequency is exactly the same as the transition frequency of the molecule excites the vibrational state with high probability. The intensity change of the input radiation provides information about the strength of the Raman transition. To interrogate broad spectral regions, a light source with a tunable wavelength is required.

In this dissertation, a non-collinear optical parametric oscillator (NOPO) is evaluated for stimulated Raman spectroscopy. The light source is characterized by its particularly fast and narrowband tuning behavior. It allows real-time recording of Raman spectra over a large wavenumber range of more than  $2000\text{ cm}^{-1}$  in 8 ms. In this work, the required phase matching conditions in the nonlinear crystal, as well as the influence of the dispersion on the output spectra, are discussed in detail.

Furthermore, the NOPO in combination with stimulated Raman spectroscopy allows real-time observation of mixtures of substances. For instance, the change of a water-alcohol mixture is monitored live. Furthermore, microplastic particles are detected. The tiny plastic particles are ubiquitous in our modern society. Nevertheless, there is a lack of reliable and consistent detection methods. The NOPO proves to be a promising light source to analyze samples for microplastics in real-time without extensive preparation. In this work, along with macroscopic plastic samples, moving  $50\text{ }\mu\text{m}$  to  $160\text{ }\mu\text{m}$  sized polyamide particles were detected directly in a water-filled cuvette.

**Keywords:** Optical Parametric Oscillators, Stimulated Raman Spectroscopy, Microplastics

# Contents

Kurzfassung . . . . .	i
Abstract . . . . .	ii
List of Tables . . . . .	vi
List of Figures . . . . .	vii
<b>1 Introduction</b>	<b>1</b>
1.1 Motivation . . . . .	1
1.2 Overview . . . . .	2
<b>2 Theoretical Aspects of Optical Parametric Processes</b>	<b>5</b>
2.1 Optical parametric generation . . . . .	6
2.1.1 Optical parametric processes . . . . .	7
2.1.2 Optical Parametric Gain . . . . .	8
2.2 Phase-matching . . . . .	11
2.2.1 Birefringent Phase-matching . . . . .	11
2.2.2 Quasi-Phase-Matching . . . . .	13
2.2.3 Collinear vs. Non-collinear Phase-Matching . . . . .	14
2.3 Tuning of Optical Parametric Oscillators . . . . .	16
2.3.1 Collinear Tuning . . . . .	17
2.3.2 Non-collinear Tuning . . . . .	17
<b>3 Experimental realization of a Non-collinear Optical Parametric Oscillator</b>	<b>21</b>
3.1 Tunable OPOs and alternative light sources . . . . .	22
3.2 Experimental setup of the NOPO . . . . .	24
3.3 Experimental results of the NOPO . . . . .	25
3.3.1 Impact of dispersion . . . . .	25
3.3.2 NOPO characteristics . . . . .	28

<b>4</b>	<b>Theoretical Aspects of Stimulated Raman Scattering</b>	<b>31</b>
4.1	Spontaneous Raman Scattering . . . . .	31
4.1.1	Molecular vibrational resonances . . . . .	32
4.1.2	Spontaneous scattering . . . . .	33
4.2	Stimulated Scattering . . . . .	36
4.2.1	Coherent Raman scattering . . . . .	36
4.2.2	The Stimulated Raman scattering process . . . . .	38
<b>5</b>	<b>Experimental realization of a Stimulated Raman Scattering setup</b>	<b>43</b>
5.1	Measurement principle . . . . .	43
5.1.1	Multicolor SRS methods . . . . .	44
5.1.2	Experimental setup . . . . .	46
5.1.3	Measurement procedure . . . . .	47
5.2	Mixing processes in liquids . . . . .	49
5.2.1	SRS on sugar solutions . . . . .	50
5.2.2	SRS on water-isopropanol mixtures . . . . .	51
5.3	SRS of Microplastic Particles . . . . .	53
5.3.1	Overview of common techniques for microplastics analysis . . . . .	54
5.3.2	SRS of static plastic samples . . . . .	57
5.3.3	SRS of microplastics in an aquatic environment . . . . .	58
<b>6</b>	<b>Conclusion</b>	<b>61</b>
<b>7</b>	<b>Outlook</b>	<b>63</b>
<b>A</b>	<b>Optical Parametric Gain</b>	<b>68</b>
<b>B</b>	<b>SRS from the wave equation</b>	<b>70</b>
<b>C</b>	<b>Principle of Lock-In Amplifiers</b>	<b>72</b>
	<b>Bibliography</b>	<b>85</b>
	<b>List of Publications</b>	<b>86</b>
	<b>Curriculum Vitae</b>	<b>89</b>
	<b>Acknowledgements</b>	<b>91</b>



# List of Figures

2.1	DFG energy level diagram and schematics . . . . .	8
2.2	Parametric gain depending on the phase-mismatch and crystal thickness	10
2.3	Uniaxial crystal and index ellipsoid . . . . .	12
2.4	Schematics of collinear and non-collinear PM geometries. . . . .	15
2.5	Simulations of the phase-matching curves in BBO . . . . .	16
2.6	Synchronously pumped NOPO and cavity detuning . . . . .	18
3.1	Spectral coverage of common tunable lasers and OPOs . . . . .	23
3.2	Experimental NOPO setup and simulated beam waist in the cavity . .	25
3.3	Internal cavity group delay and group delay dispersion . . . . .	26
3.4	The tuning behavior of the NOPO with different dispersion . . . . .	27
3.5	Final NOPO characteristic . . . . .	29
4.1	Simplified picture, energy diagram and molecular response of IR absorption	33
4.2	Spontaneous Raman scattering: energy diagrams and frequency domain	35
4.3	Coherent Raman processes: Illustration and energy diagrams . . . . .	38
4.4	Behavior of the nonlinear susceptibility . . . . .	39
4.5	Energy level diagram and illustration of SRS . . . . .	40
5.1	Multicolor SRS methods . . . . .	45
5.2	Experimental SRS setup . . . . .	46
5.3	SRS measurement principle with the NOPO . . . . .	48
5.4	Evaluated SRS spectrum . . . . .	49
5.5	Spectroscopy setup . . . . .	50
5.6	Raman spectra of sucrose-water solutions with different concentrations.	51
5.7	Raman spectra of water-isopropanol mixtures . . . . .	52
5.8	Time series of Raman spectra observing mixing processes . . . . .	53
5.9	Spectroscopy setup for macroscopic plastic pieces . . . . .	57
5.10	SRS-spectra of macroscopic plastic pieces . . . . .	58
5.11	Stimulated Raman spectra on microplastics in an aquatic solution . . .	59
7.1	Phase-matching curves for CSP . . . . .	65

C.1 Sketch and example of lock-in measurement . . . . .	73
C.2 Lock-in amplifier detects noisy input signal . . . . .	73

# List of Tables

2.1	Three exemplary parametric systems in different gain regimes . . . . .	10
2.2	Different types of PM configurations in uniaxial crystals . . . . .	12
4.1	Raman cross sections for typical molecules from our atmosphere . . . . .	36
5.1	Multicolor SRS techniques . . . . .	45
5.2	Analytical spectroscopic techniques for microplastics detection . . . . .	56



# 1 | Introduction

The most important tool to decode the world around us is light. We cannot travel to the stars, but we can capture their light to analyze it. Likewise, we cannot look at an atom under a microscope, but we can examine which part of the light it absorbs or emits. Spectroscopy, the study of interactions between electromagnetic radiation and matter, is what we owe our current scientific understanding of the world. The origin of the word comes from Latin. Spectrum translates as spirit or apparition. Figuratively speaking, an object is not observed directly, but its shadowy image [1]. The first spectroscopic observations started in the early 19th century with the discovery of dark absorption lines in the solar spectrum and of characteristic emission lines, when chemical elements were strongly heated [2]. Over many decades, these discoveries ultimately led to our present understanding of quantum mechanics, with its concept of discrete energy levels. The light from distinct regions in the electromagnetic spectrum interacts with different states in the atoms and molecules under study. For example, transitions in the outer electron shells are excited with visible light, but the ones in the inner shell close to the nuclei with X-rays. An important branch of spectroscopy looks at the vibrational levels in molecules [3]. When the individual atoms in a molecule move with respect to each other, only certain stretching and bending modes are allowed. These vibrational states can either be excited directly in infrared absorption spectroscopy or detected via inelastic scattering, which is called Raman spectroscopy after its discoverer. Since the vibrational levels are unique for each molecule, both spectroscopic methods provide a kind of fingerprint that allows the molecules to be identified. This type of spectroscopy has many applications. Raman spectroscopy is mainly known from biomedical imaging like cancer diagnostics [4]. But it is also widely used in the pharmaceutical [5], cosmetic and food industries [6], as well as in geology and mineralogy [7] or for drug identification [8].

## 1.1 Motivation

A major challenge in our modern society is the occurrence of microplastics in our environment. These tiny plastic particles are found everywhere, not only in the soil, but more importantly in all marine and surface waters worldwide [9]. Of particular concern

is their increasing presence in drinking water [10]. Microplastics cover a wide range of particles with different shapes, sizes and materials. They appear as fragments, fibers or beads with sizes between 1  $\mu\text{m}$  to 5 mm. Due to their diversity, detecting them using established detection and identification processes is a challenge [11]. Current methods allow only for random sampling and are unsuitable for continuously monitoring the water quality. The very common infrared absorption spectroscopy cannot be applied in water. The water signal would cover many spectral lines, making it impossible to identify the plastic samples. In contrast, Raman spectroscopy suffers from long integration times as the inelastic scattering is a rather weak process. To overcome these limitations, stimulated Raman scattering (SRS) can be utilized [12]. It exploits the coherent excitation of the scattering process and results generally in higher signals than in the spontaneous case. However, it places higher demands on the light source. Two synchronized, pulsed laser beams are required, one with fixed frequency and the other with a tunable output spectrum.

This doctoral thesis was part of a collaborative project named OPTIMUS (**O**ptische **E**rkennung von **T**rinkwasserverunreinigungen durch **M**ikroplastik **u**nd **S**purenstoffe). It was funded by the Federal Ministry of Education and Research of Germany. Its aim was to enable continuous monitoring of drinking water flows for microplastics using stimulated Raman spectroscopy. For this purpose, a novel laser source was to be investigated. It requires narrowband output spectra, which in turn can be tuned at high speed over a wide spectral range. As means of choice a noncollinear optical parametric oscillator (NOPO) was chosen. Compared to commercially available parametric oscillators, its novel, fast tuning technique allows for real-time acquisition of SRS-spectra. The main purpose of this work is to explore the rapidly tunable NOPO with sufficiently high output powers and short pulses, as well as to test its broadband parametric radiation in stimulated Raman spectroscopy. The detection of microplastics in an aqueous solution aims to pave the way for sustained monitoring of large water streams in the future.

## 1.2 Overview

This work is divided into two sections. The first one deals with the characteristics of the developed NOPO and the second one covers the spectroscopy application. Both sections are again subdivided into an introductory section, in which the theoretical foundations are reviewed and an experimental part, where the setups and results are presented. Thus, this introduction is followed by an overview of the principles of optical parametric oscillators. In particular, the parametric gain is derived with which it is possible to construct a laser-like light source. Special attention is given to the phase-matching conditions, since they determine the output spectrum of the parametric

oscillator and can be tailored to a specific demand. The particular strength of the developed light source is its fast tunability of the output wavelength over a wide spectral range. This is achieved by broadband noncollinear phase-matching in combination with a fast adjustable gain window. This tuning mechanism is explained in detail. After an overview of alternative, tunable laser sources, the setup and characteristics of the realized NOPO are presented. Special attention is paid to the spectral tuning curve depending on the internal cavity dispersion.

The spectroscopy part starts with the mathematical description of vibrational states in molecules, their excitation via spontaneous Raman scattering and finally its coherent counterpart, the stimulated Raman scattering. In the experimental section, alternative methods for fast stimulated Raman spectroscopy are presented first. After a description of the experimental setup, the measurement procedure is explained. A change of the cavity length of the NOPO causes a shift in the output spectrum. In this way, stimulated Raman spectra can be detected in real-time. This is demonstrated by the observation of different mixing ratios in sugar solutions and alcohol-water mixtures. The Raman intensities of different substances are used to determine their mixing ratio. Finally, the spectroscopic experiments on plastic samples are shown. Besides macroscopic fragments, moving microplastics are detected directly in an aqueous environment. At a rate of 120 spectra per second, a fluid containing particles less than 160  $\mu\text{m}$  in size was observed. This thesis ends with a summary of the achieved results and an outlook on possible improvements on the NOPO, as well as an extension of the spectroscopic applications.





## 2 | Theoretical Aspects of Optical Parametric Processes

Nonlinear optic describes the interaction between intense light fields with matter. It is a vast field that explains many interesting phenomena: from Second-harmonic to High-harmonic generation, from Self-phase modulation to Self-focusing. It finds its application in the creation of new frequencies, in optical signal processing as well as in quantum optics. And likewise in this thesis, nonlinear optic plays an important role in two ways. On the one hand, it forms the basis of the elaborated light source, and on the other hand it generates the measured signals in the spectroscopic experiments.

The first experimental proof of nonlinear optics was published in 1961 with the detection of second harmonic generation [13]<sup>1</sup>. Nowadays, the basics of nonlinear optics are well understood for many years and can be found in a variety of textbooks and review papers. To give a general overview the next sections are limited to the references [15–18]. The goal is to give an impression about the physics involved in femtosecond Optical Parametric Oscillators.

When an electromagnetic field  $\vec{E}(t)$  interacts with matter, the field induces a Lorentz force on the charged particles. The nuclei of the atoms have a much higher mass than the electrons. Therefore, an interaction with high driving frequencies, as it is the case for electromagnetic fields in the visible or infrared spectral regime, influences only the electrons. They in turn, are moving charges that generate an electromagnetic field. The displacement of the electrons is commonly expressed by the polarization  $\vec{P}(t)$ , which characterizes the strength of the dipole moments in dielectric materials. For fields that are weak compared to the binding forces between electrons and nuclei, it is directly proportional to the incident field:  $\vec{P}(t) = \varepsilon_0 \chi^{(1)} \vec{E}(t)$ , with the vacuum permittivity  $\varepsilon_0$  and the linear susceptibility  $\chi^{(1)}$  as material dependent proportionality factor. However, for strong light fields this simple approach is not valid anymore. As the electric field strength approaches that of the binding forces between electrons and nuclei, the field of nonlinear optics is entered. For larger displacements of the electrons, the anharmonic contributions to the binding potential are no longer negligible. They

---

<sup>1</sup>The publication is still well known today, but due to a mistake. The lithographer erased the spot indicating the SHG because he figured it a defect on the photo [14].

need to be added to the polarization as nonlinear corrections. The total polarization is commonly written as power series

$$\vec{P}(t) = \varepsilon_0 \left[ \chi^{(1)} \vec{E}(t) + \chi^{(2)} \vec{E}^2(t) + \chi^{(3)} \vec{E}^3(t) + \dots \right], \quad (2.1)$$

where  $\chi^{(n)}$  represents the  $n$ -th order component of the susceptibility. In general, the polarization and the electric fields are vectors with contributions in all three spatial directions. For simplification, during these theoretical considerations they will be regarded as scalar fields propagating along the  $z$ -axis. The susceptibilities are tensors with increasing complexity. They determine the strength of the nonlinearities and depend on the material and on the direction and polarization of the interacting light fields. To simplify matters, the effective nonlinear coefficient  $d_{\text{eff}} \sim \chi^{(2)}/2$  is introduced, which combines all properties in one value. It needs to be determined individually for each configuration. In the same way, the higher order susceptibilities can be converted to scalar quantities, accounting for the particular conditions.

The next Section 2.1 shows the fundamental principles for optical parametric generation and amplification, which are second-order nonlinear processes. They build the core of the light source presented in Chapter 3. Subsequently, the coherent Raman processes in Chapter 4 result from third-order contributions to the nonlinear polarization.

## 2.1 Optical parametric generation

Compared to a classical laser, which is based on a  $\chi^{(1)}$ -process and an occupation number inversion, an OPO is based on a  $\chi^{(2)}$ -nonlinearity, which exploits the nonlinear polarization. As the laser medium can store the pump energy, it has less requirements on the pump source. In contrast, the OPO itself needs a laser as pump to reach the necessary intensities for the parametric process. However, the spectral output wavelengths of lasers are limited to the existing gain materials. In comparison, OPOs generally offer a more broadband and better tailorable output.

This section explores the relevant second-order nonlinear processes. The optical parametric generation, which produces new frequencies, is one of them. It may arise when two electromagnetic fields interact in a second-order nonlinear medium. As fundamental requirement, the conservation of energy and momentum must be satisfied. Subsequently, an intensity gain, much like that of a classical laser, is derived. In this way, the energy enhancement in parametric amplifiers and oscillators can be described. To give an overview of the achievable orders of magnitude, different parametric systems are compared.

### 2.1.1 Optical parametric processes

The optical parametric generation shows up as a particular form of parametric down-conversion or difference frequency generation. Considering two electromagnetic fields with different frequencies  $\omega_1$  and  $\omega_2$  and their respective amplitudes  $A_1$  and  $A_2$ , the total field in the time domain can be written in complex notation as

$$E(t) = A_1 \exp(-i\omega_1 t) + A_2 \exp(-i\omega_2 t) + c.c. \quad (2.2)$$

When these fields interact in a medium with a second-order nonlinearity, they generate a polarization there, which in turn may generate new frequency components. According to Equation (2.1) the second-order polarization depends on the square of the electric field  $E(t)^2$ . By expanding the whole term, all the second order processes are obtained

$$P^{(2)}(t) = 2\varepsilon_0 d_{\text{eff}} E(t)^2 = 2\varepsilon_0 d_{\text{eff}} \begin{cases} A_1^2 \exp(-2i\omega_1 t) + c.c. & \text{SHG} \\ A_2^2 \exp(-2i\omega_2 t) + c.c. & \text{SHG} \\ 2|A_1|^2 + 2|A_2|^2 & \text{OR} \\ 2A_1 A_2 \exp(-i(\omega_1 + \omega_2)t) + c.c. & \text{SFG} \\ 2A_1 A_2^* \exp(-i(\omega_1 - \omega_2)t) + c.c. & \text{DFG} \end{cases} \quad (2.3)$$

From top to bottom the processes are second-harmonic generation (SHG) from either  $\omega_1$  or  $\omega_2$ , optical rectification (OR), which is a constant polarization, sum-frequency generation (SFG) and difference-frequency generation (DFG).

Of course, these processes do not take place at arbitrary frequency combinations. First and foremost, the conservation of energy must be ensured. For the DFG process this implies

$$\hbar\omega_1 - \hbar\omega_2 = \hbar\omega_3. \quad (2.4)$$

The corresponding energy level diagram is shown in Figure 2.1(a). The nonlinear medium is not excited to a higher energy level, but remains in the ground state. Instead, the parametric process occurs via a transient or virtual energy state. In addition, it can already be seen in this diagram, that for each destroyed input photon at highest frequency  $\omega_1$ , a photon at the lower input frequency  $\omega_2$  must be generated. An optical parametric amplifier (OPA) exploits this behavior. Commonly, the involved light fields are named pump, signal and idler field. The presence of a weak seed beam at the signal frequency  $\omega_s = \omega_3$  stimulates the strong pump beam ( $\omega_p = \omega_1$ ) to decay into a signal and idler beam ( $\omega_i = \omega_2$ ). Furthermore, even without the seed, a strong pump can generate signal and idler spontaneously. This is called parametric fluorescence or optical parametric generation (OPG). However in this case, the generated fields are much weaker than in the amplified one. But by building a cavity around the nonlinear

medium, the signal can be enhanced significantly and is amplified each round-trip. Such a system is called an *Optical Parametric Oscillator* (OPO). The different possibilities of the parametric interaction are shown in Figure 2.1(b)-(e).

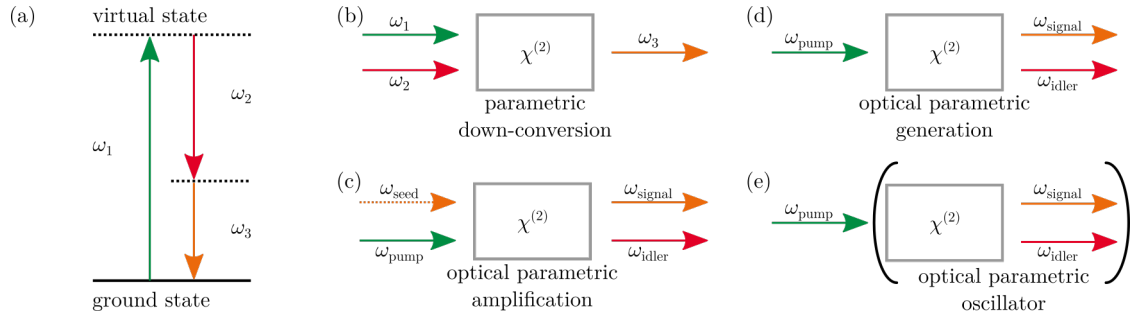


Figure 2.1: (a) Energy level diagram of the difference-frequency generation and schematics of its parametric processes: (b) parametric down-conversion, (c) parametric amplification, (d) parametric generation and (e) the optical parametric oscillator.

In addition, the momentum must be conserved. For light fields, it is determined by the wave vector  $\vec{k}(\omega)$  and is expressed commonly through the phase-mismatch  $\Delta\vec{k} = \vec{k}(\omega_1) - \vec{k}(\omega_2) - \vec{k}(\omega_3)$ . Section 2.2 takes a closer look at this issue.

## 2.1.2 Optical Parametric Gain

The full mathematical description of parametric interactions between the electromagnetic light fields and a nonlinear crystals, is given by Maxwell's equations [16]. They are the foundation of all classical optics and lead to the nonlinear wave equation

$$\frac{\partial^2 E}{\partial z^2} - \frac{n^2}{c^2} \frac{\partial^2 E}{\partial t^2} = \frac{1}{\varepsilon_0 c^2} \frac{\partial^2 P^{(2)}}{\partial t^2}. \quad (2.5)$$

It contains the wavelength-dependent refractive index  $n$ , the vacuum permittivity  $\varepsilon_0$ , the speed of light  $c$  and the second-order polarization from Equation (2.3). The total electric field comprises all three involved waves

$$E = E_s(\omega_s) + E_i(\omega_i) + E_p(\omega_p) \quad \text{with} \quad E_j(\omega_j) = A_j e^{-i(\omega_j t - k_j z)} + c.c., \quad j = s, i, p.$$

For the derivation of Equation (2.5) common assumptions for the medium are made. It is considered to be non-conductive, as well as non-magnetic and the optical losses are neglected. These conditions apply for most commonly used nonlinear materials. With the further assumption that the field amplitudes vary only slowly with respect to the

wavelength, the wave equation (2.5) can be separated into three coupled differential equations [19]

$$\begin{aligned}\frac{\partial A_s}{\partial z} &= i\kappa_s A_p A_i^* e^{i\Delta k z}, \\ \frac{\partial A_i}{\partial z} &= i\kappa_i A_p A_s^* e^{i\Delta k z}, \\ \frac{\partial A_p}{\partial z} &= i\kappa_p A_s A_i e^{-i\Delta k z},\end{aligned}\tag{2.6}$$

where  $\kappa_j = \omega_j d_{\text{eff}}/n_j c$  and  $\Delta k = k_p - k_s - k_i$  is the phase-mismatch, which is explained more in Section 2.2. Using these three equations, all the second-order nonlinear processes, from SHG to SFG and DFG can be explained, depending on the involved fields and the starting conditions. For the parametric amplification, a strong, non-depleting pump and no idler, but an initially weak seed signal can be assumed. Solving the coupled differential Equations (2.6) yields the amplitude of the signal wave  $A_s(z)$  and thus its intensity curve  $I_s(z) \propto |A_s(z)|^2$ . The detailed derivation is given in the Appendix A. In this way it is possible to derive the parametric gain in a nonlinear crystal of length  $l$  to

$$G(l) = \frac{I_s(z=l)}{I_s(z=0)} = \frac{\Gamma^2}{g^2} \sinh^2(gl) \quad , \quad \text{where} \quad \begin{aligned} g &= \sqrt{\Gamma^2 - (\Delta k/2)^2} \\ \Gamma &= \frac{2\omega_s \omega_i d_{\text{eff}}^2 I_p}{n_s n_i n_p \varepsilon_0 c^3}, \end{aligned}\tag{2.7}$$

with the gain factor or conversion rate  $\Gamma$  and the modified gain  $g$ , which takes the phase-mismatch into account. For perfect phase-matching  $\Delta k = 0$ , it writes as  $G(l) = \sinh^2(\Gamma l)$ . The reduction of the gain with increasing phase-mismatch is plotted in Figure 2.2(a). In the high-gain regime  $\Gamma^2 \gg \Delta k^2$ , the conversion rate clearly exceeds the phase mismatch and the gain grows exponentially with the crystal length

$$G(l) = \sinh^2(\Gamma l) \approx \frac{1}{4} e^{2\Gamma l}.$$

In this way, an optical parametric amplifier (OPA) can run efficiently even in single pass configuration. However, in the low-gain regime with a large phase-mismatch  $\Gamma^2 \ll \Delta k^2$  the newly generated and the already existing signal wave run out of phase and back-conversion into the fundamental pump wave takes place. The parametric gain starts to oscillate with

$$G(l) = \Gamma^2 l^2 \frac{\sin^2\left(\sqrt{(\Delta k l/2)^2 - \Gamma^2 l^2}\right)}{(\Delta k l/2)^2 - \Gamma^2 l^2} \approx \Gamma^2 l^2 \frac{\sin^2(\Delta k l/2)}{(\Delta k l/2)^2}.$$

This behavior is shown in Figure 2.2 on the right.

As an example, three different OPO and OPA configurations are presented in Table 2.1: a continuous-wave OPO in the low-gain regime [20], an OPO which resembles the

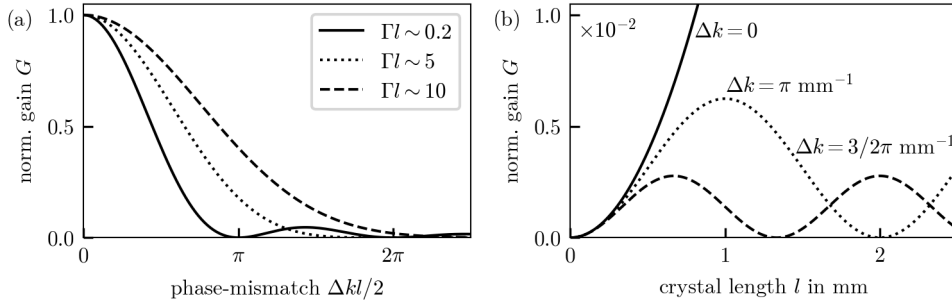


Figure 2.2: Left: Parametric gain depending on the phase-mismatch  $\Delta kl/2$  for the three examples from Table 2.1. The greater the conversion  $\Gamma l$ , the greater the bandwidth of the process. Right: Parametric gain over the crystal length  $l$  for the low-gain example with  $\Gamma l \sim 0.2$  normalized to the maximal gain for perfect phase-matching in a 8 mm crystal [17].

light source presented in Chapter 3, and a high power OPA [21]. It is important to note that these calculations are only valid for perfect phase-matching and monochromatic light fields, which in practice are never achieved. On the contrary, for the amplification of ultrashort laser pulses a broadband gain spectrum is crucial [22]. In addition, further effects like pump depletion or a temporal and spatial walk-off, which severely reduce the gain, are neglected. Nonetheless, a good overview of the expected orders of magnitude is given.

		continuous wave OPO [20]	femtosecond OPO	high-power OPA [21]
pump power	$P_{\text{ave}}$	20 W	7.5 W	100 W
pulse duration	$\tau$	–	300 fs	900 fs
repetition rate	$f_{\text{rep}}$	–	34 MHz	100 kHz
focus waist	$w_0$	60 $\mu\text{m}$	30 $\mu\text{m}$	0.8 mm
peak intensity	$I_p$	175 kW/cm <sup>2</sup>	25 GW/cm <sup>2</sup>	50 GW/cm <sup>2</sup>
crystal		5%MgO-PPLN	BBO	BBO
nl. coefficient	$d_{\text{eff}}$	27 pm/V	2 pm/V	2 pm/V
crystal length	$l$	8 mm	2 mm	3 mm
conversion rate	$\Gamma$	0.027 mm <sup>-1</sup>	2.5 mm <sup>-1</sup>	3.4 mm <sup>-1</sup>
conversion	$\Gamma l$	0.2	5	10
net intensity gain	$G(l)$	0.05	5500	$2.4 \times 10^8$

Table 2.1: Three exemplary parametric systems in different gain regimes. The calculations are based on the data of the respective publications and the mentioned Equation (2.7). Here, perfect phase-matching  $\Delta k = 0$  and a single-pass configuration were assumed. The last line lists the net gain for a single-pass through the crystal [19]. The highlighted femtosecond-OPO corresponds to the used light source for the experiments in this thesis.

## 2.2 Phase-matching

As described in the previous section, a pump beam with a certain frequency  $\omega_p$  induces in an OPO a nonlinear polarization which in turn generates new frequencies  $\omega_s$  and  $\omega_i$  following the energy conservation. However, a macroscopic medium consists not only of a single atom, but many. And each of them will generate new waves that superimpose with each other. But all generated waves will have independent phases and interfere destructively. To circumvent this problem, all waves need to superimpose constructively, which is called phase-matching. Thus, only with specially arranged crystals an efficient generation of new frequencies is possible. The phase-matching (PM) conditions are coupled to the momentum conservation, which is defined in terms of the wave vector  $\vec{k}$ . The wave vector points perpendicular to the wave fronts and its absolute value is given by  $|\vec{k}(\omega)| = \frac{\omega}{c}n(\omega)$ , with the speed of light  $c$  and the frequency dependent refractive index  $n(\omega)$ . For the parametric generation the conservation of momentum is expressed as

$$\hbar\vec{k}_p = \hbar\vec{k}_s + \hbar\vec{k}_i. \quad (2.8)$$

Often it is written in terms of the phase-mismatch  $\Delta\vec{k} = \vec{k}_p - \vec{k}_s - \vec{k}_i$ . For perfect PM applies  $\Delta\vec{k} = 0$ . Though, in the collinear case, when all wave vectors point into the same direction, it needs to hold  $n_p\omega_p = n_s\omega_s + n_i\omega_i$ . However, most materials show normal dispersion. This implies that the higher the frequency, the larger the refractive index. By general convention,  $\omega_p > \omega_s > \omega_i$  is valid and thus  $n_p > n_s > n_i$  holds in this case. Together with the energy conservation  $\omega_p = \omega_s + \omega_i$  it is not possible to satisfy the PM condition. To fulfill it anyway, the refractive index difference of differently polarized light in birefringent crystals can be exploited.

### 2.2.1 Birefringent Phase-matching

In birefringent crystals the refractive index depends on the polarization, which relates this time to the oscillation planes of the electromagnetic fields. In this thesis, the focus is on uniaxial crystals. They have one main crystal axis, called the optical axis (OA), which spans with the wave vector of the propagating beam  $\vec{k}$  the principal plane. It is illustrated in Figure 2.3(a) and (b) in gray. The part of the field, which is polarized perpendicular to the principal plane is called the ordinary beam or o-wave. It has a direction-independent refractive index  $n_o$ . The other part, oscillating in the principal plane, is the extraordinary beam or e-wave. Its refractive index depends on the propagation direction, which is commonly given by the polar angle  $\theta$  between the OA and the wave vector of the field  $\vec{k}$ . For  $\theta = 0^\circ$ , the wave vector is parallel to the OA and the extraordinary field experiences the same refractive index  $n_o$  as the ordinary one. In contrast, for  $\theta = 90^\circ$  the refractive index reaches its extreme

non-critical PM	Type 0	Type I <sup>(-)</sup>	Type II <sup>(-)</sup>
$\theta = 0^\circ$ or $90^\circ$ no walk off	$e \rightarrow ee$	$e \rightarrow oo$	$e \rightarrow eo$ $e \rightarrow oe$
critical PM	Type 0	Type I <sup>(+)</sup>	Type II <sup>(+)</sup>
$\theta \neq 0^\circ$ or $90^\circ$ walk off	$o \rightarrow oo$	$o \rightarrow ee$	$o \rightarrow eo$ $o \rightarrow oe$

Table 2.2: Types of phase-matching configurations in uniaxial crystals Left: Main differences between critical and non-critical PM. Right: Different types of PM configurations in negative (-) and positive (+) uniaxial crystals. The configurations show the extraordinary (e) and ordinary polarization (o) states of the involved beams in an OPG process.

value  $n_e$ . Depending on the size ratios, there are negative ( $n_o > n_e$ ) and positive ( $n_o < n_e$ ) uniaxial crystals. This distinction is necessary because later in this section, it determines the direction of deflection and the permitted PM configurations. In general, the extraordinary refractive index can be calculated via

$$\frac{1}{n_e(\theta)^2} = \frac{\sin^2 \theta}{n_e^2} + \frac{\cos^2 \theta}{n_o^2}. \quad (2.9)$$

This Equation (2.9) describes an ellipse, with the refractive indices  $n_o$  and  $n_e$  on the semiaxes. It is illustrated in Figure 2.3(c). The refractive index  $n_e(\theta)$  is determined by the intersection between the wave vector  $\vec{k}$  and the ellipse. For the ordinary beam (gray), the ellipse becomes a circle and the refractive index  $n_o$  is independent of the direction. By tailoring the correct angle  $\theta$  and therefore a specific refractive index  $n_e$ , the PM condition can be fulfilled. This technique is also known as critical PM, since it is very responsive to angular variations of  $\theta$ .

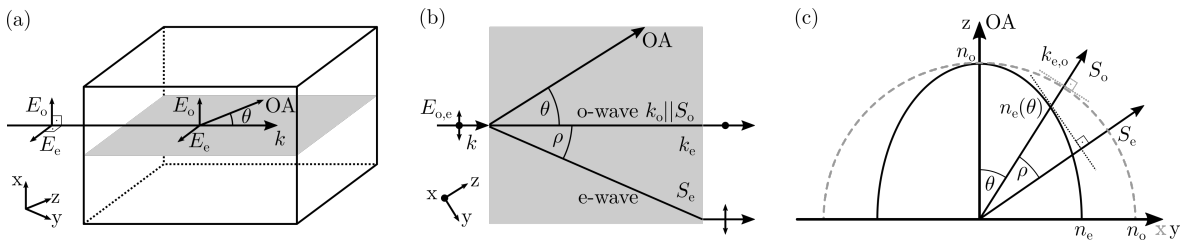


Figure 2.3: (a) Schematic of a uniaxial crystal: The principal plane (gray) is spanned by the wave vector  $\vec{k}$  and the crystal axis OA. The electric field oscillations  $E_{o,e}$  are normal to the wave vector. (b) Top view of the crystal: The wave vector  $k_e$  and Poynting vector  $\vec{S}_e$  do not coincide, but form the walk-off angle  $\rho$ . (c) Index ellipse for a negative uniaxial crystal. For the ordinary beam it forms a circle (gray) [23].

Overall, a distinction is made between different types of birefringent PM regarding to the polarizations of the pump, signal and idler beams. To satisfy the PM condition



it is important that the refractive index of the pump beam  $n_p$  is smaller than the one for the signal and idler beams  $n_s$  and  $n_i$ . Therefore, it is necessary to discriminate between negative and positive uniaxial crystals. An overview is given in Table 2.2, on the right side. Here, the notation is associated with the polarizations of the wave vectors  $k_p \rightarrow k_s k_i$ . The sign indicates, if the crystal is negative (-) or positive (+) uniaxial. For Type 0, all interacting waves have the same polarization. It cannot be exploited for birefringent PM.

However, in birefringent crystals the extraordinary wave travels in a different direction than the ordinary one, as can be seen in Figure 2.3(b). This walk-off limits the spatial overlap of the interacting light beams propagating through the crystal and thus constrains the crystal length. The wave vectors  $\vec{k}_{o,e}$  remain parallel, but the power flows, indicated by the Poynting vectors  $\vec{S}_{o,e}$ , separate. They form the walk-off angle

$$\rho(\theta) = \pm \left[ \arctan \left( \frac{n_o^2}{n_e^2} \tan(\theta) \right) - \theta \right]. \quad (2.10)$$

The sign indicates whether it is a negative or positive uniaxial crystal. The angle is illustrated in the ellipse in Figure 2.3(c). The Poynting vector  $\vec{S}$  points perpendicular to the tangent of the index ellipse at its intersection point with the wave vector  $\vec{k}$ . For  $\theta = 0^\circ$  and  $\theta = 90^\circ$ , there is no walk-off. In these cases, the angular adjustment of the crystal is less sensitive or less critical to deviations. This is why this configuration is called non-critical PM. Commonly, for non-critical PM the phase-mismatch  $\Delta k$  is minimized via the crystal temperature. More on this can be found in the next Section 2.2.2.

Besides uniaxial crystals, there are also a number of biaxial crystals, which are suitable for nonlinear processes. They have not one main optical crystal axis, but two and therefore three different refractive indices on the semi-axes. To describe the beam propagation, the azimuthal angle  $\phi$  must be introduced in addition to the polar angle  $\theta$ . The calculations of the refractive indices and the PM angles are incomparably more difficult. An accurate derivation will be omitted here. In [23] all the formulas for calculating the PM angles and the nonlinear coefficients are listed and explained in more detail.

## 2.2.2 Quasi-Phase-Matching

For the sake of completeness, quasi-phase-matching (QPM) is to be introduced briefly. Even in non-phase-matched crystals the signal of a parametric process can build up over a certain coherence length  $l_c = \pi/\Delta k$ . The pump beam generates the signal and idler beams, but they accumulate a phase shift while propagating through the crystal. If the phase shift exceeds  $\pi$ , back-conversion takes place. The signal and the idler sum

up and transfer their energy via SFG back to the pump. After another  $\pi$  phase shift, the signal is completely back-converted and the cycle starts again. This behavior can be seen in Figure 2.2(b) in the previous Section 2.1.2. However, flipping the crystal optical axis every coherence length, whenever the maximum signal is reached, resets the phase shift. This ensures a continuous energy transfer from the pump beam into the signal. Typically, ferroelectric materials with outstandingly high nonlinear coefficients  $d_{\text{eff}}$  are chosen, allowing nonlinear processes even in low-power or continuous wave operations. Attaching electrodes in a periodic pattern on the crystal surface with a high voltage reverses their domains in the selected regions. These periodically poled crystals are neither limited in their birefringence properties nor in the polarization of the interacting beams and thus allow for non-critical, Type 0 PM schemes with no walk-off. The fine tuning to adapt the modulation period of the grating to the pump wavelength is typically done via the crystal temperature. Thus, QPM goes hand in hand with a crystal oven and temperature control. In contrast to a mechanical tuning of the crystal or to an electronic shifting of the pump wavelength, temperature changes are very slow. Hence, QPM is not suitable for fast spectroscopic experiments, which are topic of this thesis. Alternatively, various grating patterns in the crystals, like multiple gratings with different periods or fan-shaped gratings, are used for tuning the output wavelength [24]. Translating the crystal so that the pump beam passes through a different grating structure allows to shift the phase-matched wavelength. Nevertheless, the tuning range is strongly limited by the crystal size. More details about QPM with a mathematical description and specific tuning techniques can be found in the mentioned textbooks [15, 16] and in the review paper [24].

### 2.2.3 Collinear vs. Non-collinear Phase-Matching

Until now, only collinear PM with monochromatic waves has been considered. This means that the wave vectors from the interacting beams run parallel, as shown in Figure 2.4(a). However, for broadband parametric generation the phase-matching condition  $k(\omega_p) = k(\omega_s) + k(\omega_i)$  must withstand changes in the signal and idler wavelengths. Assuming a fixed pump frequency  $\omega_p$  and a changed signal frequency  $\omega'_s = \omega_s + \Delta\omega$ , then the idler frequency follows due to the energy conservation  $\omega'_i = \omega_i - \Delta\omega$ . A Taylor expansion shows the impact on the wave vectors [22]

$$k(\omega_s + \Delta\omega) = k(\omega_s) + \left. \frac{\partial k}{\partial \omega} \right|_{\omega_s} \Delta\omega = k_s + \frac{\Delta\omega}{v_{\text{gs}}}, \quad (2.11a)$$

$$k(\omega_i - \Delta\omega) = k(\omega_i) - \left. \frac{\partial k}{\partial \omega} \right|_{\omega_i} \Delta\omega = k_i - \frac{\Delta\omega}{v_{\text{gi}}}. \quad (2.11b)$$

The additional phase-mismatch due to the small frequency shift  $\Delta\omega$  amounts to  $\Delta k \simeq (1/v_{gs} - 1/v_{gi}) \Delta\omega$ , with the group velocities of the signal and idler beams  $v_{gs}$  and  $v_{gi}$ . It becomes smaller for smaller group velocity differences. Typically around the degeneracy point, where signal and idler have the same frequency, more broadband PM is found. A simulation of broadband collinear PM in a beta barium borate (BBO) crystal similar to the one used in the following NOPO experiments is shown in Figure 2.5(a).

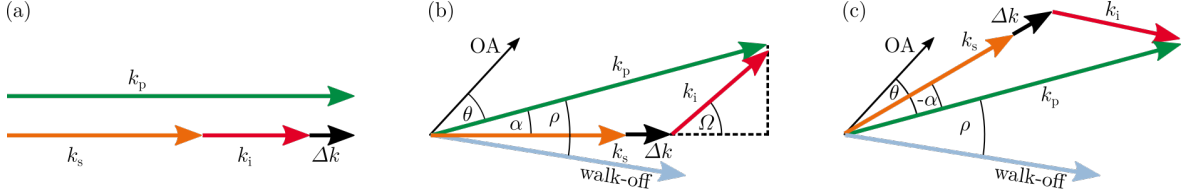


Figure 2.4: Schematics of (a) collinear and (b-c) non-collinear PM geometries. Non-collinear PM distinguishes between (b) the Poynting Vector Walk-off Compensation, where the signal wave vector  $k_s$  is close to the Poynting vector of the extraordinary pump beam (bright blue) and (c) the Tangential PM geometry, where it propagates on the opposite side of the pump vector  $k_p$ .

However, a more promising approach to reach broadband amplification is non-collinear PM, where the pump and signal radiation enclose the non-collinear angle  $\alpha$  and the idler is emitted at an angle  $\Omega$  as can be seen in Figure 2.4(b). Geometric considerations lead to the non-collinear phase-mismatch

$$\Delta k(\alpha) = k_p \cos \alpha - k_s - \sqrt{k_i^2 - k_p^2 \sin^2 \alpha}. \quad (2.12)$$

Using the same approach as in the collinear case, with a Taylor expansion for small frequency changes, perfect PM  $\Delta k = 0$  is now given by the condition  $v_{gs} = v_{gi} \cos \Omega$ . The different group velocities between signal and idler can be compensated by the non-collinear geometry and thus, the temporal overlap is ensured [22].

Depending on the direction of the non-collinear angle  $\alpha$ , a distinction is made between two types of PM: the Poynting Vector Walk-off Compensation geometry (PVWC) and the Tangential PM geometry (TPG). They are sketched in Figure 2.4(b) and (c) for the case of a negative uniaxial crystal as used in the following experiments of this work. Essentially, their main difference is the overlap of the signal beam with the divergent energy flow of the pump, which is explained in Section 2.2.1 with the birefringent walk-off. The effects of the different geometries can no longer be described by analytic equations, but need to be simulated by a numerical model [25, 26].

In BBO crystals, there is the "magic angle"  $\alpha = \pm 2.5^\circ$  at which very broadband PM occurs. For comparison, the phase-matched wavelengths in BBO, pumped at 515 nm for two different angles of incidence  $\theta$  are shown over the non-collinear angle  $\alpha$  in Figure 2.5.

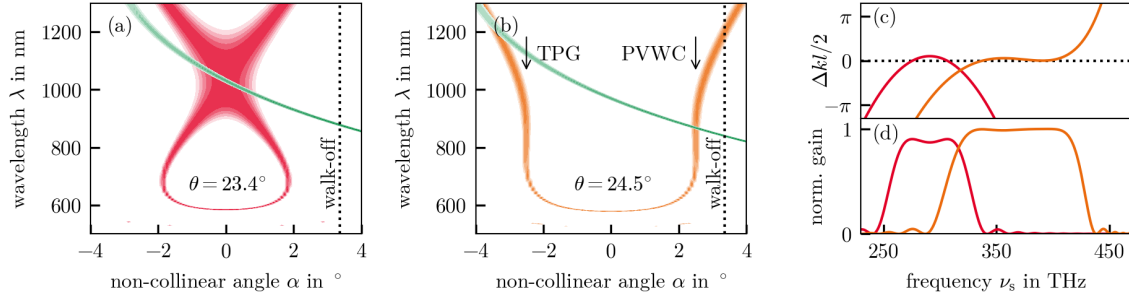


Figure 2.5: Simulations of the phase-matched wavelength of the DFG-process over the non-collinear angle  $\alpha$  in a 1.5 mm BBO-crystal pumped at 515 nm. (a) Collinear PM with  $\alpha = 0^\circ$  occurs at  $\theta = 23.4^\circ$  close to the degeneracy point in red. (b) Very broadband non-collinear PM at  $\theta = 24.5^\circ$ ,  $\alpha = 2.5^\circ$  in orange. The green line indicates likewise phase-matched parasitic SHG of the signal. (c) Phase-mismatch and (d) gain bandwidth for the collinear (red) and non-collinear (orange) case.

The calculations are based on the Equations (2.7) and (2.12) of the parametric gain and the non-collinear phase-mismatch. For  $\theta = 23.4^\circ$  broadband collinear PM is found around the degeneracy point as predicted by Equation (2.11). On the other hand, for  $\theta = 24.5^\circ$  even broader PM occurs. The phase-mismatch and the gain bandwidth are illustrated in Figure 2.5(c) and (d), for both cases respectively. It is important to add that in the collinear, as well as in the non-collinear case, parasitic SHG is phase-matched in addition to the desired DFG. Since both processes are competitively amplified, parametric oscillators in these configurations fluctuate strongly and break down in output power. The phase-matched SHG radiation is indicated in green in Figure 2.5.

To summarize, in general PVWC offers a superior beam profile, due to the better spatial overlap of pump and signal beams in the nonlinear medium. However, the large walk-off in TPG geometry can be compensated with a high pump power in combination with a large pump spot size and a short crystal length. In this case, it is superior to PVWC, as it offers a consistent PM range without interfering parasitic SHG generation. Nevertheless, the PVWC geometry was chosen for the NOPO built in this work, as the beam profile is crucial for the further spectroscopy applications.

## 2.3 Tuning of Optical Parametric Oscillators

OPOs are known for their outstanding tunability. As elaborated throughout this chapter, the output wavelength is not limited to the fixed properties of a laser-active medium, but excellently tailorable over the PM conditions. After a short overview of collinear OPO tuning techniques, the tuning mechanism of the non-collinear parametric oscillator, which is used for the spectroscopic experiments in this thesis is discussed.

### 2.3.1 Collinear Tuning

As pointed out in Section 2.2.3, in general, collinear OPOs have a more narrowband PM condition. It depends on the interacting wavelengths, as well as on a large number of parameters via the refractive indices [16]

$$\Delta k = 2\pi \left[ \frac{n_p(\lambda_p, \theta, T, \dots)}{\lambda_p} - \frac{n_s(\lambda_s, \theta, T, \dots)}{\lambda_s} - \frac{n_i(\lambda_i, \theta, T, \dots)}{\lambda_i} \right]. \quad (2.13)$$

Shifting one of these parameters will lead to a change in the output wavelength.

One option is already introduced in Chapter 2.2.1, which deals with birefringent PM. The orientation of the optical crystal axis influences the refractive index of light with extraordinary polarization. This is referred as angular tuning. The angle  $\theta$  between the OA and the pump radiation is changed either by a rotation of the crystal or by an angular adjustment of the pump beam. Though, in both cases the propagation direction of the resonant radiation inside the cavity changes as well. The cavity needs to be realigned with every modification step, which is rather complicated and difficult to automate. Another approach, also already mentioned in Section 2.2.2, is temperature tuning. Especially in periodically poled crystals, the phase-mismatch is quite sensitive to heating. In a crystal oven, the temperature of the nonlinear medium is controlled and adjusted for tuning. However, compared to the mechanical or electronic tuning possibilities, temperature changes are slow. They do not allow for fast wavelength shifting in spectroscopic experiments. The third often used technique is pump wavelength tuning. Initially, mainly Ti:Sapphire lasers were used as pump sources for OPOs. They offer a broadband gain bandwidth and could be tuned itself to some extend. Meanwhile, new types of fiber lasers have been developed, that can be tuned at high speed. Compared to light sources based on bulk crystals and free-space propagation they run very stably and are very suitable for working even in the absence of perfect laboratory conditions. Certainly, they will play an important role in future OPO development.

Examples for all three tuning methods can be found in [19]. Nowadays, there are commercially available OPOs between continuous wave to the femtosecond time scales. However, they suffer from the slow adjustment speed of the PM conditions. For time-resolved imaging or spectroscopy applications, fast tunable light sources with short pulses are desired. This can be achieved by switching to the non-collinear geometry.

### 2.3.2 Non-collinear Tuning

Instead of shifting the narrowband PM conditions in the collinear geometry, a non-collinear OPO (NOPO) exploits the broadband PM condition discussed in Section 2.2.3. The wide tunability results from synchronous pumping of a small part of the

broadband generated spectrum. Figure 2.6(a) shows a simplified sketch of the presented NOPO from Chapter 3.2. A pump pulse generates a broadband parametric fluorescence in the nonlinear medium. Due to the non-collinear geometry, it contains all different phase-matched frequencies. This signal travels through the cavity and diverges spectrally due to a specifically tailored dispersion. Because of this broadening the signal pulse is many times longer than the pump pulses. The overlap between the next pump pulse with the resonating signal determines the efficiently amplified output wavelength.

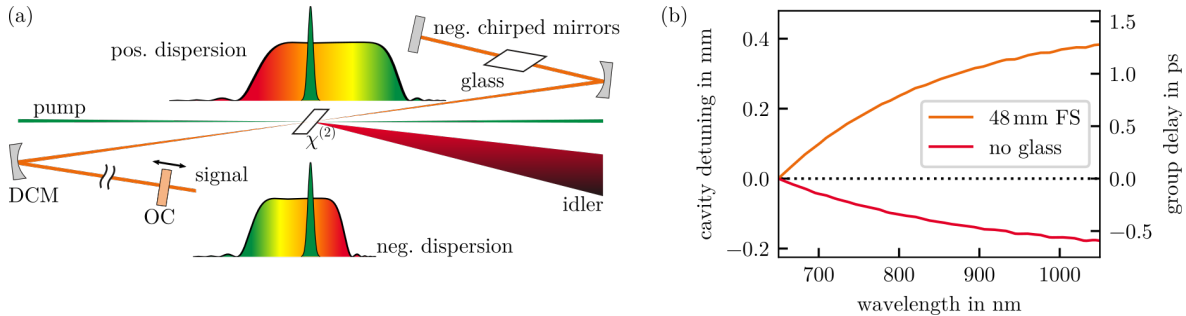


Figure 2.6: (a) Synchronously pumped NOPO. The width of the parametric fluorescence depends on the internal dispersion. Bottom: Small amount of negative dispersion due to the double-chirped mirrors (DCM) results in narrowband fluorescence. Top: Additional glass inside the cavity broadens the superfluorescence. The overlap with the pump is adjusted over the round-trip time. (b) Simulation of the cavity detuning and group delay over the efficiently amplified wavelength. The calculations are based on the cavity design for the NOPO described in the next chapter.

The dispersion control and its influence on the spectral phase is crucial for the NOPO. The first-order phase, the group delay (GD), affects a shift in time of the resonating pulse. It can be compensated by adjusting the cavity length. The second-order spectral phase, the group delay dispersion (GDD), causes the pulses to diverge in time. For normal dispersion, the red parts of the spectrum travel faster than the blue parts and the pulses broaden. The short pump pulses provide a gain window. The part of the broadband superfluorescence that passes through the nonlinear medium simultaneously with the pump will be amplified efficiently. The cavity roundtrip time, and therefore the cavity length, determines their temporal overlap. Furthermore, the amount of GDD can be used to regulate the spectral bandwidth of the output pulses. The more dispersion, the more the signal diverges and the narrower are the resulting pulses. Thus, the dispersion directly determines the spectral bandwidth and the tuning behavior of the NOPO, two key parameters for the subsequent spectroscopy experiments.

Experimentally, the internal dispersion can be regulated via chirped mirrors. During the development of ultrashort laser pulses, the design of double chirped mirrors (DCMs) was greatly advanced [27]. They offer an ultrabroadband reflection range in

combination with a negative chirp to prevent ultrashort laser pulses from diverging in time during propagation. Often they are used in pairs to reduce their strong oscillations in the GDD. This can be seen later in Figure 3.3(b), where the setup of the constructed NOPO is described. On the other hand, any amount of normal dispersion can be added to the cavity by prism pairs or glass windows. A simulation of the dispersion curves as well as the tuning behavior of the NOPO presented in this thesis are given in Chapter 3. More detailed insights into the NOPO mechanics, together with a full characterization of a system depending on different amounts of dispersion is found in [25, 28].





### 3 | Experimental realization of a Non-collinear Optical Parametric Oscillator

Following the theoretical considerations, the demands on a fast tunable NOPO are defined. A suitable pump source must provide sufficient high intensities for the parametric process, as well as short pulse durations to create a gain window for the spectral tuning method described in the last chapter. Among others, YAG-lasers have proven to be appropriate for this purpose. Particularly in the thin-disk geometry, they allow for high-power operation with femtosecond pulses. The choice of the nonlinear crystal depends on the desired output wavelength. For the visible and near-infrared regime, beta barium borate (BBO) is a reliable candidate. In the mid-IR range zinc germanium phosphide (ZGP) and cadmium silicon phosphide (CSP) show excellent properties for broadband operation with high conversion rates [29]. In addition to a large nonlinear coefficient  $d_{\text{eff}}$ , a wide transparency range and a high damage threshold are key factors for selecting appropriate crystals. A selection of the most adequate crystals for OPOs operating in the near-IR spectral regime is presented in the following Section 3.1. Here, a brief chronological outline of alternative tunable laser sources is given as well.

For the stimulated Raman measurements, not a specific wavelength is needed, but a relative wavenumber difference, which is tunable over a specific range. Nevertheless, output wavelengths in the near-IR regime are preferable to those in the visible or ultraviolet spectral range. Even though the Raman process is slightly less efficient there, but interfering fluorescence lines are avoided. On the other hand, in the far-IR range, most materials begin to absorb the excitation light. In microscopy, typically only a few tens of milliwatts average power are needed due to the strong focusing. However, for monitoring large areas the power needs to be scaled accordingly. This chapter introduces the NOPO, matching the listed requirements for the spectroscopic measurements in the scope of this thesis. The experimental setup is followed by an investigation of the dispersion management, as well as the characterization of the light source.

### 3.1 Tunable OPOs and alternative light sources

The first tunable optical parametric oscillator (OPO) was published in 1965, only four years after the invention of the laser [30]. The cavity consisted merely of a lithium niobate crystal about 5 mm long with reflective, dielectric coatings on the end faces. The output wavelength was already tunable over a range of 70 nm, from 970 nm to 1040 nm by controlling the crystal temperature. Even then, the potential of this technology to construct continuously tunable oscillators was recognized. However, due to the lack of suitable pump sources with high coherence and intensity, as well as missing nonlinear crystals with appropriate optical properties, the field of OPO development remained behind these expectations for 20 years [19]. Instead, dye lasers gained much popularity. The mostly liquid dyes feature broad emission and absorption bands. Replacing one cavity mirror with a diffraction grating, the lasers offer a good tunability with narrow linewidth [31]. Things changed, with the coming of the more practical solid-state lasers, most notably the Ti:Sapphire laser. It owns a broad gain bandwidth, ranging from 680 nm to 1100 nm and offers a certain tunability itself. As alternative tunable light sources, chromium-based solid-state lasers are worth to mention. They have similar intrinsic properties as Ti:Sapphire, but in the near-infrared spectral range [32]. A selection of the most conventional tunable lasers is shown in Figure 3.1. The cited systems are mostly continuous-wave or nanosecond oscillators, since the ultrashort pulse lasers require the broad optical bandwidth to generate the short pulses.

Around the same time of the advent of solid-state lasers, the discovery of new nonlinear crystals invigorated OPO research. Particularly promising in the near-IR spectral regime are beta barium borate (BBO), lithium triborate (LBO), potassium titanyl phosphate (KTP) and bismuth triborate (BIBO). Besides broadband phase-matching conditions, they feature a wide transparency range and a high damage threshold. Firstly, nanosecond-pulse OPOs were reported. They were pumped by Q-switched neodymium lasers, which were commercially available early on. Their radiation was used at 1064 nm or its second or third harmonic at 535 nm and 355 nm, respectively [33]. With the development of Kerr-lens mode-locking (KLM) within Ti:sapphire lasers [34], likewise the OPO research was pushed to picosecond and femtosecond time scales. The high peak intensities of the ultrafast pump lasers lead to high parametric gains, so that the OPO-threshold is easily exceeded. In contrast, continuous-wave OPOs were realized rather late. Usually, they require cavity designs with more than one resonating wave to build up enough gain and enable successful operation. Another breakthrough was achieved with quasi-phasematching (see Section 2.2.2) and the development of periodically poled lithium niobate (PPLN) and KTP crystals (PPKTP). Their high nonlinear coefficient  $d_{\text{eff}}$  is 5 to 10 times larger than for BBO, depending on the exact configuration. Together with the possibility to use rather long crystals, they allow for

extremely widely tunable OPOs from continuous-wave to femtosecond pulse durations. To demonstrate the tuning range, a variety of reported OPOs with different nonlinear media are illustrated in Figure 3.1. Further examples, mainly from the mid-IR spectral region, can be found in [19,33]. Nowadays, widely tunable OPOs are commercially available on all time scales. Recently, fiber-based OPOs are on the rise. Using a four-wave mixing process in specifically tailored photonic crystal fibers, they are very stable alternatives to free-space OPOs [35]. However, a more detailed description goes beyond the scope of this thesis.

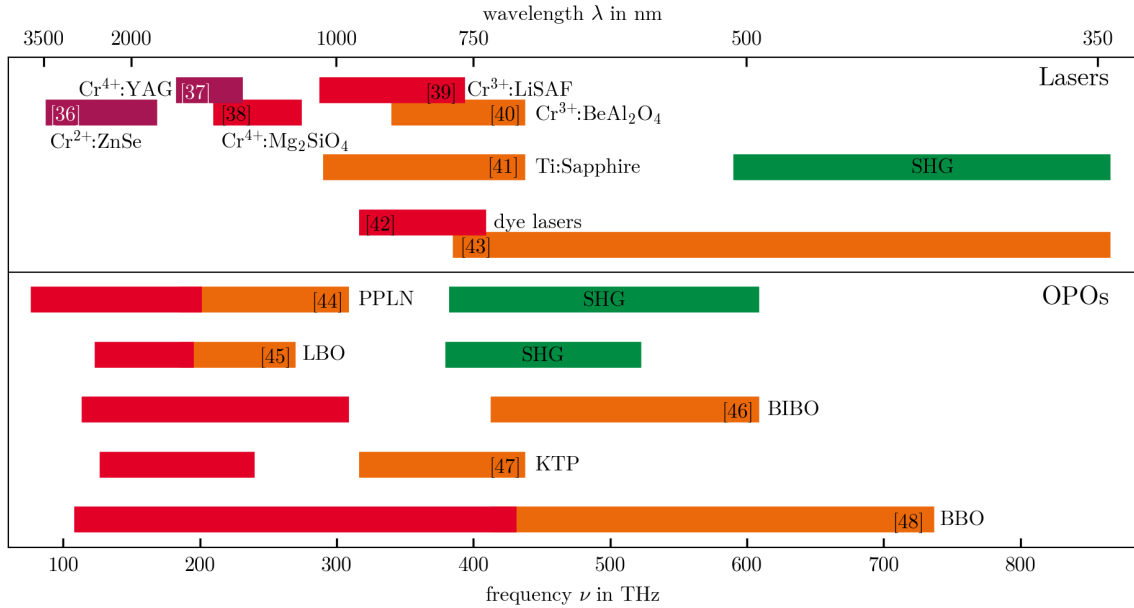


Figure 3.1: Spectral coverage of the most common tunable lasers and OPOs from the ultraviolet to the near-infrared regime. Top: Chromium-doped lasers [36–40], the famous titanium-sapphire laser with its second harmonic [41] and two examples of dye lasers [42, 43]. The colors have no significance. Bottom: Widely tunable OPOs based on the nonlinear crystals PPLN, LBO, BIBO, KTP and BBO [44–48] with their signal (orange) and idler (red) tuning ranges and at times with additional intracavity second harmonic generation (green). The vertical axis has no importance.

For spectroscopy experiments, the narrow-band OPO needs to be tuned in wavelength. However, most OPOs adapt the phase-matching condition over crystal angle or temperature changes, which slows down the measurements. To speed up spectroscopy processes, electronically tunable OPOs can be used. For example, an intracavity electro-optical Lyot filter may change the polarization and thus shift the output wavelength. This way, Kong et al. recorded SRS-spectra in 5 ms per spectral component [49]. But the tuning span of their light source achieves only 7.5 nm, covering a spectral range of 115 cm<sup>-1</sup> in stimulated Raman scattering microscopy. Likewise, a fiber-based OPO was shown by Brinkmann et al. [35]. They combined an electronically tunable wavelength filter with a special chirped fiber Bragg grating as output coupler,

reaching 5 ms per wavelength step as well. But their tuning range between 780 nm and 980 nm is considerably broader. Such fiber-based light sources are particularly characterized by their stability. Therefore, they are ideally suited for use beyond the laboratory work.

## 3.2 Experimental setup of the NOPO

A self-built Kerr-lens mode-locked Yb:YAG thin-disk (KLM TD) laser [50] acts as pump source for the NOPO. It provides 280 fs-pulses with a repetition rate of 34 MHz at an average output power of more than 20 W. Around 9.5 W of the IR-light is converted in a 2 mm lithium triborate (LBO) crystal to more than 7.5 W green light at 515 nm with an efficiency of nearly 80 %. This second harmonic with a pulse energy of 0.2  $\mu$ J is used to pump the NOPO. Via a periscope followed by a lens, the pump beam is focused through a cavity mirror into the nonlinear crystal. A change in height at the periscope causes a change in angle at the same focal point. In this way, the non-collinear angle between the pump and signal beams is adjusted.

The centerpiece of the NOPO is a 2 mm long BBO-crystal. Its outer surfaces are cut in Brewster's angle to minimize losses in the cavity. In Figure 2.5 on page 16 the broadband phase-matching conditions for BBO pumped at 515 nm and  $\theta = 24.5^\circ$  are already shown. Additionally, the non-collinear angle of  $\alpha = 2.4^\circ$  needs to be considered designing the crystal. Therefore, it is cut at an angle  $\theta = 27^\circ$  between the optical axis and the signal beam, which propagates horizontally through the crystal. The pump beam is irradiated at the non-collinear angle in PVWC-geometry to obtain the best possible beam profile. The cavity itself consists of seven plane and two curved double chirped mirrors (DCMs), with a radius of curvature of  $-100$  mm centered around the gain crystal, plus an output coupler with a transmission of 12 % arranged in standing wave geometry. One mirror is placed on a piezoelectric actuator to adjust the cavity length to the desired output wavelength, according to the non-collinear tuning technique presented in the last chapter. For this purpose, a folding mirror rather than an end mirror was specially chosen. With the same movement of the actuator, twice the cavity length change is generated and the output wavelength is tuned more quickly. The resulting misalignment of the NOPO is negligible and has no impact on the stability. A schematic setup and the behavior of the beam waist within the resonator are illustrated in Figure 3.2.

To control the dispersive broadening of the wide parametric fluorescence, the dispersion inside the cavity needs to be regulated. Firstly, this is done via negatively chirped mirrors. The used DCMs cover a high spectral reflection range between 600 nm and 1200 nm and introduce a small amount of negative dispersion. To circumvent the unavoidable oscillations in the group delay (GD) and group delay dispersion (GDD),

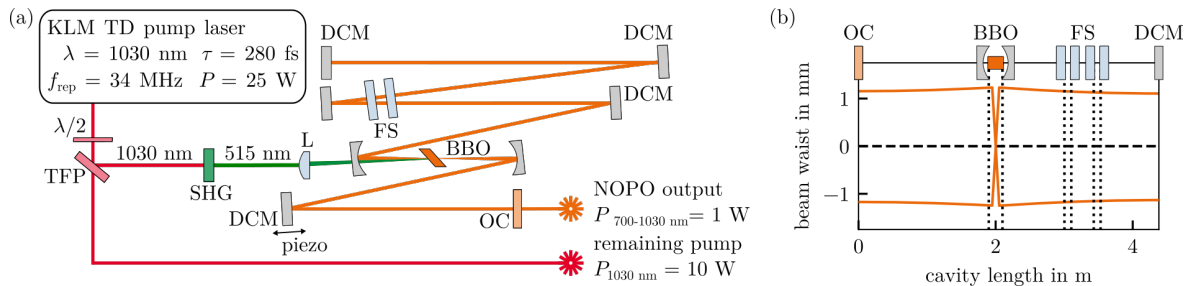


Figure 3.2: (a) Experimental NOPO setup: TFP: thin film polarizer,  $\lambda/2$ : half-wave plate, SHG: LBO-crystal for frequency doubling, L: lens, BBO: gain crystal, DCM: double chirped mirror, FS: fused silica window, OC: output coupler. (b) Simulation of the sagittal (top) and tangential (bottom) beam waist in the cavity. The focal waists in the nonlinear crystal are  $w_{\text{sag}} = 10 \mu\text{m}$  and  $w_{\text{tan}} = 17 \mu\text{m}$ .

they are used in pairs [27]. Their dispersion profiles are shown in Figure 3.3(a) and (b). Moreover, by inserting glass windows, any amount of positive dispersion can be introduced into the cavity, depending on the glass type and thickness. In the final configuration, two 12 mm thick fused-silica windows generate over four beam passes each an internal dispersion of about  $3500 \text{ fs}^2$  at a central wavelength of 800 nm. In Figure 3.3(c) and (d) the GD and GDD of the whole cavity are simulated for a varying number of glass plates. Their influence on the NOPO spectra is investigated in the next section.

### 3.3 Experimental results of the NOPO

In previous publications, the scalability of NOPOs has already been examined in detail [28, 51]. There it is shown that the slopes of the signal output power over the pump power follow the typical laser characteristics with a linear progression above the pump threshold. Depending on the output wavelength, the threshold and the efficiency may vary slightly. Nevertheless, sufficient intensities for the subsequent stimulated Raman spectroscopy can be achieved even with moderate pump powers. However, the tuning behavior and the width of the individual output spectra are essential for the Raman measurements and their resolution. This in turn is regulated via the internal round-trip dispersion. In the following section, the influence of the dispersion is examined more closely. Subsequently, the NOPO characteristics in the final configuration are presented.

#### 3.3.1 Impact of dispersion

As discussed in Section 2.3.2 the internal dispersion causes mainly two effects. On the one hand, it affects the length by which the resonator mirrors needs to be shifted for tuning the output wavelength. Only the spectral components that overlap spatially and

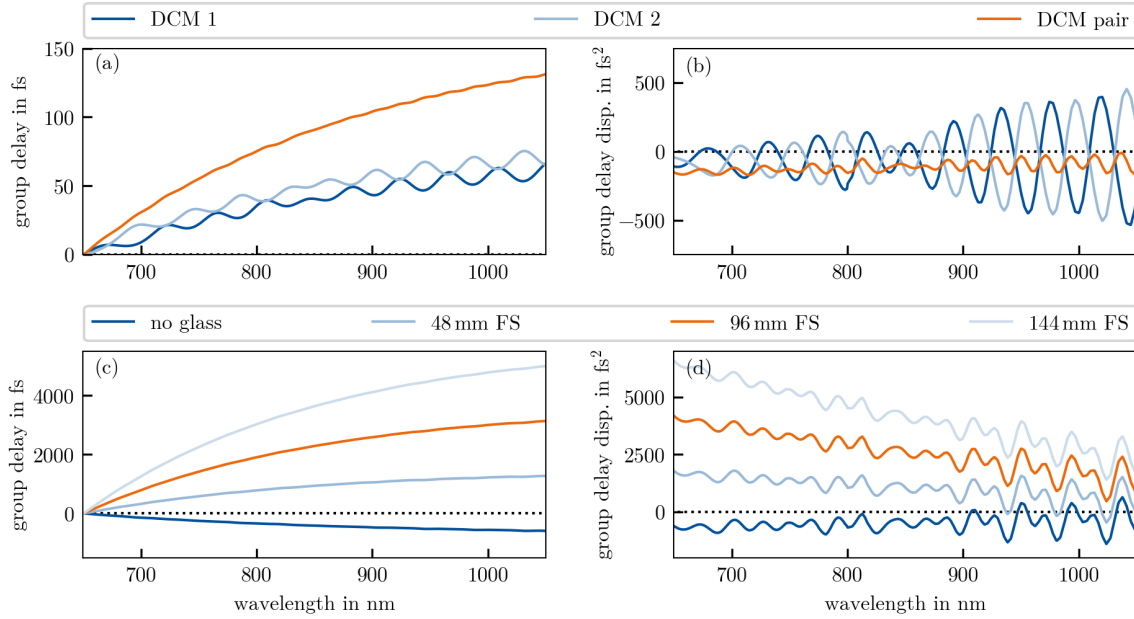


Figure 3.3: Top: (a) GD and (b) GDD of the used individual DCMs 1 and 2 in dark and bright blue, as well as of the DCM pair in orange. Bottom: (c) Simulation of the internal cavity GD and (d) GDD (right) for zero to three inserted fused silica (FS) plates. The final configuration, inserting two FS windows, which corresponds to 96 mm glass per round-trip is highlighted in orange. The remaining ripples in the GDD occur from the DCMs.

temporally with the pump pulses in the nonlinear crystal are amplified. Besides the repetition rate of the pump radiation, this depends on the respective color round-trip time and thus on the group delay dispersion and the cavity length. This relationship is already illustrated in the Figures 2.6(b) and 3.3(c). Furthermore, the NOPO internal dispersion defines the bandwidth of its output spectra. Since the pump pulses represent a fixed gain window, their overlap with a spectrally more dispersed pulse causes a narrower signal wavelength range. For the fast spectroscopy experiments narrow output spectra, but a high tuning rate and thus small mirror shifts are beneficial. A suitable trade-off needs to be found.

In the presented NOPO, the internal dispersion is realized by 12 mm thick windows made of fused silica. To reduce losses in the cavity, they are either protected with a broadband anti-reflection coating or inserted in Brewster's angle into the cavity. Without any glass plate, the NOPO is not stable. All frequencies are simultaneously amplified in the nonlinear crystal and no stable mode can establish. Even with a single glass window, controlled tuning of the output wavelength is difficult. Already small length changes of the cavity by a few micrometers cause a large spectral variation. In particular, the influence of two and three glass plates is investigated. Their respective tuning curves with the output spectra in the frequency domain in relation to the movement of the electronically driven translation stage are shown in Figure 3.4.

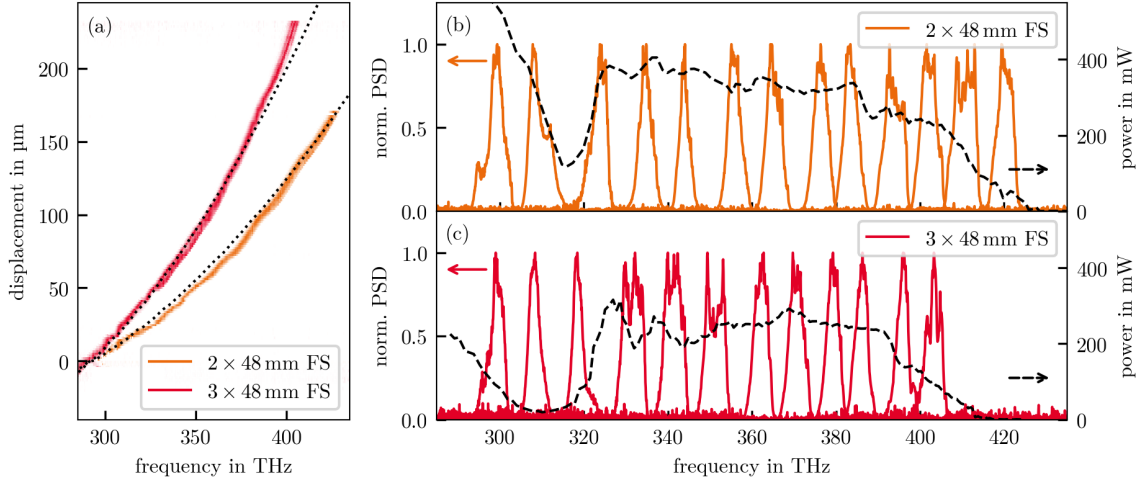


Figure 3.4: (a) The tuning behavior of the NOPO with two (orange) and three (red) 12 mm thick fused-silica windows. The dotted lines indicate the calculated values. (b), (c) Selected spectra for each configuration. The output power over the central frequency is shown in dashed lines.

As shown in the schematic NOPO setup in Figure 3.2(a), each glass window is traversed four times per round-trip in the standing wave cavity. The large optics are each crossed twice on the way there and twice on the way back through the cavity. Thus, one 12 mm thick plate introduces a total of 48 mm material per round-trip. With two FS windows, the cavity mirror must be moved by  $170\ \mu\text{m}$  to scan through the entire spectral range from 290 THz to 430 THz. With one additional plate, the distance increases to  $240\ \mu\text{m}$ , although the spectral range is shortened to 410 THz. Due to the added glass window, additional losses are introduced into the cavity. These losses are not only visible in the reduced tunability and a harder alignment of the oscillator, but also in lower output power. This is shown for two plates with a total of 96 mm introduced fused silica in Figure 3.4(b) and for three plates with 144 mm in 3.4(c) respectively by the dashed lines. With comparable pump powers of about 7 W in the green, the NOPO achieves with two glass plates up to 400 mW output power. An additional plate reduces this value by 100 mW. Likewise, the drop in output power at 320 THz, caused by parasitic second harmonic generation, is stronger with the added glass window. Though, the NOPO starts fluctuating in both configurations, the unstable region is larger in the second case. No spectroscopy experiments can be performed here.

Special attention is paid not only to the tuning range but also on the shape of the output spectra. Individual spectra for both configurations can be seen again in Figure 3.4. However, only slight differences are found here. On average, the oscillator using 96 mm inserted glass emits spectra with a full width at half maximum (FWHM) of 3.8 THz. If the dispersion is increased to 144 mm fused silica, the width is slightly

reduced to 3.6 THz. Nevertheless, the more unstable behavior of the NOPO is also evident here. The width of the individual output spectra fluctuates more than in the previous configuration. Besides very narrowband spectra, there are as well very wide ones with up to 5.8 THz, which corresponds to 14.9 nm. For this reason, the setup with two plates is used for the spectroscopic measurements. The minimal reduction in spectral width does not justify the increased instabilities and challenges in setting up the laser source. Alternatively, other types of glass with better transparency and higher dispersion can lead to a more stable, but narrowband NOPO. Also, the use of a single thick glass block instead of multiple windows may contribute to a better performance. This prevents cavity losses due to fewer surface reflections.

### 3.3.2 NOPO characteristics

The complete tuning range of the NOPO in the final configuration is shown in Figure 3.4 in orange. For the spectroscopic measurements, particularly the spectral range from 365 THz to 400 THz or 750 nm to 820 nm is of interest. This is where the strong oxygen-hydrogen and carbon-hydrogen stretching modes can be detected with the stimulated Raman setup that will be described in Chapter 5. In this section, the focus lies on this finite wavelength region, well away from the degeneracy point and the region of parasitic SHG.

Essentially, after a warm-up period, the NOPO runs very reliable and stable during the day. Nevertheless, it needs to be slightly readjusted after each turning-on to reach the full power and bandwidth. The phase-matching within the nonlinear crystal and though the tuning behavior is highly sensitive even to very small changes in length and angle of the cavity mirrors. For this reason, the laser radiation is newly characterized before each experimental unit. Mainly, the output spectra and power are recorded in relation to the replacement of the piezoelectric actuator. Such a characterization measurement is shown in Figure 3.5. More precisely, this is the calibration curve for the following mixing experiments in Chapter 5.2.

The tuning curve in Figure 3.5(a) is not smooth, but has small irregularities. They are caused by the ripples in the GDD. The individual spectra support pulse durations as short as 130 fs. However, the pulses directly out of the NOPO are not Fourier limited, but typically slightly shorter than the pump pulses [25]. For the subsequent stimulated Raman spectroscopy experiments, these longer pulses are beneficial as they provide a better temporal overlap of the detection beams. Therefore, no further compression stages are included. The output power, plotted in Figure 3.5(c) decreases with smaller wavelength and declines towards the edge of the phase-matched region. Nevertheless, these power differences are of no significant importance for the spectroscopy applications. In addition, the beam profile is pictured in the inset 3.5(b). Although it



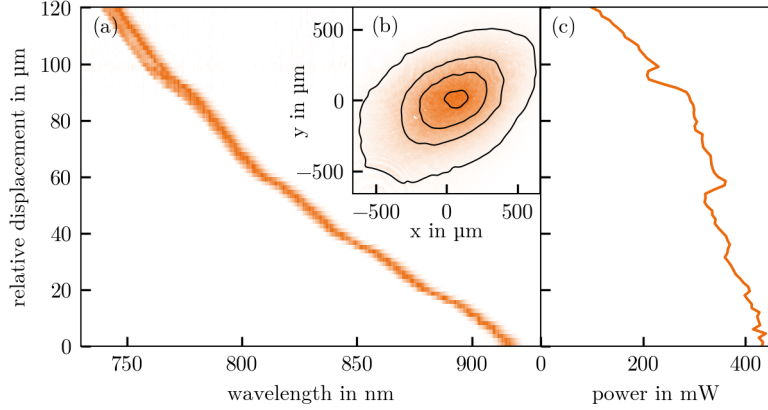


Figure 3.5: Tuning characteristic of the NOPO from an actual measurement (refer to Section 5.2), showing (a) the output spectra and (c) power over the relative cavity displacement. The inset (b) shows the elliptic beam profile with a Gaussian shape.

shows a slight ellipticity, it still features a Gaussian beam shape with excellent focusing properties.

All in all, the presented NOPO is an ideal light source for stimulated Raman spectroscopy. With the fast-moving piezoelectric actuator, the output spectrum is tuned within the shown range in less than 10 ms. Hence, real-time spectroscopy is enabled. Actual measurements with the demonstrated system are shown in Chapter 5. In the outlook in Chapter 6 further improvements for the NOPO are suggested. Besides a possibility to extend the spectral range for the experiments, a transfer of the non-collinear tuning concept to other nonlinear crystals is discussed. Of particular note, a NOPO in the visible spectral range was already realized using the same concept [51]. By a further SHG step, fast tunable radiation in the ultraviolet spectral regime is feasible, which opens up further possibilities for spectroscopy applications. For example in resonance Raman scattering, where the excitation energy is close to the electron transitions of the molecules. It provides a significantly enhanced intensity of the Raman scattering.



## 4 | Theoretical Aspects of Stimulated Raman Scattering

The spontaneous Raman effect was discovered in 1928 by C. V. Raman [52] and earned him the Nobel Prize two years later. Inspired by the blue color of the ocean<sup>1</sup> Raman wanted to study the scattering of light in liquids, as he stated in his noble lecture [54]. During his investigations he observed a new kind of radiation. A small portion of the scattered light comes at different wavelength than the original one. A small part of the photon energy is transferred to the molecules, raising them to a higher energy level. The Nobel Committee recognized the great potential in this discovery, as it provides insights in the structure of molecules and allows the analysis of all different types of materials. At the latest with the development of the laser, which supplies sufficient light intensities, Raman spectroscopy had its breakthrough. Today, it is one of the most used analysis methods, mainly in chemical research and in biomedical imaging. Several techniques and tricks emerged to increase the sensitivity towards smaller probing volumes and shorter detection time scales. In this work, the focus lies on Stimulated Raman Scattering. A method that evolved since 1960 from bulk samples over single cell imaging to measurements of nanoscopic volumes [55]. In addition to the textbooks [15, 16, 56], the following sections are based on a tutorial about coherent Raman scattering [57]. In this special topic article all fundamental basics are brought together.

### 4.1 Spontaneous Raman Scattering

Many physical processes do not only occur spontaneously, but they can be specifically stimulated. For example, the laser is based on stimulated emission instead of spontaneous fluorescence. the NOPO from the first part of this work uses not only parametric fluorescence, but its stimulated amplification. In the same way, there is also a spontaneous and stimulated course in Raman scattering. This chapter starts

---

<sup>1</sup>Unlike the sky, the ocean does not get its blue color from scattering, but from the absorption of the red parts in the visible spectrum. [53]

with the spontaneous scattering processes and their mathematical description. They are based on the the excitation of vibrational energy states in molecules. After the fundamentals, the next chapter describes stimulated Raman scattering, which is used for the spectroscopy experiments in the scope of this thesis.

### 4.1.1 Molecular vibrational resonances

In molecules, the energy levels are not only determined by the electrons, but also by vibrational and rotational movements of the individual atoms against each other. These vibrational modes are quantized and can be excited by infrared (IR) light. Typical excitation wavelengths range from 2500 nm to 20 000 nm, which corresponds to frequencies between 15 THz and 120 THz or  $500 \text{ cm}^{-1}$  and  $4000 \text{ cm}^{-1}$ . The electronic energy levels are far above the vibrational ones, typically in the visible and ultraviolet spectral regime.

To understand what is behind this IR absorption, the description of the nonlinear polarization and its first linear order  $P^{(1)}$  from Chapter 2 must be taken up. In a simple classical model, a molecule can be described by charged masses, representing the atomic nuclei, connected with a spring as bonding. The most simple case, a diatomic molecule, is illustrated in Figure 4.1(a). It is described by two masses  $m_1$  and  $m_2$  holding opposite charges  $\pm q$ . The charge difference of the two masses induces a dipole moment  $p(t) = qx(t)$ . If now a linearly polarized electromagnetic light field  $E(t) = E_0 \exp(-i\omega t)$  hits the molecule, it generates a Lorentz force  $F_L(t) = qE(t)$  and excites the atoms to oscillate around their ground position  $x_0$ . The molecule passes from its ground state to an excited vibrational state, as illustrated in the energy level diagram in Figure 4.1(b). For weak fields, the motion of the masses follows a driven harmonic oscillation

$$\frac{d^2x}{dt^2} + 2\gamma\frac{dx}{dt} + \Omega_R^2x = \frac{F_L(t)}{m}, \quad (4.1)$$

with the damping term  $\gamma$  which represents the radiation losses, the systems resonance frequency  $\Omega_R$  and the reduced mass  $m = m_1m_2/(m_1 + m_2)$ . For excitation close to the resonance ( $\omega \approx \Omega_R$ ) and for small damping ( $\gamma \ll \Omega_r$ ) the solution of this differential equation is an oscillation  $x(t) = x(\omega) \exp(-i\omega t)$  with the well-known Lorentzian function as complex amplitude

$$x(\omega) = \frac{-qE_0/m}{\Omega_R^2 - \omega^2 - 2i\omega\gamma}. \quad (4.2)$$

Extending this simple system to a macroscopic medium with  $N$  particles, the light field generates not only a single dipole moment, but an overall polarization  $P(t) =$

$Np(t)$ . In linear optics, the polarization can be seen as direct response to the electric field with the linear susceptibility  $\chi^{(1)}$  as proportionality factor:

$$P(\omega) = Nqx(\omega) = \varepsilon_0\chi^{(1)}(\omega)E(\omega), \quad (4.3)$$

where  $\varepsilon_0$  is the electric permittivity in vacuum. The linear susceptibility  $\chi^{(1)}$  is a complex material property alike Equation (4.2). Its real part is related to the refractive index  $n(\omega)$ , whereas the imaginary part determines the absorption coefficient of the medium  $\alpha(\omega)$  [58]. Close to the resonance, it applies

$$n(\omega) = n_0 - \frac{1}{2n_0} \operatorname{Re}\{\chi^{(1)}\} \quad \alpha(\omega) = \frac{2\pi}{\lambda_0 n_0} \operatorname{Im}\{\chi^{(1)}\}. \quad (4.4)$$

In these formulas,  $n_0$  is the mean refractive index of the medium and  $\lambda_0$  is the wavelength in vacuum corresponding to the angular frequency  $\omega$ . The course of the linear susceptibility as a function of the excitation frequency is plotted in Figure 4.1(c). The absorption shows a peak at the resonance frequency  $\Omega_R$ . At this frequency the molecule absorbs the light and passes in an excited vibrational state. The absorption bands can be directly measured over IR absorption spectroscopy.

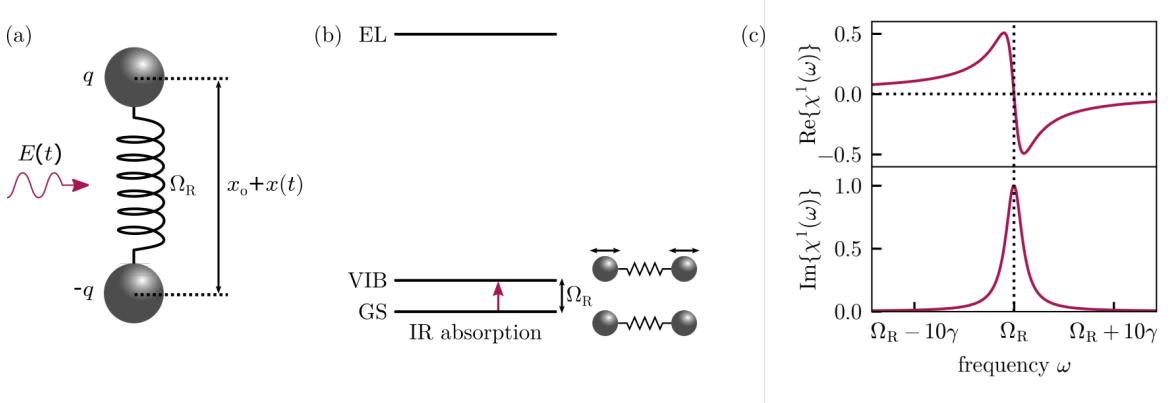


Figure 4.1: (a) Simplified picture of a diatomic molecule as two charged masses connected with a spring. (b) Energy diagram of the IR absorption process. The system is lifted from its ground state (GS) to the vibrational state (VIB) by infrared light with the photon energy  $\hbar\Omega_R$ . The electronic levels (EL) require far more excitation energy. (c) Normalized behavior of the linear susceptibility  $\chi^{(1)}$  across the molecular resonance. The real part (top) is related to the refractive index of the medium. The imaginary part (bottom) is related to the medium absorption and has a strong peak at the resonance frequency  $\Omega_R$ .

### 4.1.2 Spontaneous scattering

Talking about scattering, the frequency of the incident light field  $\omega_P$  is far-away from the resonance  $\Omega_R$ . Thus, the Lorentzian approximation from the previous Section 4.1.1

is not valid anymore. Nevertheless, considering again the diatomic molecule in Figure 4.1(a), an exciting field  $E(t) = A_P \cos(\omega_P t)$  induces a dipole moment  $p(t) = \alpha(t)E(t)$  to the molecule, where  $\alpha(t)$  is the polarizability. The polarizability is a property of molecules and atoms. It is a measure of how strong the different charged particles can be displaced under an external electric field. The higher the polarizability, the easier it is to induce a dipole moment. Its strength depends on the intra-molecular distance  $x$ . Without excitation, this distance oscillates at the resonant frequency  $x(t) = x_f \cos(\Omega_R t)$ , with a small fluctuation amplitude  $x_f$ . For low fluctuations, the polarizability can be expanded as Taylor series around its initial value  $\alpha_0$ , where the molecule rests in its ground position  $x_0$

$$\alpha(t) = \alpha_0 + \left( \frac{\partial \alpha}{\partial x} \right)_0 x(t). \quad (4.5)$$

Combining all the equations the dipole moment is found as:

$$\begin{aligned} p(t) &= \left[ \alpha_0 + \left( \frac{\partial \alpha}{\partial x} x_f \cos(\Omega_R t) \right)_0 \right] A_P \cos(\omega_P t) \\ &= \underbrace{\alpha_0 A_P \cos(\omega_P t)}_{\text{Rayleigh}} \\ &\quad + \underbrace{\frac{1}{2} \left( \frac{\partial \alpha}{\partial x} \right)_0 A_P x_f \cos[(\omega_P - \Omega_R)t]}_{\text{Stokes}} + \underbrace{\frac{1}{2} \left( \frac{\partial \alpha}{\partial x} \right)_0 A_P x_f \cos[(\omega_P + \Omega_R)t]}_{\text{anti-Stokes}} \end{aligned} \quad (4.6)$$

The first term, containing only the pump frequency  $\omega_P$ , describes the Rayleigh scattering. The molecule stays in its ground state and the scattered light has the same frequency as the initial one. The second term with the frequency  $\omega_S = \omega_P - \Omega_R$  shows a red shifted scattering, which is the Stokes Raman scattering. The molecule is moved from the ground state to an excited vibrational state, while the initial field loses energy. The third term with frequency  $\omega_{AS} = \omega_P + \Omega_R$  describes the blue shifted anti-Stokes Raman scattering. The molecule goes from the excited state to its ground level transferring energy to the field. In Figure 4.2(a) the energy diagrams of the three scattering processes are shown.

In a macroscopic picture with  $N$  molecules, the pump field with the frequency  $\omega_P$  induces an overall polarization  $P(t) = Np(t)$  analogue to Equation (4.3) and thus generates the Stokes field  $E_{\text{Stokes}} = A_{\text{Stokes}} \cos(\omega_S t)$ . This leads to the intensity of the Raman shifted light:

$$I(\omega_S) = \frac{\varepsilon_0 c}{2} |E_{\text{Stokes}}(\omega_S)|^2 \propto |x_f|^2 |A_P|^2 \left( \frac{\partial \alpha}{\partial x} \right)_0^2 \quad (4.7)$$

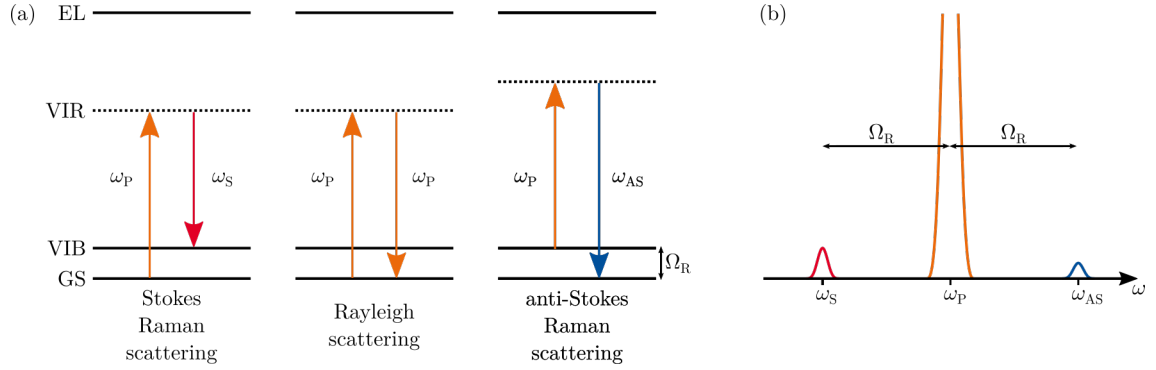


Figure 4.2: (a) Spontaneous Raman scattering energy diagrams: In Stokes Raman scattering the pump light transfers over a virtual energy level (VIR) the system into an excited vibrational state (VIB). Accordingly in Rayleigh scattering the system stays in its ground state (GS) and in anti-Stokes Raman scattering, it falls from its excited state to the fundamental level. The electronic states (EL) are far above the excitation energy. (b) Schematic illustration of the scattered light in the frequency domain: The intensity of the Rayleigh scattering at the initial frequency  $\omega_P$  is much higher than the inelastic Raman scattering.

From this equation it can be seen that the intensity scales with  $|\partial\alpha/\partial x|^2$ , which underlies the requirement of a change in the polarizability  $\alpha$ . Furthermore, it scales with the amplitude of the nuclear motion  $|x_f|^2$ . However, the nuclear motions are not correlated. Each generated field carries a random phase, which causes the spontaneous Raman scattering to be incoherent. Commonly, the intensity is described in terms of a cross section  $\sigma(\omega)$ , which inherits all the material properties and the strength of the frequency dependent Raman response. With the intensity of the pump beam  $I_P \propto |A_P|^2$ , the sample length  $L$  and the number of molecules in the interaction volume  $N$  the total intensity of the Stokes scattered light can be written as

$$I(\omega_S) = NL\sigma(\omega_S)I_P. \quad (4.8)$$

Typical values for the Raman cross section are listed in Table 4.1. Commonly, they are determined as differential cross sections over the solid angle  $sr$  to account for the scattering angle.

Unfortunately, our classical approach does not provide the full picture of the spontaneous Raman scattering process. In thermal equilibrium the ground state is more populated than the excited energy levels. For this reason, experimentally, the Stokes scattering is more intense than the anti-Stokes scattering as illustrated in Figure 4.2(b). This only follows from the complete quantum mechanic description. However, this calculation goes beyond the scope of this thesis. It can be looked up in [56].

molecule		frequency shift in $\text{cm}^{-1}$	cross section $d\sigma/d\Omega$ in $\text{cm}^2/\text{sr}/\text{molecule}$
nitrogen	$\text{N}_2$	2330	$5.5 \times 10^{-31}$
oxygen	$\text{O}_2$	1556	$6.77 \times 10^{-31}$
carbon dioxide	$\text{CO}_2$	1338	$8.31 \times 10^{-31}$
water	$\text{H}_2\text{O}$	3657	$13.75 \times 10^{-31}$
ozone	$\text{O}_3$	1103	$16.50 \times 10^{-31}$
methane	$\text{CH}_4$	2917	$40.15 \times 10^{-31}$

Table 4.1: Raman cross section for typical molecules from our atmosphere. The results were taken with an excitation wavelength of  $\lambda_P = 488 \text{ nm}$  [16].

## 4.2 Stimulated Scattering

This chapter will first discuss coherent Raman scattering in general. Subsequently, the stimulated Raman process, which is used for the measurements in the context of this thesis, is described in more detail.

### 4.2.1 Coherent Raman scattering

For a classical description of the Coherent Raman scattering (CRS) process, the model from Figure 4.1 needs to be extended. In addition to the pump field at  $\omega_P$ , the Stokes field at frequency  $\omega_S$  is added as second initial wave. The total field in complex notation can be written as

$$E(t) = A_P \exp(-i\omega_P t) + A_S \exp(-i\omega_S t) + c.c. \quad (4.9)$$

The diatomic molecule still follows the movement of a driven harmonic oscillator like described in Equation (4.1). However, the driving force  $F(t)$  depends now on both fields. As the pump and Stokes frequencies are far from the resonance  $\Omega_R$ , the vibrational mode cannot be excited efficiently. Nonetheless, the surrounding electrons follow the incident fields. If the fields are sufficiently intense, nonlinear electron motions can occur at the beating frequency  $\Omega = \omega_P - \omega_S$ . The mathematical derivation of the force can be found in [16]. It is given by

$$F(t) = \left( \frac{\partial \alpha}{\partial x} \right)_0 [A_P A_S^* \exp(-i\Omega t) + c.c.]. \quad (4.10)$$

Analogous to the solution in Equation (4.2) for the spontaneous scattering, the molecule starts an oscillation at the beating frequency  $x(t) = x(\Omega) \exp(-i\Omega t) + c.c.$ . The vibrational amplitude

$$x(\Omega) = \frac{1}{m} \left( \frac{\partial \alpha}{\partial x} \right)_0 \frac{A_P A_S^*}{\Omega_R^2 - \Omega^2 - 2i\Omega\gamma} \quad (4.11)$$



follows again a Lorentzian function. And analogous to Equation (4.3) an overall polarization  $P$  is found depending on the polarizability  $\alpha(t)$ . It splits into a linear part  $P_L = N\alpha_0 E(t)$  and into a nonlinear part

$$\begin{aligned} P_{\text{NL}}(t) &= N \left( \frac{\partial \alpha}{\partial x} \right)_0 \left[ x(\Omega) e^{-i\Omega t} + c.c. \right] \times \left[ A_P e^{-i\omega_P t} + A_S e^{-i\omega_S t} + c.c. \right] \\ &= P(\omega_{\text{AS}}) e^{-i\omega_{\text{AS}} t} + P(\omega_{\text{CS}}) e^{-i\omega_{\text{CS}} t} + P(\omega_{\text{P}}) e^{-i\omega_{\text{P}} t} + P(\omega_{\text{S}}) e^{-i\omega_{\text{S}} t} + c.c. \end{aligned} \quad (4.12)$$

The nonlinear polarization radiates at four different frequencies  $\omega_{\text{AS}} = 2\omega_{\text{P}} - \omega_{\text{S}}$ ,  $\omega_{\text{CS}} = 2\omega_{\text{S}} - \omega_{\text{P}}$ ,  $\omega_{\text{P}}$  and  $\omega_{\text{S}}$  with the complex amplitudes:

$$P(\omega_{\text{AS}}) = N \left( \frac{\partial \alpha}{\partial x} \right)_0 x(\Omega) A_{\text{P}} = 6\varepsilon_0 \chi_{\text{NL}}(\Omega) A_{\text{P}}^2 A_{\text{S}}^* \quad \text{CARS} \quad (4.13a)$$

$$P(\omega_{\text{CS}}) = N \left( \frac{\partial \alpha}{\partial x} \right)_0 x(\Omega)^* A_{\text{S}} = 6\varepsilon_0 \chi_{\text{NL}}^*(\Omega) A_{\text{S}}^2 A_{\text{P}}^* \quad \text{CSRS} \quad (4.13b)$$

$$P(\omega_{\text{P}}) = N \left( \frac{\partial \alpha}{\partial x} \right)_0 x(\Omega) A_{\text{S}} = 6\varepsilon_0 \chi_{\text{NL}}(\Omega) |A_{\text{S}}|^2 A_{\text{P}} \quad \text{SRL} \quad (4.13c)$$

$$P(\omega_{\text{S}}) = N \left( \frac{\partial \alpha}{\partial x} \right)_0 x(\Omega)^* A_{\text{P}} = 6\varepsilon_0 \chi_{\text{NL}}^*(\Omega) |A_{\text{P}}|^2 A_{\text{S}} \quad \text{SRG} \quad (4.13d)$$

The nonlinear susceptibility  $\chi_{\text{NL}}$  is a material quantity, which describes the frequency response of the material to the incoming fields. Similar to the vibrational oscillations in Equation (4.11) it follows a complex Lorentzian function

$$\chi_{\text{NL}}(\Omega) = \frac{N}{6m\varepsilon_0} \left( \frac{\partial \alpha}{\partial x} \right)_0^2 \frac{1}{\Omega_{\text{R}}^2 - \Omega^2 - 2i\Omega\gamma}. \quad (4.14)$$

The progression of the nonlinear susceptibility is alike the one of the linear susceptibility shown in Figure 4.1(c). It is stronger the closer the difference frequency  $\Omega$  is to the resonance frequency  $\Omega_{\text{R}}$ . Further on, the nonlinear susceptibility is highly dependent on the coupling term  $(\partial\alpha/\partial x)_0$ , which links the electron motions with the nuclear modes.

The buildup of this nonlinear polarization is illustrated in Figure 4.3(a). The beating of the two frequencies in the total incident field  $E(t)$  drive the molecular vibration  $x(t)$  at the resonance frequency  $\Omega_{\text{R}}$ . This vibration results in a changing polarizability and mixes with the incident field to a nonlinear polarization, generating the four frequencies  $\omega_{\text{AS}}$ ,  $\omega_{\text{CS}}$ ,  $\omega_{\text{P}}$  and  $\omega_{\text{S}}$ . The different processes are named: Coherent anti-Stokes Raman Scattering (CARS), Coherent Stokes Raman Scattering (CSRS), Stimulated Raman Loss (SRL) and Stimulated Raman Gain (SRG). The energy level diagrams in Figure 4.3(b) show the involved fields for each process. Note, that they do

not provide any information about either the field intensities nor of the energy state of the molecule (compare Figure 4.5).

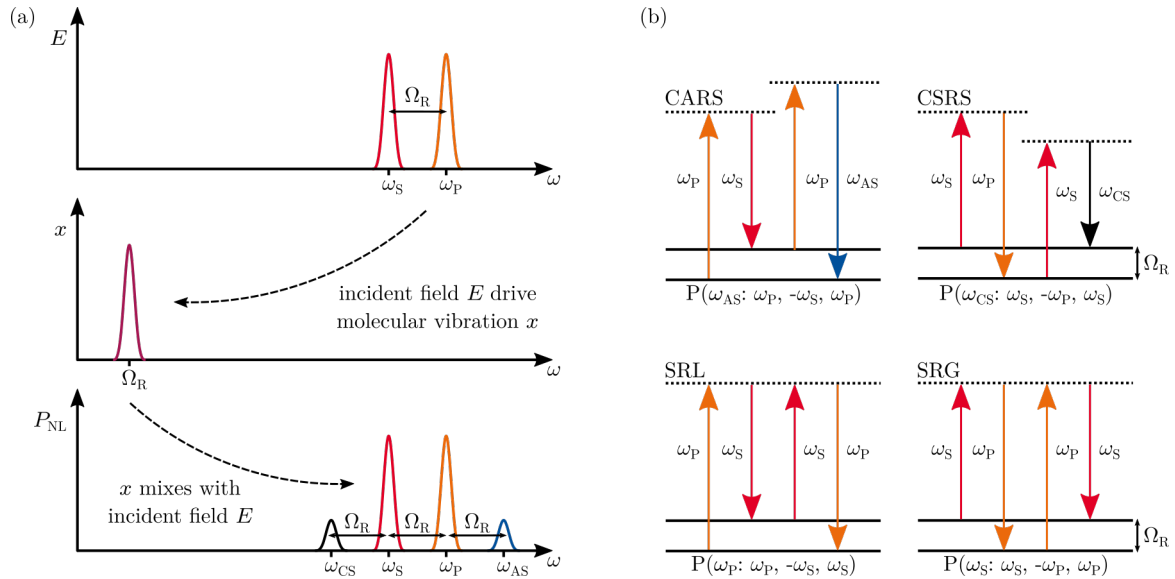


Figure 4.3: (a) Illustration of the coherent Raman process. (b) Energy level diagrams of the four stimulated Raman processes. The first argument in the polarization amplitude denotes the frequency of the generated wave and the following ones after the colon indicate the frequencies of the involved input waves.

CSRS is not often used in laboratory operations. The generated frequencies  $\omega_{CS}$  are red-shifted with respect to the input fields and are often in competition with fluorescence signals. In contrast, the CARS process generates blue-shifted frequencies  $\omega_{AS}$ . Here, the measurements are less noisy and better detectors are available. However, CARS suffers from a non-resonant background. There is an other four wave mixing process, which scatters the light to the frequency  $\omega_{AS}$ , even if the difference between pump and Stokes does not match the molecular resonance. SRG and SRL are discussed in more detail in the next section.

## 4.2.2 The Stimulated Raman scattering process

The Stimulated Raman scattering process (SRS) includes the stimulated Raman gain (SRG) and loss (SRL) introduced in the last section. The energy level diagrams from Figure 4.3(b) already hint, that both processes are linked together as exact the same fields are involved. Their nonlinear susceptibilities from Equation (4.13d) and (4.13c) are connected over  $\chi_{NL} = \chi_{SRL} = \chi_{SRG}^*$ . In this section we continue this considerations.

Keeping the classical model from the previous parts, a pump and a Stokes field generate a nonlinear polarization  $P_{SRL}$ , which itself produces a weak field at the pump frequency  $E_{SRL} = A_{SRL} \exp(-i\omega_P t) \exp(i\phi)$ . The generated field can have a phase difference  $\phi$  compared to the initial pump field. Its complex amplitude depends according

to Equation (4.13c) to the nonlinear susceptibility  $A_{\text{SRL}} \propto P_{\text{SRL}} \propto \chi_{\text{NL}} |A_{\text{S}}|^2 A_{\text{P}}$ . The overall intensity at the pump frequency is given by the individual intensities and the interference term

$$I(\omega_{\text{P}}) = \frac{\varepsilon_0 c}{2} |E_{\text{P}} + E_{\text{SRL}}|^2 \propto |E_{\text{P}}|^2 + |E_{\text{SRL}}|^2 + [E_{\text{P}} E_{\text{SRL}}^* + E_{\text{P}}^* E_{\text{SRL}}] \\ \propto I_{\text{P}} + I_{\text{SRL}} + 2I_{\text{P}} I_{\text{SRL}} [\text{Re}\{\chi_{\text{NL}}\} \cos \phi + \text{Im}\{\chi_{\text{NL}}\} \sin \phi]. \quad (4.15)$$

The intensity of the weak field  $I_{\text{SRL}}$  in the second term is negligible in comparison to the one of the pump field. However, the mixing term can be significant depending on the phase difference  $\phi$  and the strength of the nonlinear susceptibility  $\chi_{\text{NL}}$ . In Figure 4.5(a) its dependence on the frequency  $\Omega$ , which follows again a Lorentzian function, is plotted. Far from the resonance frequency  $\Omega_{\text{R}}$  the susceptibility becomes small. At resonance, the real part vanishes. The phase amounts to  $-\pi/2$ , so the generated field is  $\pi/2$  retarded with respect to the initial pump field. The same considerations can be

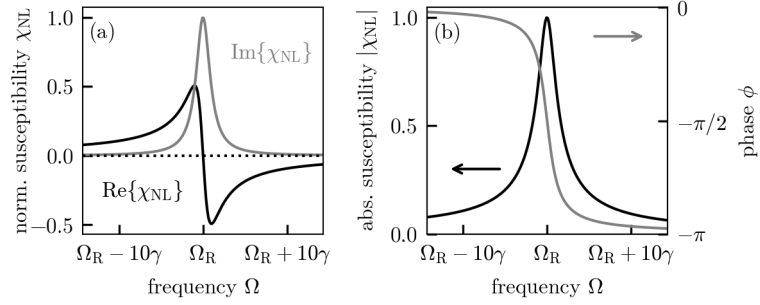


Figure 4.4: Behavior of the normalized susceptibility  $\chi_{\text{NL}}$  over the frequency  $\Omega = \omega_{\text{P}} - \omega_{\text{S}}$  according to Equation (4.14). (a) Real (black) and imaginary (grey) part. (b) The susceptibility expressed in polar form  $\chi_{\text{NL}} = |\chi_{\text{NL}}| \exp(i\phi)$ , decomposed in amplitude and phase. [56]

done for the Stokes field. With the symmetrical susceptibility the phase adds up to  $\phi = \pi/2$ . The overall intensities are found to be

$$I(\omega_{\text{S}}) \propto I_{\text{S}} + 2I_{\text{P}} I_{\text{S}} \text{Im}\{\chi_{\text{NL}}\}, \quad I(\omega_{\text{P}}) \propto I_{\text{P}} - 2I_{\text{P}} I_{\text{S}} \text{Im}\{\chi_{\text{NL}}\}. \quad (4.16)$$

The pump field interferes destructively with the generated weak field, so it appears as loss in intensity  $\Delta I_{\text{P}}$ . In the same time, the Stokes field experiences a gain  $\Delta I_{\text{S}}$ . The process is illustrated in Figure 4.5(b) in the frequency domain.

This simple classical model already describes the most important aspects of SRS. A more complex approach, by inserting the nonlinear polarizations from Equations (4.13) into the wave equations as done in Section 2.1.2 for the parametric gain, results

in the same dependencies. Within the slowly varying envelope approximation, the wave equation for the pump and the Stokes field are [16, 57]

$$\frac{\partial A_S}{\partial z} = \frac{i\omega_S}{2n_S\epsilon_0 c} P(\omega_S) \quad \text{and} \quad \frac{\partial A_P}{\partial z} = \frac{i\omega_P}{2n_P\epsilon_0 c} P(\omega_P). \quad (4.17)$$

In this way, a stimulated Raman gain  $g_R I_P$  can be found, which is related to the imaginary part of the nonlinear susceptibility. The detailed solution is given in Appendix B. It leads to the SRG and SRL intensities, which can be described via the coupled equations [59]

$$\frac{\partial I_S}{\partial z} = g_R I_P I_S, \quad \frac{\partial I_P}{\partial z} = -\frac{\omega_P}{\omega_S} g_R I_P I_S. \quad (4.18)$$

The gain and loss quantities are linked by  $\Delta I_P = -(\omega_P/\omega_S)\Delta I_S$ . The pump beam loses more energy, than is transferred to the Stokes beam. The residual energy remains in the molecule. This can be seen in the energy level diagrams in Figure 4.5(a). In contrast to the ones in Figure 4.3, they are not depicted in terms of fields, but of intensities. As in the spontaneous Raman process, SRS lifts the system from its ground state (GS) via a virtual energy level (VIR) into an excited vibrational state (VIB). Thereby a pump photon is transferred into a Stokes photon. Nevertheless, their formation is based on different mechanisms. Spontaneous Raman scattering is an inelastic scattering process with low probability, whereas SRS is a coherent interaction between two beams. This is somehow similar to the differences between fluorescence and the stimulated emission of radiation.

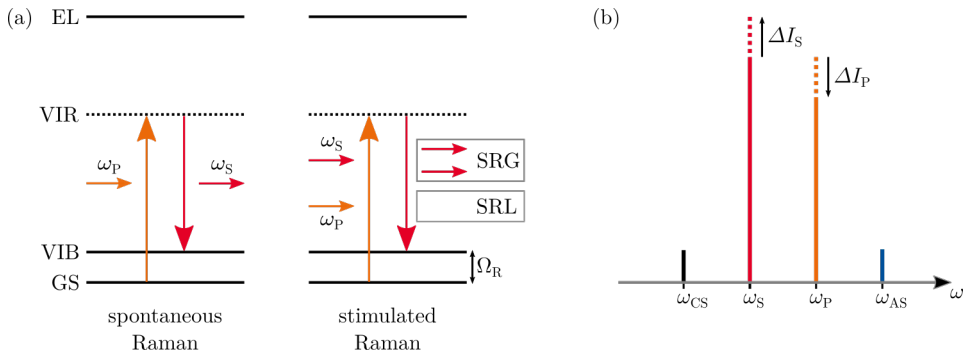


Figure 4.5: (a) Energy level diagrams of spontaneous and stimulated Raman scattering. In the coherent case, the extinction of the pump photon is called stimulated Raman loss (SRL) and the generation of the additional Stokes photon stimulated Raman gain (SRG). (b) Illustration of the SRS process in the frequency domain. In contrast to CARS and CSRS, SRS does not generate new frequencies, but appears as intensity loss  $\Delta I_P$  and gain  $\Delta I_S$  on the pump and Stokes beam.

Indeed, it is possible, using SRS to build a Raman laser. However, the Raman gain is quite low compared to the one of usual laser media. Therefore, it is often

compensated by increasing the interaction length of the active medium utilizing a fiber [59]. On the other hand, in microscopy, the SRL or SRG is measured to get access to the vibrational information of the investigated samples. Here, it is more common to express the intensity changes in dependence of a cross section as done for the spontaneous case in Equation (4.8):

$$\Delta I_P \propto N\sigma(\Omega)I_P I_S, \quad \Delta I_S \propto N\sigma(\Omega)I_P I_S. \quad (4.19)$$

Besides, spontaneous scattering can be considered as stimulated Raman process out of vacuum fluctuations [57]. Vacuum fluctuations are present in all electromagnetic modes, including the Stokes Mode with frequency  $\omega_S = \omega_P - \Omega$ . However, they run in any direction and have random phases, so that only incoherent fields can be generated. Inserting the fluctuations  $\delta I_P$  in Equation (4.16) leads to

$$\delta I_S(L) \propto \delta I_S(0) + 2I_P \delta I_S(0) \text{Im} \{ \chi_{NL} \}. \quad (4.20)$$

The first term is negligible, but the second one is amplified via the pump radiation and the simulated Raman gain. Thus, it can be shown that the inelastic scattering depends on the nonlinear susceptibility  $I_{\text{spon.}} \propto \text{Im} \{ \chi_{NL} \}$ . Likewise, the cross sections in the Equations (4.8) and (4.19) coincide and measurements of the SRL and SRG give direct access to the Raman spectra. In real-life experiments, the stimulated signals are generally three orders of magnitude higher, than the spontaneous ones. However, typical values are in the range  $\Delta I_P / I_P \sim 10^{-4}$  to  $10^{-7}$ . In the next Chapter, techniques to measure the small signals hidden in the laser noise, are shown.



## 5 | Experimental realization of a Stimulated Raman Scattering setup

After the presentation of the tuneable laser source and the theoretical aspects of SRS, this Chapter covers the actual measurements. A big advantage of the SRS in combination with the fast tunable NOPO is the high acquisition speed. To enable a classification, different techniques to achieve fast stimulated Raman spectroscopy are presented. Then, the measurement setup is shown and the measurement principle is introduced as an interplay between laser tuning and time-resolved detection. Firstly, it is used for concentration determination in different solutions. Explicitly, mixing processes in a water-isopropanol solution are observed in real-time to highlight the remarkable detection speed. Furthermore, different plastic samples are investigated. Finally, even microplastic particles (MP) floating inside a cuvette filled with water are analyzed. With a temporal resolution of 8 ms, the tiny particles are detected when they cross the detection beams. In the future, the presented technique may be used for fast MP detection in water flows.

### 5.1 Measurement principle

Now that the origin of SRS-signals has been discussed in the theoretical considerations, the question is how to measure them. Lock-in amplifiers find application everywhere, where small, alternating signals are to be extracted from a large noise background. They are electronic devices, which can convert a noisy ac-signal into a detectable dc-output via phase-sensitive detection. Its input is multiplied with a reference signal and passes a low-pass filter so that only the frequency of interest remains from all frequency components. A more detailed explanation of lock-in amplifiers is given in the Appendix C. Lock-In amplifiers are used in the vast majority of SRS-experiments. As they need alternating signals, typically either the pump or the Stokes beam is modulated by an acousto- or electro-optic modulator. If the difference between pump and Stokes frequency corresponds to a Raman-active transition of the sample, the modulation transfers to the respective other beam. This is measured at a photodiode,

which passes the signal to the lock-in amplifier. There, it is isolated from the strong background and read out. Lock-in amplifiers can reach integration times in the order of microseconds. However, only a single spectral line, which corresponds to a single difference frequency between pump and Stokes beam, can be observed in this way. For broadband measurements multiplex SRS and spectral focussing established in addition to the wavelength tuning [60]. These methods are presented in the following Section. Afterwards, a detailed description of the measurement principle used in the scope of this thesis is given.

### 5.1.1 Multicolor SRS methods

Summarizing the last Chapter, stimulated Raman measurements are based on the fact, that different molecules show different Raman spectra as they own different vibrational states. To interrogate a single Raman line, two laser beams are needed. Their frequencies must be precisely tuned so that their difference frequency matches the vibrational transition of interest. The most obvious way to achieve this is it to shift a narrowband laser in wavelength, as illustrated in Figure 5.1(a). It is very possible with OPOs by adapting the phase-matching conditions. In Chapter 3.1 already some systems were presented, which can tune their wavelength particularly fast [35,49]. Nonetheless, other methods to obtain stimulated Raman spectra at high rates are developed. A variety of techniques and applications of SRS can be found in textbooks [61] or review paper [55,60]. Here, the two most common methods, namely multiplex-SRS and spectral focussing are presented in more detail.

Instead of scanning all spectral lines step by step, multiplex-SRS speeds up the measurements significantly. Using one narrow and one broadband detection beam, allows the recording of several lines simultaneously. However, a simple photodiode with lock-in detection is no longer sufficient for detection. In its place, a spectral splitting, an entire diode array and a multi-channel lock-in are needed. A schematic setup is shown in Figure 5.1(b). Zhang et al. perfected this technique. They achieved acquisition times of 5  $\mu\text{s}$  per SRS-spectrum with help of a 32-channel diode array and a lock-in free detection [62]. Their setup needs a pulse shaper to spectrally narrow down the Stokes beam down to  $20\text{ cm}^{-1}$  for a good resolution. Behind the microscope system, transmission gratings disperse the broadband pump light to fill the photodiode array. The spectral window covers  $200\text{ cm}^{-1}$ . Another method that is frequently used is spectral focussing. Here, the pump and the Stokes beam experience the same linear chirp as depicted in Figure 5.1(c). The difference frequency, which excites the Raman transition, stays constant over the whole pulse length. It is tuned via a temporal delay, which is typically easier to handle than wavelength tuning or spectral decomposition. It can be realized over a motorized stage or a rapid acousto-optic delay line. Alshaykh et al.



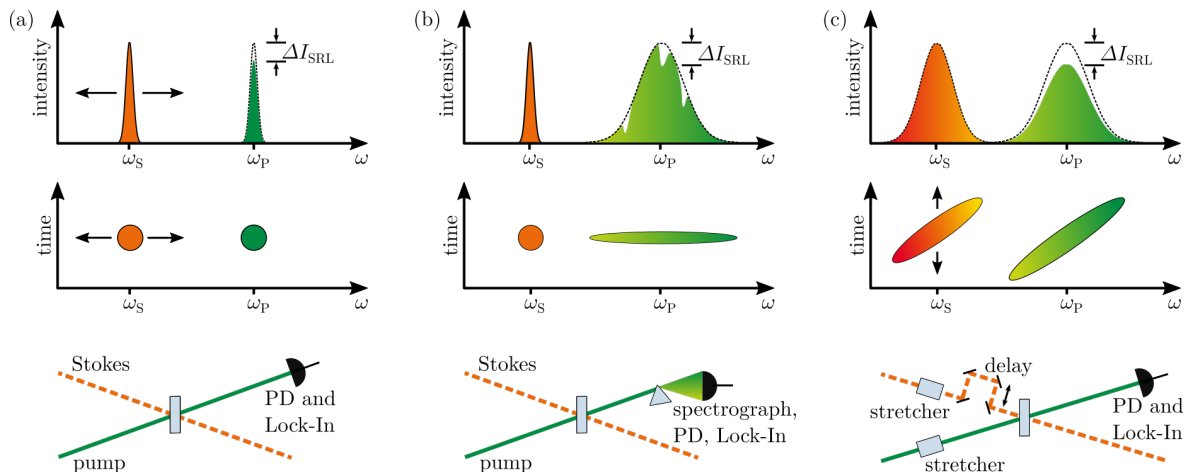


Figure 5.1: (a) Wavelength tuning, (b) multiplex SRS and (c) spectral focusing in the spectral regime (top) and in the time regime (center), as well as a schematic setup respectively (bottom).

succeeded in a sampling rate of 30 kHz with SRS-spectra spanning over  $200 \text{ cm}^{-1}$  [63]. In detection radiation is provided by an Ti:Sapphire pumped OPO. The pump beam is chirped from 120 fs to 1.6 ps passing two glass rods. An acousto-optic programmable dispersive filter or dazzler is used to match the chirp on the Stokes beam, as well as to introduce the temporal delay. They reach a spectral window of  $250 \text{ cm}^{-1}$  with a resolution of  $25 \text{ cm}^{-1}$ . For comparison, Table 5.1 lists the presented systems with their main properties.

	citation	spectral range	coverage	speed	resolution
multiplex SRS	[62]	$200 \text{ cm}^{-1}$	$2900\text{--}3100 \text{ cm}^{-1}$	$5 \mu\text{s}$ per spectrum	$20 \text{ cm}^{-1}$
spectral focussing	[63]	$250 \text{ cm}^{-1}$	$2800\text{--}3050 \text{ cm}^{-1}$	$12.8 \mu\text{s}$ per spectrum	$25 \text{ cm}^{-1}$
this work		$1500 \text{ cm}^{-1}$	$2000\text{--}3500 \text{ cm}^{-1}$	$7.7 \text{ ms}$ per spectrum	$125 \text{ cm}^{-1}$
fast wavelength tuning [35]	[35]	$2700 \text{ cm}^{-1}$	$570\text{--}3300 \text{ cm}^{-1}$	$5 \text{ ms}$ per wavelength step	$12 \text{ cm}^{-1}$

Table 5.1: Multicolor SRS techniques with typical parameters

Stimulated Raman scattering in combination with the NOPO introduced in the previous chapters, utilizes wavelength tuning as the most straight forward technique. The detection unit consists only of one photodiode in combination with the lock-in amplifier. No elaborate optics or spectral diffraction is needed. Nevertheless, it allows for real-time recording of Raman spectra. The covered spectral window exceeds  $2000 \text{ cm}^{-1}$  and thus outperforms multiplex SRS and spectral focussing. The detailed setup and actual measurements follow in the next Section.

## 5.1.2 Experimental setup

For the SRS measurements, two laser beams with different wavelength are required. Their difference frequency determines the scanned Raman transition. The Stokes beam is provided by the thin-disk laser, which powers the NOPO. Its wavelength is fixed at 1030 nm. The pump beam for the SRS-process is produced by the NOPO and is commonly tuned between 750 nm and 850 nm. The piezo actuator in the NOPO is driven with up to 65 Hz via a triangle voltage. Thus spectral lines ranging from  $2100\text{ cm}^{-1}$  to  $3600\text{ cm}^{-1}$  can be probed within less than 10 ms. Both laser systems are inherently synchronized and share the same repetition rate. A delay line is used to temporally overlap their pulses. Moreover, the amplitude of the Stokes beam is altered by means of an acousto-optic modulator (AOM) (IntraAction Corp., AOM-405A1). Modulation depths of up to 75 % are achieved at a modification frequency of 1 MHz. Both, the delay line and the AOM are placed in the IR-beam with fixed wavelength instead of the tuned NOPO output. In this way, dispersion effects are avoided when tuning the NOPO. The two detection beams are spatially superimposed by a dichroic mirror. Subsequently, a lens with a focal length of 50 mm focuses the beams into the sample. Here, beam diameters of about  $25\text{ }\mu\text{m}$  are achieved. With a respective average power of 260 mW, sufficiently high intensities of  $25\text{ kW/cm}^2$  are generated in the probe. In front of the detection unit, a short-pass filter removes the originally modulated Stokes beam. In case of a valid Raman transition, its modulation is transferred to the pump beam. For the detection a large-area photodiode (Thorlabs, FDS100) is used. An additional neutral density filter protects it against saturation. The strength of the SRL-signal, which corresponds to the depth of the transferred modulation, is sensed at the lock-in amplifier and finally passed to an oscilloscope for fast data acquisition and visualization. A schematic of the SRS setup is shown in Figure 5.2.

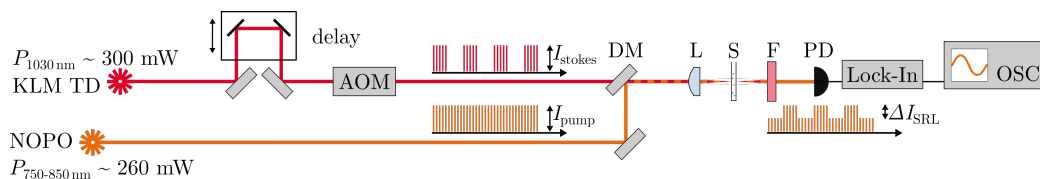


Figure 5.2: Experimental SRS setup: AOM: acousto-optical modulator, L: lens, S: sample, F: shortpass filter, OSC: oscilloscope

For the interaction of AOM, photodiode and lock-in amplifier (Stanford Research Systems, SR865A) the corresponding time scales have to be kept in mind. The reference frequency of the lock-in amplifier and the modulation frequency of the AOM must match exactly. For this reason, the internal reference in the lock-in amplifier is used to drive the AOM. It supports frequencies up to 4 MHz. Generally higher frequencies are

favorable, because in the lower and middle kHz range, the laser noise is rather strong. On the other hand, the large-area photodiode supports only a limited bandwidth. Because of the barrier layer capacitance, the larger the active area, the slower the diode or the lower its cutoff frequency. In parameter studies with the used components, modulation frequencies between 750 kHz and 1 MHz have proven to be suitable with the best signal to noise ratio. Another parameter is the time constant of the lock-in amplifier. It determines the detection bandwidth in which signals different from the reference frequency are filtered out. A long time constant reduces more noise, but increases the response time for the measurements. Too short constants may result in crude signals. For the setup used, time constants of 30  $\mu$ s work best. More details about the measurement procedure and the results are presented in the next Section.

### 5.1.3 Measurement procedure

The primary aim of this work is the high-speed detection of stimulated Raman spectra. For real-time acquisitions, the piezoelectric actuator in the NOPO is periodically moved back and forth at rates between 50 Hz to 80 Hz. Thus, the NOPO's output wavelength periodically changes and the whole spectral range can be sampled in 6 ms to 10 ms. Before the actual fast measurements, the setup must be calibrated each time so that every position of the fast-moving piezo stage can be assigned to a specific spectral line. In a slow measurement the NOPO output is characterized for different voltages at the translation stage. This is demonstrated in Figure 5.3(a)-(c) on the left side. It shows the piezo voltage, the output power and the output spectrum in relation to the relative cavity length. A thermal power sensor (Thorlabs, S425C-L) measures the average power. The spectra are read out by a grating spectrometer (Ocean Optics, USB4000). Each monitoring point takes about 2 s from changing the voltage, waiting for the devices response time to automatically read out the data. Consequently, each voltage value can be mapped to a NOPO wavelength and thus in combination with the Stokes beam of 1030 nm to an interrogated wavenumber. Afterwards the real-time measurements can take place.

As an example, SRS-spectra from a static water sample are recorded. The triangular voltage on the fast piezo actuator has a frequency of 50 Hz. In other words, it takes 10 ms to pass through the entire frequency range for a single SRS-spectrum. The voltage versus time is shown in Figure 5.3(d). It is permanently monitored by the oscilloscope. Likewise, the output power of the NOPO can be tracked via a photodiode. However, the spectrometer is too slow to measure on millisecond time scales. Instead, the slow calibration measurement is used to assign a central wavelength to each time point. Finally, the stimulated Raman signal from the lock-in amplifier is transmitted

to the oscilloscope. A section of the recorded data is shown in Figure 5.3(d)-(g) on the right side.

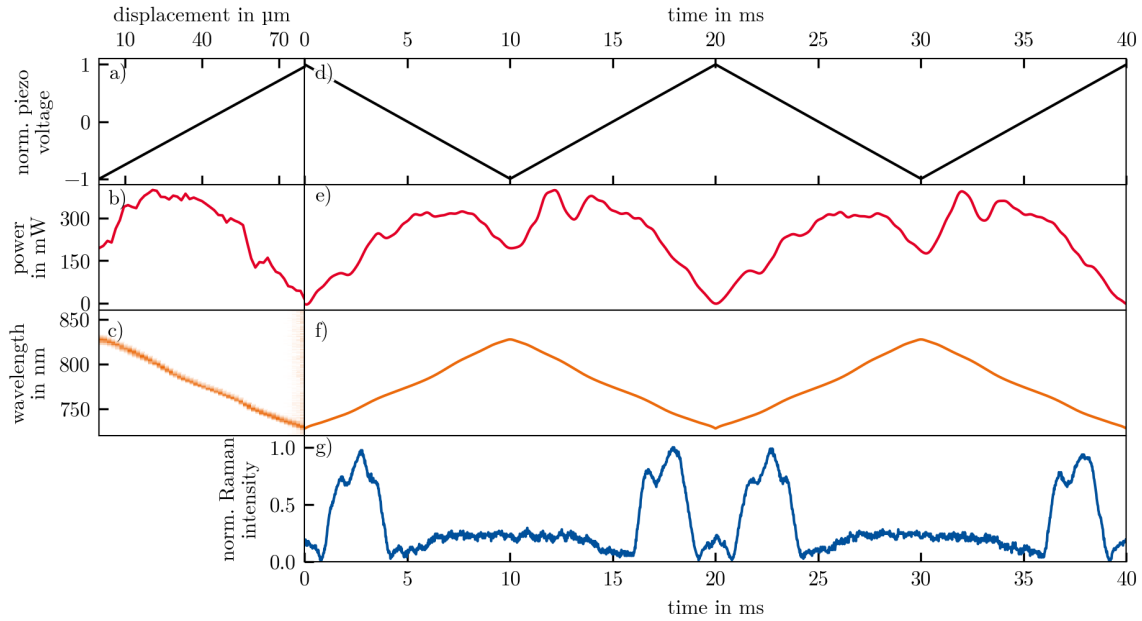


Figure 5.3: Illustration of the measurement principle. Left: slow calibration measurement. (a) piezo voltage, (b) NOPO average output power and (c) spectrum over the displacement of the cavity mirror. Right: fast measurement. Accordingly (d) piezo voltage, (e) power and (f) central wavelength determined by the slow measurement over time. (g) Stimulated Raman signal from the lock-in from a pure water sample.

Basically the measured SRS-spectra agree very well with the known reference spectra from databases or other publications. Nevertheless, the power and the Raman-signal in the Figure 5.3(e) and (g) above reveal a hysteresis in the mirror motion. Their curves show differences in forward and backward direction. For this reason, only every second spectrum is commonly used for analysis. Besides, they own a constant time shift of a few milliseconds, which is already corrected in the graphs. Moreover, the voltage-wavelength mapping at the end points where the piezo actuator changes his direction fails, especially at high speeds. At the edges, the wavelengths are no longer approached correctly. Though in the center part, the mirror movement can be assumed to be linear. Apart from this small inaccuracies, which show up in the absolute wavenumber values, this method detects stimulated Raman spectra very quickly and reliable. The evaluated water spectrum as a function of wavenumber instead of time is shown in Figure 5.4.

However, the spectral resolution is limited by the bandwidth of the individual NOPO output spectra. In Chapter 3.3.1, it was determined to 3.8 THz full width at half maximum, which corresponds to  $125\text{ cm}^{-1}$  and is rather log. For comparison, the other multi-color Raman techniques can achieve resolutions of  $20\text{ cm}^{-1}$  to  $25\text{ cm}^{-1}$  [62, 63].

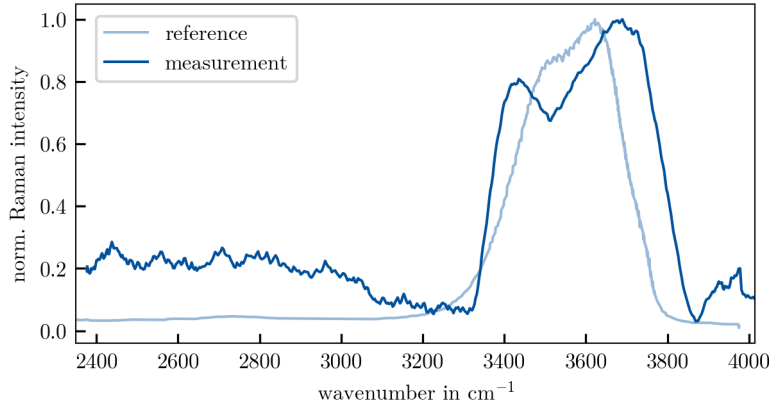


Figure 5.4: Evaluated stimulated Raman spectrum from above measurement (dark blue) in comparison with a reference (light blue) [64].

And even the fiber-based OPO presented in Chapter 3.1 is much slower to tune through, but comes up with an excitation bandwidth of  $12\text{ cm}^{-1}$  [35]. Nevertheless, with over  $1500\text{ cm}^{-1}$ , a much higher spectral range can be covered than with other multiplex or spectral focusing techniques. And the fast tuning of the NOPO in the non-collinear configuration outperforms other SRS-methods using wavelength tuning with common OPOs. The following measurements demonstrate its good performance for fast stimulated Raman spectroscopy.

## 5.2 Mixing processes in liquids

This section deals with the observation of mixing processes in liquids. Besides water, many different substances own very strong Raman lines. Here, isopropyl alcohol and sugar are discussed in more detail. While water with the known molecular formula  $\text{H}_2\text{O}$  has its prominent Raman line in the region  $3050\text{ cm}^{-1}$  to  $3600\text{ cm}^{-1}$  due to the stretching mode of the OH-group, isopropyl alcohol dominates in the wavenumber range  $2800\text{ cm}^{-1}$  to  $3050\text{ cm}^{-1}$ . Based on its chemical composition  $\text{C}_3\text{H}_8\text{O}$ , the CH- and  $\text{CH}_2$ -groups determine the Raman line [65]. The same is true for sucrose, commonly known as table sugar, whose chemical formula is  $\text{C}_{12}\text{H}_{22}\text{O}_{11}$  [66]. Their respective reference Raman spectra [64, 66, 67] are shown in Figure 5.6(a) and 5.7(a).

The intensity of the Raman signal is directly proportional to the number of molecules, as discussed in the theoretical Sections 4.1.2 and 4.2.2. In turn, the molecule count is linearly related to the volume fraction of a compound in the mixture. Therefore, it is possible to conclude the mixing ratios of the involved substances from their respective Raman peak ratio. This is demonstrated in the following parts by means of sugar and isopropanol.

## 5.2.1 SRS on sugar solutions

The experiments presented here use sucrose solutions with different concentrations. They are filled into fused silica cuvettes with a rectangular cross-section of 10 mm, which are commonly used for absorption spectroscopy. They are sketched in Figure 5.5(a). The spectroscopy setup primarily follows the layout given in the previous Section 5.1.2 and is shown again more distinctly in Figure 5.5(b). The samples are placed in the focal point of the two detection beams. The Stokes beam has an amplitude modulation of 1 MHz. The stimulated Raman loss is detected and stored via photodiode, lock-in amplifier and oscilloscope. After balancing noise suppression and response time, the time constant at the lock-in amplifier is set to 30  $\mu$ s.

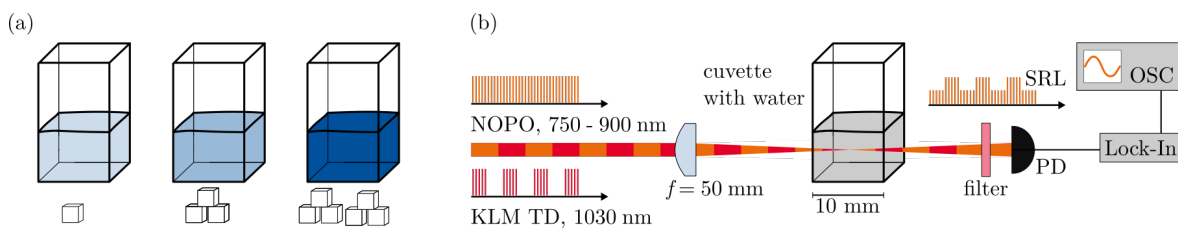


Figure 5.5: (a) Sketch of the cuvettes with sugar solutions. The different concentrations are symbolized by the sugar cubes at the front. (b) Setup of the spectroscopy unit. The Stokes beam is modulated in amplitude with a frequency of 1 MHz and is removed behind the sample with a filter. The transfer of the modulation to the pump beam is detected as Stimulated Raman loss (SRL).

Meanwhile, the cavity mirror on the piezoelectric actuator is moved at a rate of 65 Hz, so that the NOPO is tuned between 755 nm and 900 nm in 7.7 ms. The measured Raman spectra shown in Figure 5.6(a) are averaged from five individual ones taken in 70 ms each. Due to the hysteresis of the fast translation stage, only every other spectrum is considered. Above the measurements, the literature spectra are displayed [64, 66]. Below, the measured SRS-spectra with different concentrations are shown. The Raman signals of water and sucrose are clearly visible, although the resolution is not sufficient to resolve the small structures on the sucrose spectrum. With decreasing concentration, from top to bottom, the sugar peak shrinks. Their size ratio is shown next to the single spectra in Figure 5.6(b). For each spectrum from the adjacent measurements, the Raman intensity ratio  $I_{\text{sucrose}}/I_{\text{water}}$  is determined and plotted above the volume ratio  $V_{\text{iso}}/V_{\text{water}}$ . This was done using the maximum peak values in the respective wavenumber range for water and sugar. The dashed fitting curve shows the expected linear progression. The coefficient of determination  $R^2$  is 0.9876. Using this straight line, it is possible to determine arbitrary concentrations. And with the demonstrated NOPO and its fast tuning concept, this works exceedingly fast in a few milliseconds. The next section shows this even more clearly using real-time observations of alcohol-water mixtures.

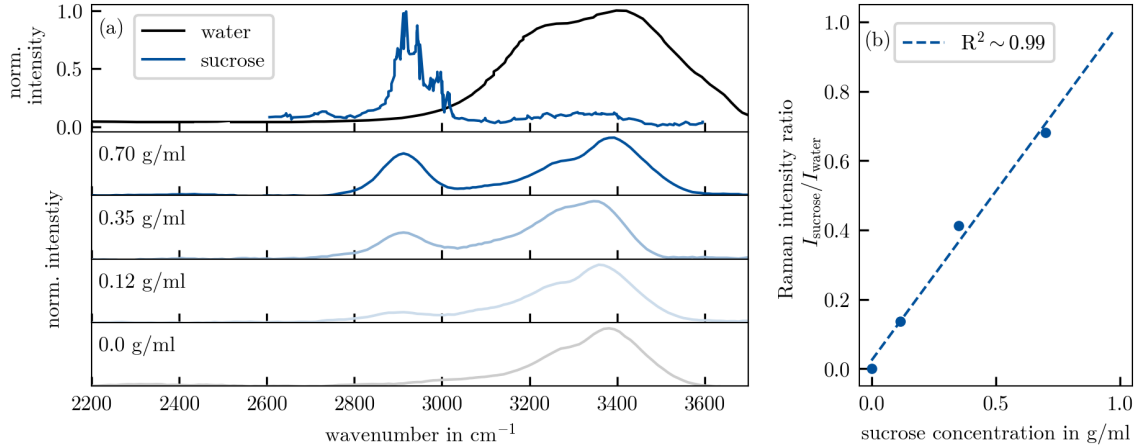


Figure 5.6: (a) Top: Reference spectra of sucrose and water [64, 66]. Bottom: Measured SRS spectra from four sugar solutions with different concentrations. (b) Linear progression of the Raman intensity ratio  $I_{\text{sucrose}}/I_{\text{water}}$  over the sugar concentration. The data points are extracted from the adjacent measurements.

## 5.2.2 SRS on water-isopropanol mixtures

The experimental setup is similar to the previous one. Instead of sucrose solutions, various isopropanol-water mixtures with different mixing ratios are examined. To start, Figure 5.7(a) again shows the reference spectra from the literature of water and isopropyl alcohol [64, 67]. Below in Figure 5.7(b), it displays the measured spectra with different mixing quantities. On the y-axis, the volume fraction of isopropanol  $\varphi_{\text{iso}}$  is shown. It takes values between zero, the sample contains only water, to one, the sample contains only alcohol. The spectra are obtained using the rapid detection method presented in the previous section. Each spectrum is averaged from 17 individual ones, recorded in a total time of 260 ms. The linear relationship of the mixing proportions, here represented by the volume ratio  $V_{\text{iso}}/V_{\text{water}}$ , and the size ratio of the respective Raman signals  $I_{\text{iso}}/I_{\text{water}}$  is illustrated Figure 5.7(c). Again the maximum values of the water and isopropanol peak are used directly. With the exception of the two marginal values, representing pure water or pure alcohol, the data points lie on a perfect straight line. The coefficient of determination is  $R^2 = 0.9954$ . With these findings, mixing processes can be observed very quickly with an real-time concentration determination. This is illustrated in the following experiment.

This measurement is very similar to the previous one. However, no static samples are investigated, but changing mixing ratios. The NOPO output wavelength is tuned between 760 nm and 895 nm with a frequency of 65 Hz. The acquisition of a single SRS-spectrum takes 7.7 ms. The sample setup is sketched in Figure 5.8(a), whereas the continuously recorded SRS-spectra are mapped next to it in Figure 5.8(b). Initially, there are 400  $\mu\text{L}$  of isopropyl alcohol in the examined cuvette. The corresponding

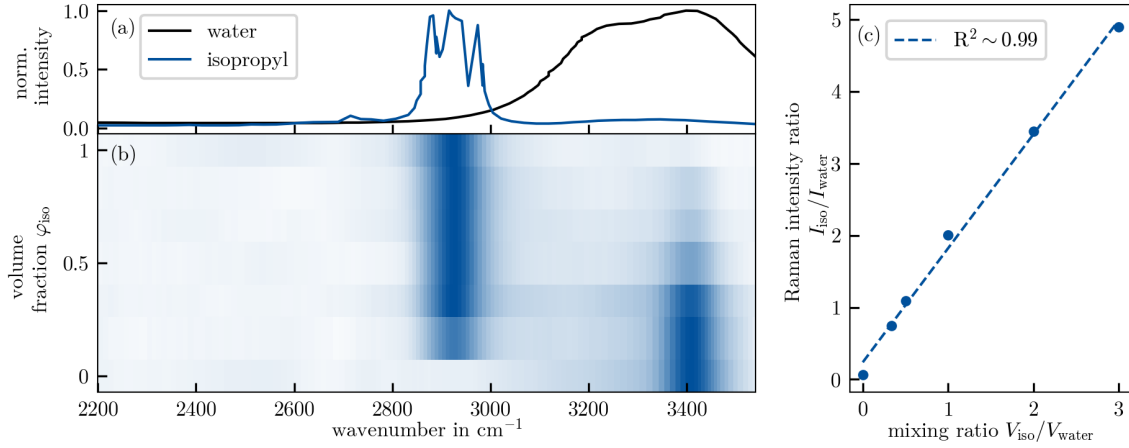


Figure 5.7: (a) Reference spectra of water and isopropyl alcohol [64,67]. (b) Measured Raman spectra of water-diluted isopropyl alcohol solutions with different mixing quantities. (c) Linear progression of the Raman intensity ratio  $I_{\text{iso}}/I_{\text{water}}$  over the mixing ratio  $V_{\text{water}}/V_{\text{iso}}$ . The datapoints are extracted from the adjacent measurement.

Raman spectra are marked with an  $\textcircled{A}$ . They feature only one significant peak around  $2900\text{ cm}^{-1}$  originated from the alcohol, but no water signal. After 1.1 s one water droplet is added. As water-alcohol solutions from strong streaks, the laser radiation gets deflected and does not reach the photodiode correctly. The Raman spectra are disturbed, labeled by a  $\textcircled{B}$ . Another 280 ms later the liquid calms down again. Next to the still dominant isopropanol peak, a weak water signal emerges at  $3410\text{ cm}^{-1}$ . Furthermore, slow, periodic movements within the solution are visible in the SRS-spectra. They can be seen in the area  $\textcircled{C}$  due to a decrease of the water signal and a larger noise background.

Finally, the mixing ratio and thus the volume of the water droplet is determined using the previously derived linear relationship from Figure 5.7(c). The peak intensity ratio after the mixing process is determined to be  $I_{\text{iso}}/I_{\text{water}} \approx 14.6$ . Using the line of best fit from Figure 5.7 and the initial alcohol volume of  $400\text{ }\mu\text{L}$ , a mixing ratio of  $V_{\text{iso}}/V_{\text{water}} \approx 9.1$  and thus a water droplet size of  $44\text{ }\mu\text{L}$  is obtained. In parallel, the average drop volume with the pipette is found to be  $42\text{ }\mu\text{L}$ . For this purpose, a certain volume is filled into the pipette and when emptying, the number of drops are counted. The two values are in close agreement. In this manner, mixing concentrations can be determined in a few milliseconds. The presented setup proves to be suitable for fast spectroscopy and real-time observation of liquids. Further confirmation will be given in the next Section. Here, the detection of microplastic particles directly in a water environment is presented. A topic of growing interest and importance to our society.



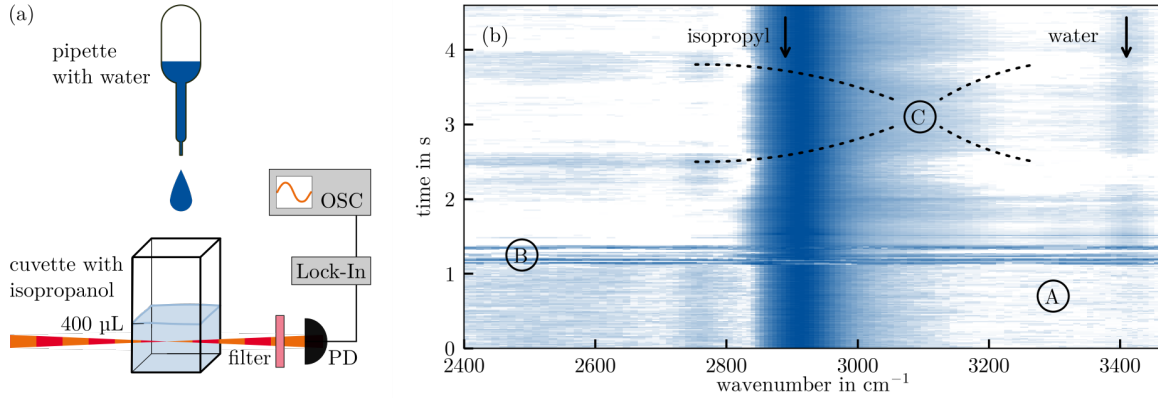


Figure 5.8: (a) Schematic setup of the mixing experiment. The pump and Stokes beams (orange and red) are focused into the sample cuvette. The SRL-signal from the pump beam is processed by the detection unit, consisting of photodiode (PD), lock-in amplifier and oscilloscope (OSC). (b) Time series of Raman spectra observing mixing processes of  $\textcircled{A}$  pure isopropyl alcohol,  $\textcircled{B}$  when adding a drop of water and  $\textcircled{C}$  after the mixing process. The spectra are taken with a rate of 130 Hz, corresponding to a 7.7 ms acquisition time.

### 5.3 SRS of Microplastic Particles

The global distributions of microplastics (MP) challenges the scientific community worldwide. Even in the most remote regions on our planet, MP has been discovered: In the snow of the north pole [68], as well as in Antarctica [69]. On the highest mountains [70] and in the deep sea [71]. In freshwater systems, as well as in their sediments and living organisms [72]. And even our drinking water is polluted by these tiny particles [10]. There are countless publications with MP measurements from all kinds of locations and there are already a vast number of reviews with typically more than one hundred references. To shed some light on this convoluted field, here is a brief overview.

Talking about MP, most people think about plastic packaging, which enter the environment through our waste and sewage. Due to environmental influences they break down to smaller and smaller pieces and accumulate in sediments and waters, where they may enter the food chain. Yet packaging waste is not the biggest source of MP. Every wash cycle can flush hundreds of thousands of microfibers from our synthetic clothes into the wastewater [73]. Road traffic tyre wear is estimated to be responsible for up to 10 % of the MP in the oceans [74]. From the streets through atmospheric transport, they can travel long distances and distribute all around the world. Many paints and coatings are based on polymers. MP hide in cosmetics and personal care products or they are simply created by abrasion of our everyday objects. Researchers estimate in a worst-case scenario, that humans ingest up to 5 g microplastics, the

amount of a credit card, per week [75]. On average, however, the amount is likely to be significant lower. Nevertheless, it can be assumed that adults intake more than 800 particles per day over inhalation and food [76]. The MP can accumulate in the body, but the impact on the human health is not yet understood. This is mainly due their diversity: MP can have different sizes, typically between 1  $\mu\text{m}$  and 5 mm. They can have different shapes like fragments, beads or fibers. And they all consists of different chemical compounds, which of course impact their toxicity.

Anyhow, the research community agrees that more data needs to be collected. But the behavior of MP makes their measurement difficult. They tend to stick together and adhere in tubings or sample containers. Yet a slight breeze is enough to carry them through the air and cross-contaminate samples. Furthermore, a standardized analysis or concepts for the sample collection and preparation are missing. Many already implemented studies are not comparable with each other [77]. Some only sort and count particles by hand. Others go through multiple rinsing and filtration cycles. Some works label the MP with dyes. Other determine the exact type of plastic by spectroscopic methods. An overview of the main tools for MP identification is given in the next Section. Subsequently, SRS measurements with the presented NOPO setup are presented. First, fragments of plastic cups and plastic wrap are investigated. The fast spectroscopy method is brought to bear on measurements of moving microplastics particles in an aqueous environment.

### **5.3.1 Overview of common techniques for microplastics analysis**

By now, there are microplastics studies in great numbers. As a result of their large variety, many reviews have been written, which are typically restricted to specific regions, sample types or detection methods. This overview is mainly compiled from the references [11, 78, 79]. A typical microplastics study proceeds as follows. Firstly, samples are collected at a certain location. This can be sediments, water samples from rivers, oceans and lakes or even animals, especially seafood and fish. Subsequently, the samples have to be processed before they are analyzed in more detail. The animals are dissected and searched for plastics. The sediments are screened too. Since plastics are very light, the surroundings are usually removed by density separation. In most cases, organic material accumulates on the particles and hinders further investigation. Therefore, the particles are purified with chemicals or enzymes, which may not degrade the plastics itself. And in all this, no particles shall be lost, nor shall the samples be cross-contaminated. Here, it already becomes apparent that the preparation is a rather challenging task. In addition, there are no standardized procedures. Not each

study performs every single preparation step and they all use different equipment and chemicals. Hence, the comparability between the various works is strongly limited.

After the preliminary processing, the actual identification and quantification of MP begins. In many cases, the MPs are sorted and counted by hand with the aid of stereomicroscopes. This visual inspection is fast and cost effective, but it does not reveal the nature of the MP. Further on, the result depends greatly on the skill and care of the performing person. Another straightforward analysis technique is the tagging method [80]. The dye Nile Red stains the MP and fluoresces green when excited under blue light. Again, the disadvantage is that the plastic material cannot be identified. In addition, the dye may adhere to organic debris and thus falsify the results. In contrast, chromatographic methods can reveal the type of plastic. Pyrolysis-gas chromatography in combination with mass spectrometry was used to study environmental samples [81]. For this purpose, the MP are strongly heated. The resulting gases are subsequently analyzed for their constituents under a mass spectrometer. Alternatively, the MP are dissolved in strong solvents and then determined by liquid chromatography [82]. Although, both techniques have proven to be reliable, they are not suitable for the analysis of large sample quantities. In one run, which takes about one hour, only a few particles can be investigated.

Therefore, it is not surprising that spectroscopic techniques have become prevalent in MP detection, most commonly Fourier-transform infrared (FTIR) and Raman spectroscopy. Both methods are well-established and non-destructive. They give access to the characteristic vibrational spectra of molecules. Their basic principles are already introduced in the theoretical considerations in Chapter 4.1. In FTIR spectroscopy, the samples are directly irradiated with broadband infrared light. Thereafter, it is observed which wavelength components were absorbed. Instead of scanning all wavelength individually, an interferometer is integrated in front of the sample with a continuously moving mirror. The detected, time dependent interferogram is transferred into the frequency domain via Fourier transformation. In this way, broad spectral ranges are investigated very quickly [83]. FTIR spectroscopy often operates in transmission or attenuated total-reflectance mode. This requires the infrared light to penetrate the plastic samples. Large or colored particles with high absorption are hard to detect. In reflectance mode, the results depend highly on the particle surface and are distorted by scattered light. In addition, FTIR can not be used on aqueous samples, since water absorbs very strongly in the infrared spectral range. In contrast, Raman spectroscopy relies on inelastic scattering. For a detailed description, please refer to Chapter 4.1.2 on page 33. By moving from point spectroscopy to imaging, Raman spectroscopy is superior to FTIR spectroscopy, because of its lower diffraction limit. Especially small particles between 1  $\mu\text{m}$  and 10  $\mu\text{m}$  cannot be resolved by IR spectroscopy. However, Raman microscopy suffers from long integration times for high-quality images. When

scanning over large area samples, the time difference can add up to several hours. Furthermore, an accurate sample preparation is necessary. Many organic and inorganic materials show strong fluorescence lines, which interfere with the scattered detection light. The main advantages and limitations of this two techniques are listed in Table 5.2.

	FTIR spectroscopy	Raman spectroscopy	SRS spectroscopy
foundation	absorption	inelastic scattering	coherent interaction
light source	broadband IR emitter (typ. 500–4000 $\text{cm}^{-1}$ )	continuous wave laser with narrow linewidth	pulsed tunable laser source, two synchronized beams
detector	thermal detector or infrared photodiode	spectrometer	photodiode and lock-in amplifier
detection time	short, typ. 0.1–1 s/spectrum	long integration times, typ. > 1 s/spectrum	limited by laser tuning, $\mu\text{s}\dots\text{s}$ /spectrum (ref. 5.1.1)
spectra quality	depends on particle size and thickness	depends strongly on laser parameters and integration times	depends on light source, typ. lower spectral resolution and coverage
detectable MP	MP > 10 $\mu\text{m}$ , large diffraction limit, total absorption for too thick particles	MP > 1 $\mu\text{m}$ , no upper limit	MP > 3 $\mu\text{m}$ , no upper limit
interferences	strong water absorption, only dry samples	parasitic fluorescence, needs careful sample preparation	no fluorescence, works directly in water

Table 5.2: Analytical spectroscopic techniques for microplastics detection: FTIR, spontaneous and stimulated Raman spectroscopy with their advantages and disadvantages.

The use of stimulated Raman spectroscopy for MP detection is only reported by a few [62, 84], although its benefits are already known from biomedical research. SRS works directly in aquatic samples and is insensitive to parasitic fluorescence, so that less sample preparation is needed. As SRS requires in addition to the pump radiation a Stokes beam with longer wavelength, the diffraction limit is somewhat higher than for spontaneous Raman spectroscopy. However, there is no size limitation for large MP particles. Apparently, the requirements for the light source are much higher. While FTIR and Raman spectroscopy rely on well established systems, SRS needs two synchronized pulsed laser beams. OPOs are the systems of choice. However, the fast tuning concepts introduced in Section 5.1.1 are demonstrated only occasionally in laboratory work and are not yet ready for widespread use. Meanwhile, the commercially available OPOs lose their advantage of potential fast SRS-signal acquisition due to their slow tuning speeds. The NOPO presented in this thesis can overcome this limitation. In future, this technique may pave the way to fast and reliable MP identification. For better comparison, SRS is included in Table 5.2.

### 5.3.2 SRS of static plastic samples

Before studying the small microplastic particles, macroscopic samples are examined. For this purpose, pieces with a diameter around 10 mm are cut out of two different transparent, disposable plastic cups. One is made of polypropylene (PP) and has a very thin wall thickness of about 150  $\mu\text{m}$ . The other cup, which is made of polystyrene (PS) is more stable with a thickness around 450  $\mu\text{m}$ . The setup resembles that of the previous experiments observing the mixing processes. Instead of the cuvettes, the plastic pieces are brought into the focus of the pump and Stokes beams. This task is rather tricky due to the narrow width of the plastic samples. While the large cuvettes could easily be placed in the correct position by hand, a translation stage with a micrometer screw is needed to move the samples into the focal point to find the highest Raman signal. The spectroscopic setup is sketched in Figure 5.9.

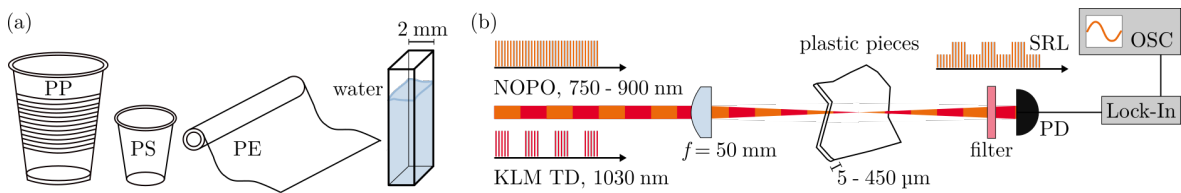


Figure 5.9: (a) Sketches of the investigated items: two disposal plastic cups made of polypropylene and polystyrene, polyethylene cling film and a 2 mm long cuvette filled with water. (b) Setup of the spectroscopic unit. Instead of the large cuvettes, the plastic pieces, which are only a few micrometers thick, are brought into the focus.

Again, the NOPO is tuned at a rate of 65 Hz between 750 nm and 900 nm, which corresponds to an acquisition time of 7.7 ms per spectrum. The recorded SRS spectra, which are illustrated in Figure 5.10(a) and (b) are averaged from 16 single ones, taken in less than 250 ms. As in the former measurements, in comparison with spontaneous Raman spectra from the literature, small structures cannot be resolved, but the shape and position of the SRS spectra agrees very well with the references [85,86]. In addition, both types of plastics can be differentiated clearly. At this point, it is important to note that the selection of the correct time constant at the lock-in amplifier is crucial. If it exceeds 30  $\mu\text{s}$ , the small PS peak at 2900  $\text{cm}^{-1}$  is no longer recognizable but merges with the larger one around 3100  $\text{cm}^{-1}$ . Moreover, the spectra broaden so that the different types are no longer distinguishable.

In preparation for the following experiments on microplastic particles in a water environment, a SRS spectrum of a 2 mm cuvette filled with water is recorded and inserted into the graphics in Figure 5.10. All spectra are normalized with respect to the water signal. While the signal from the 150  $\mu\text{m}$  thin PP is about the same as from the water peak, the signal strength from the 450  $\mu\text{m}$  thick PS is about twice as large. To push the sample thickness to the limit, SRS measurements on cling film are realized.

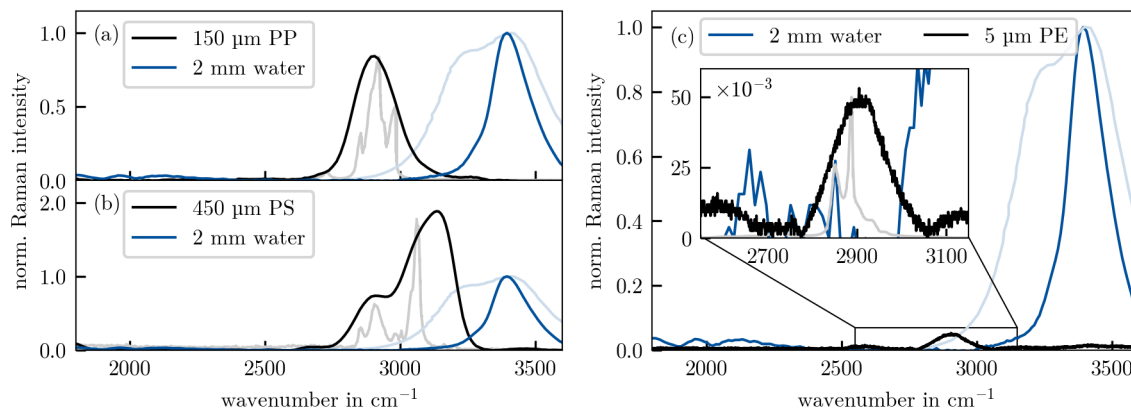


Figure 5.10: Measured SRS-spectra of (a) 150  $\mu\text{m}$  thick polypropylene, (b) 450  $\mu\text{m}$  thick polystyrene and (c) 5  $\mu\text{m}$  thin cling film compared to the Raman signal of 2 mm water. The spectra are normalized with respect to the water peak. The reference spectra [64, 85–87] are plotted in light colors.

According to the packaging information, the plastic wrap is made of polyethylene (PE) and has a thickness of less than 5  $\mu\text{m}$ . Even though it is even more challenging to position the sample correctly, SRS spectra are recorded. However, compared to the 2 mm water cuvette, the signal is 20 times smaller. It is shown in Figure 5.10(c).

This preliminary experiments on static samples show that it is indeed possible to detect MP directly in a water flow. It is also feasible to distinguish between different types of plastics. The main challenge is to guarantee that the particles pass through the focal point of the detection beams. If they intersect the radiation only partially or cross it too far in front or behind the focal point, the weak SRS signal further reduces until it is lost the strong water background. In the next section, evidence of a successful measurement is provided.

### 5.3.3 SRS of microplastics in an aquatic environment

As an example for microplastics, the following experiment is carried out with polyamide (PA) particles. The particles are originally produced as laboratory supplies for separation processes and have sizes between 50  $\mu\text{m}$  and 160  $\mu\text{m}$ . As a reminder, the Gaussian beam diameters of the two detection beams are around 25  $\mu\text{m}$ . Thereby, they can be completely blocked by the particles temporarily. Polyamide has a greater density than water, so the microplastics would sink quickly to the bottom of the sample container. Instead, a 19% sodium chloride solution with a density of 1.13  $\text{g}/\text{cm}^3$  is used as liquid environment. The dissolved ions naturally do not have any molecular vibrations and thus no Raman response. Though the plastic particles are able float constantly through the sample solution, comparable to a snow globe. The used cuvette is narrower than in the mixing experiments. It is made of borosilicate glass and has a rectangular

cross-section with a geometrical path length of 2 mm. The rest of the setup remains unchanged.

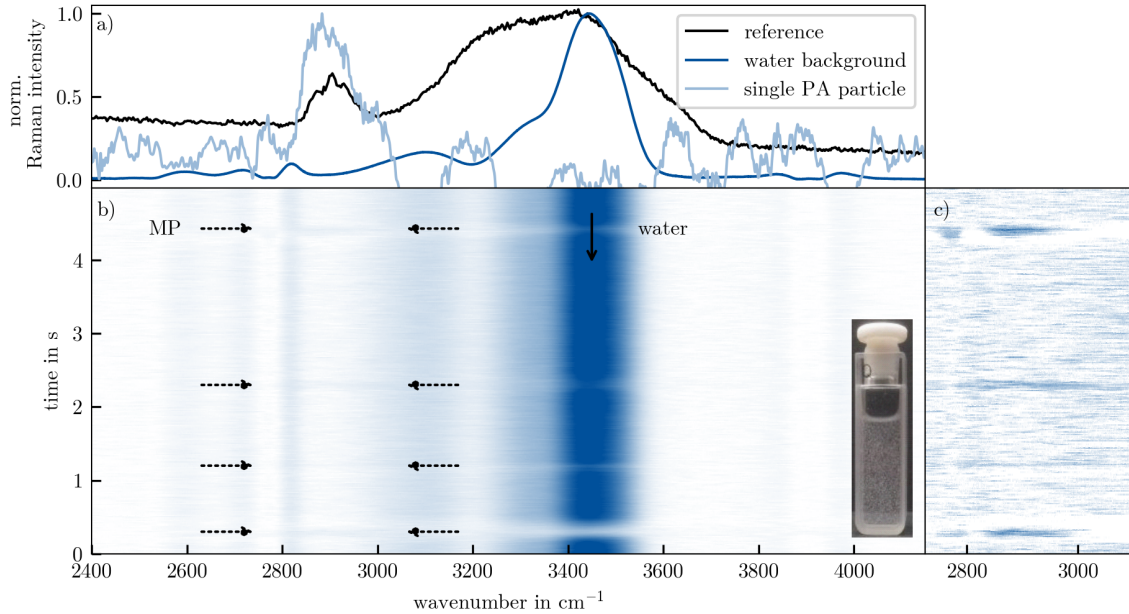


Figure 5.11: Stimulated Raman spectroscopy on polyamide plastic particles. (a) Normalized Raman spectra of the strong water background (dark blue) and a single microplastic particle after background subtraction (light blue) compared to a reference spectrum (black) obtained by spontaneous Raman spectroscopy. (b) 5 s time series of broadband SRS spectra with four polyamide particles crossing the detection area, as well as (c) a cut-out of the Raman signal originated from the plastics with background subtraction.

Figure 5.11(b) shows a time series of SRS-spectra from the described sample with a total duration of 5 s. The NOPO is tuned at 60 Hz between 710 nm to 830 nm. This corresponds to a detection time of 8.3 ms for one single spectrum over a wavenumber range from  $2300\text{ cm}^{-1}$  to  $4300\text{ cm}^{-1}$ . Most prominent is the strong Raman signal from the water solution at  $3450\text{ cm}^{-1}$ . Though, at 0.3 s, 1.2 s, 2.3 s and 4.4 s a decrease appears. Instead, a weak signal emerges at  $2890\text{ cm}^{-1}$ , illustrated by the dashed arrows. This is caused by four plastic particles crossing the detection beams. It needs to be considered, that the Raman signal from 2 mm water line is more than ten times stronger than the small particles with diameters around  $100\text{ }\mu\text{m}$ . To avoid an overloading of the water peak at the lock-in amplifier, it is necessary to work in a low sensitivity regime. This in turn causes the poor microplastics signal. To better highlight the signal, it is shown after subtracting the strong background in Figure 5.11(c). Additionally, a single spectrum of one particle is illustrated in Figure 5.11(a). For comparison, a spontaneous Raman spectrum of the same particles in a water environment is given. More details of its acquisition can be found in [88]. It is seen, that their positions along the wavenumber axis agree very well.

Finally, the parametric oscillator proves to be an excellent light source for stimulated Raman spectroscopy. Especially in the important field of microplastics, it can lead the way for a fast detection and identification of these particles. The shown measurements covered a wavenumber range of more than  $1500\text{ cm}^{-1}$  in combination with short detection times around 8 ms. Still, there are more ideas for further improvements, which are presented in the Outlook 7.



## 6 | Conclusion

The main achievement of this thesis was merging the fast tunable NOPO with stimulated Raman spectroscopy experiments. Both had already been realized independently, but only in combination they allow for real-time observations in fluids. This technique may play an important role in the future, not only to monitor microplastics. To achieve this goal, insights into the construction of optical parametric oscillators are needed, as well as knowledge of coherent Raman scattering. Both techniques are based on nonlinear effects, which are based on related effects caused by nonlinear polarization in an optically active medium. Their origins were reviewed and mathematically described in the two theoretical Chapters 2 and 4. The experimental findings are summarized in the following.

### Experimental realization of the NOPO

The NOPO is characterized by an excellent tunability over an ultra-broad spectral range. Its core, a 2 mm long BBO crystal, gets pumped at a noncollinear angle and supports a wide phase-matching range from 650 nm to 1030 nm with a significant gap at 900 nm caused by parasitic effects. A fast piezoelectric actuator is used to control the cavity length and thus to shift the central output wavelength of the spectrum. This allows control the entire spectral range in a few milliseconds. The slightly elliptical beam profile shows a Gaussian shape with good focusing properties. The output power is scalable up to more than 1 W, whereas only a moderate 300 mW is needed for the spectroscopy experiments. After warming up, the NOPO runs very stable at these conditions.

The influence of the internal dispersion in the cavity was investigated in more detail. It affects the NOPO in many ways. On the one hand, the GD determines the distance of the relative change in cavity length and thus the tuning speed. Preferably, it ought to be small. On the other hand, a large amount of GDD is beneficial for narrow-band output spectra. However, too many or too thick glass plates cause losses and affect the stability of the cavity. Here, a good balance had to be found.

## Stimulated Raman Spectroscopy experiments

Stimulated Raman spectroscopy was performed successfully with the configured NOPO. Compared to other spectroscopy setups two major benefits stand out. Firstly, the NOPOs output wavelength can be tuned much faster than with commercially available OPOs, which are currently the leading light sources for SRS. Instead of scanning only single spectral lines, which can be accessed slowly in the range of seconds, the presented setup allows real-time spectroscopy over a wide wavenumber range. More than  $1500\text{ cm}^{-1}$ , between  $2000\text{ cm}^{-1}$  and  $3500\text{ cm}^{-1}$  can be examined in less than 10 ms. Secondly, the spectroscopic setup is very basic and compact. Unlike the other two comparatively fast methods, spectral focusing and multiplex SRS, no dispersive elements are required. On the contrary, the spectroscopic unit consists merely of the most necessary elements: amplitude modulation, focusing, photodiode and lock-in amplifier, which are found in all setups.

In this manner, various experiments were realized. Since water samples cannot be analyzed by conventional IR spectroscopy, their observation is a potential application for SRS. In this work, sugar and isopropyl alcohol solutions in water were studied. The linear relationship between the stimulated Raman signal and the concentration ratio was exploited to observe mixing processes. Thus, with a temporal resolution of 7.7 ms, the addition of a water droplet in isopropanol was followed. Subsequently, the water volume could be estimated correctly. Furthermore, the goal of monitoring microplastics in a water environment was achieved. Using stationary plastic samples, it was shown that individual plastic types are distinguishable, despite the lower spectral resolution of the recorded spectra compared to spontaneous Raman measurements. In addition, moving plastics particles with sizes between  $50\text{ }\mu\text{m}$  and  $160\text{ }\mu\text{m}$  floating in a water cuvette were detected, likewise in real-time. Within a time span of 5 s, four particles were detected. On average they stayed in the detection beams for 150 ms before moving back out of the focal area. To conclude, this work opens the door for continuous monitoring of water flows for microplastics. The constructed NOPO proves to be a suitable and reliable light source for this purpose. Nonetheless, there are more ideas on how to further improve the NOPO with the SRS-spectroscopy setup. Some of them are presented in the Outlook.

## 7 | Outlook

This thesis demonstrates the suitability of the NOPO as light source for stimulated Raman spectroscopy. During its development and the spectroscopic experiments, new ideas emerged. On the one hand, they concern the oscillator itself, but also new fields of application. Some of these ideas have already been realized and are part of current research. For example, a NOPO based on the same technique, which is tunable over the whole visible spectral range [51]. Besides an adaptation of the angles in the nonlinear crystal, this requires a transfer of the pump radiation into the ultraviolet regime. Even a NOPO emitting UV-light is feasible by exploiting nonlinear mixing processes inside the cavity. This spectral range is of special interest for the spectroscopy applications. A Raman excitation with this short wavelength is close to electronic transitions in the molecules, which leads to an enhancement in the stimulated Raman intensities. This technique is known as resonance Raman spectroscopy. Other ideas are still in their infancy and need to be developed further. Some of them are presented here.

### **Development towards broad applicability**

Prior to the NOPO's widespread use beyond the laboratory work, its setup must be reduced in size. Including the home-made thin-disk laser as pump source, it takes about 2 m<sup>2</sup> on the optical table. The pump laser may be replaced by a compact fiber laser. The NOPO itself can be compacted by a more adept cavity folding. Reducing the cavity length is only recommended to a limited extent. With constant pump power, this leads to a reduced pulse peak power, which is fundamental for the nonlinear processes in the NOPO as well as for the coherent Raman spectroscopy.

### **Expansion of the spectral range**

Typical Raman spectra do not only own peaks in the wavenumber range above 2800 cm<sup>-1</sup>, which were exploited in the shown measurements. Between 500 cm<sup>-1</sup> to 1200 cm<sup>-1</sup> exists the so-called fingerprint regime with many smaller peaks originating from the CO- and CC-groups of the molecules [65]. With the demonstrated setup, this region would be addressed at NOPO output wavelength of 910 nm or higher. However, due to simultaneously phase-matched second harmonic generation in the used BBO-crystal,

the oscillator starts to run unstably just from there on. This was already shown in the NOPO characteristics on page 27 by means of the power drop in Figure 3.4 and in the phase-matching curves in Figure 2.5 in the theoretical section on page 16. In this plot the solution to this problem is already visible. By changing from the Poynting vector walk-off to the tangential phase-matching geometry the interfering parasitic processes are avoided. Using the noncollinear angle on the other side of the crystal axis, a broadband tunability from the degeneracy point at 1030 nm down to 780 nm with a plateau-like output power is expected. Though at the cost of a degraded beam profile caused by the larger walk-off. The influences of the temporal and spatial effects on the NOPO radiation are simulated in [26]. The actual impact on the spectroscopy applications remains to be studied in more detail.

## Further spectroscopy applications

The most obvious use of the constructed light source is its integration into a microscope. With a suitable focusing and an adjustment of the laser power, for example biological samples with small structures in the  $\mu\text{m}$ -range can be resolved. When scanning large-area samples, the NOPO can exploit its fast tuning times. However, in biomedical imaging typically only one or two Raman peaks are sampled, for example one for lipids and one for proteins [35]. The time benefit with the NOPO is negligible in this case. Nevertheless, if the identification of a special protein with information over a spectral range as wide as possible is required, the NOPO comes into play again. In addition, the demonstrated setup can still be combined with other technologies to increase the signal strength. Surface-enhanced Raman scattering uses the enhancement of electromagnetic fields close to plasmonic nanoantennas. In this way, the Raman signals are intensified by many orders of magnitudes, so that even single molecules can be detected [89]. This applies also to the coherent Raman spectroscopy methods like SRS and CARS.

In contrast, the demonstrated SRS setup can be extended to larger scales too. The current NOPO design allows already output powers of more than 1 W. By adjusting the beam diameters on the critical optics, especially in the nonlinear crystal, the power can be scaled even further. At this point, the initial idea from the introduction 1 at the very beginning of thesis is taken up again. A high-power NOPO allows monitoring of large volumes or process flows in real-time.

## NOPO for IR-spectroscopy

The concept of the fast tunable parametric oscillator with non-collinear phase-matching can be transferred deeper into the infrared spectral regime. Cadmium silicon phosphide (CSP) is an emerging nonlinear, birefringent crystal used in mid-IR OPOs [90]. Typically, these parametric oscillators are collinear phase-matched and pumped with 1  $\mu\text{m}$ .

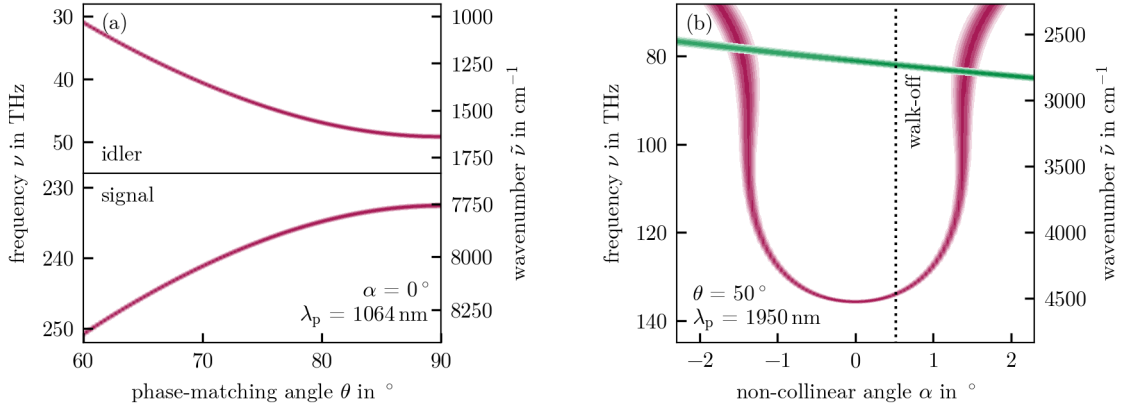


Figure 7.1: (a) Phase-matching curve for a 1.5 mm CSP-crystal which is pumped at 1064 nm and tuned over the crystal angle  $\theta$ . (b) Phase-matching curve for the same crystal, cut at  $\theta = 50^\circ$  and pumped with 1950 nm. At a non-collinear angle of  $1.4^\circ$  broadband PM is found. The green line marks phase-matched parasitic SHG.

The angular tuned signals range from  $1.2 \mu\text{m}$  to  $1.3 \mu\text{m}$ , while the idler reaches the mid-IR around  $6 \mu\text{m}$  to  $7 \mu\text{m}$ . In contrast, pumping at  $2 \mu\text{m}$  is also possible. Thulium or holmium doped fiber lasers with sufficient power and picosecond pulses are already commercially available at this wavelength. For a CSP-crystal, cut at  $\theta = 50^\circ$  broadband, non-collinear phase-matching is found under an angle  $\alpha = 1.4^\circ$ . The phase-matching curve is shown in Figure 7.1. The simulation is based on the Sellmeier coefficients according to [91].

The tunable output reaches from  $2.5 \mu\text{m}$  to  $3.7 \mu\text{m}$ , which corresponds to wavenumbers between  $2700 \text{ cm}^{-1}$  and  $4000 \text{ cm}^{-1}$ . In this spectral region, the excitation lines of OH-, NH- and CH-bondings in molecules are found, which could be directly accessed with such a light source by infrared spectroscopy. The birefringent walk-off angle is rather small at  $0.5^\circ$ , so that even in tangential phase-matching geometry a decent beam profile is to be expected. For the intracavity dispersion management, it is necessary to change to other glass types with a wider transparency range, for example magnesium or calcium fluoride windows. The main challenge will be the development of broadband, highly reflective optics in the infrared spectral regime with a flat GDD-profile.



# Appendix

# A | Optical Parametric Gain

In most literature the calculation of the parametric gain is given only piecewise. Often there are big jumps between the calculation steps. The complete derivation is carried together from several textbooks [15, 16].

To calculate the parametric gain, let's start with the three coupled amplitude equations for the difference-frequency process introduced in Equation (2.6). As explained in Chapter 2.1 the OPA process is a special case of DFG. Here, it is assumed that the pump beam is strong and do not experience any depletion.

$$\frac{\partial A_S}{\partial z} = i\kappa_S A_P A_I^* e^{i\Delta k z} \quad (\text{A.1})$$

$$\frac{\partial A_I}{\partial z} = i\kappa_I A_P A_S^* e^{i\Delta k z} \quad (\text{A.2})$$

$$\frac{\partial A_P}{\partial z} = i\kappa_P A_S A_I^* e^{-i\Delta k z} \quad \xrightarrow{\text{no depletion}} \quad \frac{\partial A_P}{\partial z} = 0 \quad (\text{A.3})$$

To solve the equation, take the second derivation from Equation (A.1):

$$\begin{aligned} \frac{\partial^2 A_S}{\partial z^2} &= i\kappa_S \underbrace{\frac{\partial A_P}{\partial z}}_{=0} A_I^* e^{i\Delta k z} + i\kappa_S A_P \underbrace{\frac{\partial A_I^*}{\partial z}}_{\rightarrow (\text{A.2})} e^{i\Delta k z} + i\Delta k \frac{\partial A_S}{\partial z} \\ &= i\kappa_S A_P \left( -i\kappa_I A_P^* A_S e^{-i\Delta k z} \right) e^{i\Delta k z} + i\Delta k \frac{\partial A_S}{\partial z} \\ &= \underbrace{\kappa_S \kappa_I |A_P|^2}_{=\Gamma^2} A_S + i\Delta k \frac{\partial A_S}{\partial z} \\ \Rightarrow \quad \frac{\partial^2 A_S}{\partial z^2} &= \Gamma^2 A_S + i\Delta k \frac{\partial A_S}{\partial z} \quad \text{by analogy} \quad \frac{\partial A_I}{\partial z} = \Gamma^2 A_I + i\Delta k \frac{\partial A_I}{\partial z} \quad (\text{A.4}) \end{aligned}$$

The solution of the differential equations has the following form:

$$A_S(z) = [\alpha \cosh(gz) + \beta \sinh(gz)] e^{i\Delta k/2z} \quad (\text{A.5})$$

$$A_I(z) = [\gamma \cosh(gz) + \delta \sinh(gz)] e^{i\Delta k/2z} \quad \text{with} \quad g^2 = \Gamma^2 - (\Delta k/2)^2. \quad (\text{A.6})$$

From the starting conditions  $A_S(0) = A_{S0}$  and  $A_I(0) = A_{I0}$ , we already get the first coefficients  $\alpha = A_{S0}$  and  $\gamma = A_{I0}$ .



From this approach we take the derivative and then compare it with the initial wave equation (A.1):

$$\begin{aligned}
\frac{\partial A_S}{\partial z} &= g [A_{S0} \sinh(gz) + \beta \cosh(gz)] e^{i\Delta k/2z} + i \frac{\Delta k}{2} [A_{S0} \cosh(gz) + \beta \sinh(gz)] e^{i\Delta k/2z} \\
&= \left[ \left( g\beta + i \frac{\Delta k}{2} A_{S0} \right) \cosh(gz) + \left( gA_{S0} + i \frac{\Delta k}{2} \beta \right) \sinh(gz) \right] e^{i\Delta k/2z} \\
&\stackrel{!}{=} i\kappa_S A_P A_I^* \\
&= i\kappa_S A_P [A_{I0}^* \cosh(gz) + \delta^* \sinh(gz)] e^{i\Delta k/2z}.
\end{aligned}$$

The same calculation can be repeated with the idler envelope  $A_I(z)$  and the Equations (A.2) and (A.6). A subsequent coefficient comparison leads to the two still unknown variables  $\beta$  and  $\delta$ .

$$\begin{aligned}
g\beta + i \frac{\Delta k}{2} A_{S0} &= i\kappa_S A_P A_{I0}^* & \text{and} & & g\delta + i \frac{\Delta k}{2} A_{I0} &= i\kappa_I A_P A_{S0}^* \\
\Rightarrow \beta &= i \frac{\kappa_S}{g} A_P A_{I0}^* - i \frac{\Delta k/2}{g} A_{S0} & \text{and} & & \delta &= i \frac{\kappa_I}{g} A_P A_{S0}^* - i \frac{\Delta k/2}{g} A_{I0}
\end{aligned}$$

Both solutions, for the signal and idler waves are symmetrical. However, in general the idler is non-resonant in an OPO or not seeded in an OPA. This changes the starting conditions to  $A_{I0} = 0$  and the solution for the signal beam is

$$A_S(z) = A_{S0} \left[ \cosh(gz) - i \frac{\Delta k/2}{g} \sinh(gz) \right] e^{i\Delta k/2z} \quad \text{with} \quad g^2 = \Gamma^2 - (\Delta k/2)^2. \quad (\text{A.7})$$

The intensity of the signal beam is calculated over  $I = \frac{1}{2} c \varepsilon_0 |A_S|^2$ . It is proportional to

$$\begin{aligned}
\frac{|A_S(z)|^2}{|A_{S0}|^2} &= \frac{1}{|A_{S0}|^2} A_S(z) A_S^*(z) && \leftarrow (a + ib)(a - ib) = a^2 + b^2 \\
&= \cosh^2(gz) + \frac{(\Delta k/2)^2}{g^2} \sinh^2(gz) && \leftarrow \cosh^2 x = \sinh^2 x + 1 \\
&= 1 + \left( 1 + \frac{(\Delta k/2)^2}{g^2} \right) \sinh^2(gz) && \leftarrow g^2 = \Gamma^2 - (\Delta k/2)^2 \\
&= 1 + \frac{\Gamma^2}{g^2} \sinh^2(gz). && (\text{A.8})
\end{aligned}$$

The net gain  $G(l)$  after a crystal of length  $z = l$  is defined over

$$G(l) = \frac{I(z=l)}{I(0)} - 1 = \frac{\Gamma^2}{g^2} \sinh^2(gl), \quad (\text{A.9})$$

which is the final expression from Equation (2.7) shown in Chapter 2.1.2.

## B | SRS from the wave equation

Like the parametric gain (2.7) for the explanation of the OPO in Chapter 2.1.2, the stimulated Raman gain is derived in more detail at this point. And again, we start with the propagation equations from Equation (4.17) and insert the corresponding nonlinear polarizations for the coherent Raman processes from the Equations (4.13c) and (4.13d).

$$\begin{aligned}\frac{\partial A_S}{\partial z} &= \frac{i\omega_S}{2n_S c \varepsilon_0} P(\omega_S) & \frac{\partial A_P}{\partial z} &= \frac{i\omega_P}{2n_P c \varepsilon_0} P(\omega_P) \\ &= 3 \frac{i\omega_S}{n_S c} \chi_{NL}^* |A_P|^2 A_S & &= 3 \frac{i\omega_P}{n_P c} \chi_{NL} |A_S|^2 A_P\end{aligned}\quad (\text{B.1})$$

Firsts, let's consider the intensity  $I = \frac{1}{2} n c \varepsilon_0 |A|^2$  of the Stokes and pump beam. They change when passing through the Raman active medium with

$$\begin{aligned}\frac{dI_S}{dz} &= \frac{n_S c \varepsilon_0}{2} \frac{d}{dz} |A_S|^2 = \frac{n_S c \varepsilon_0}{2} \left[ \underbrace{\frac{\partial A_S}{\partial z}}_{\rightarrow (\text{B.1})} A_S^* + A_S \underbrace{\frac{\partial A_S^*}{\partial z}}_{\rightarrow (\text{B.1})} \right] \\ &= \frac{n_S c \varepsilon_0}{2} \left[ 3 \frac{i\omega_S}{n_S c} \chi_{NL}^* |A_P|^2 |A_S|^2 + 3 \frac{-i\omega_S}{n_S c} \chi_{NL} |A_P|^2 |A_S|^2 \right] \\ &= \frac{n_S c \varepsilon_0}{2} \cdot 3 \frac{i\omega_S}{n_S c} |A_P|^2 |A_S|^2 \cdot [\chi_{NL}^* - \chi_{NL}]\end{aligned}\quad (\text{B.2})$$

$$\frac{dI_P}{dz} = \frac{n_P c \varepsilon_0}{2} \cdot 3 \frac{i\omega_P}{n_P c} |A_P|^2 |A_S|^2 \cdot [\chi_{NL} - \chi_{NL}^*]. \quad (\text{B.3})$$

The difference of the nonlinear susceptibilities can be simplified over

$$\chi_{NL} - \chi_{NL}^* = (\text{Re}\{\chi_{NL}\} + i \text{Im}\{\chi_{NL}\}) - (\text{Re}\{\chi_{NL}\} - i \text{Im}\{\chi_{NL}\}) = 2i \text{Im}\{\chi_{NL}\}.$$

The absolute squares of the amplitudes are replaced by the corresponding intensities  $|A|^2 = \frac{2I}{nc\varepsilon_0}$ . Thus, the differential equations read as

$$\begin{aligned}\frac{dI_S}{dz} &= \frac{12\omega_S}{n_S n_P c^2 \varepsilon_0} \text{Im}\{\chi_{NL}\} I_P I_S & \frac{dI_P}{dz} &= -\frac{12\omega_P}{n_S n_P c^2 \varepsilon_0} \text{Im}\{\chi_{NL}\} I_P I_S \\ &= g_R I_P I_S & &= -\frac{\omega_P}{\omega_S} g_R I_P I_S,\end{aligned}\quad (\text{B.4})$$

with the Raman gain coefficient  $g_{\text{R}} = \frac{12\omega_{\text{S}}}{n_{\text{S}}n_{\text{P}}c^2\varepsilon_0} \text{Im}\{\chi_{\text{NL}}\}$ .

Assuming that the incoming Stokes and pump beams do not experience any intensity change when they generate the weak stimulated Raman gain and loss fields [57], the solution of the propagation equations are

$$I_{\text{S}}(z) = I_{\text{S}}(0) \exp(g_{\text{R}}I_{\text{P}}(0)z) \quad \text{and} \quad I_{\text{P}}(z) = I_{\text{P}}(0) \exp(g_{\text{R}}I_{\text{S}}(0)z). \quad (\text{B.5})$$

## C | Principle of Lock-In Amplifiers

All the presented spectroscopy measurements base on the stimulated Raman loss, which is detected as a very small intensity change on the NOPO radiation. Specifically, in the microplastics experiments shown in Section 5.3.3, the NOPO radiation generates a voltage around 300 mV on a photodiode, varying slightly with wavelength. However, the strong Raman intensity generated by the water environment causes a voltage change of 150  $\mu$ V. This is a factor 2000 less. The signal from the microplastics is another order of magnitude lower. Such tiny changes cannot be measured directly. Lock-In amplifier provide a remedy. Their operating principle is briefly illustrated here. Further information can be found in the manufacturer's manuals [92, 93].

Lock-in amplifiers require periodic input signals, which are compared to a reference. Both of them can be expressed by sinusoidal functions, whereby the input signal has an unknown amplitude  $V_0$  and phase  $\theta$ , plus a strong background  $V_{BG}$  in some cases.

$$V_{\text{ref}}(t) = \sin[\omega_{\text{ref}}t] \quad V_{\text{sig}}(t) = V_0 \sin[\omega_{\text{sig}}t + \theta] + V_{BG}. \quad (\text{C.1})$$

The signal to be measured and the reference voltage are mixed electronically. Mathematically, this corresponds to a multiplication, which contains their sum and difference frequencies

$$\begin{aligned} V_{\text{mix}}(t) &= V_{\text{ref}}(t) \times V_{\text{sig}}(t) & (\text{C.2}) \\ &= \frac{1}{2}V_0 \cos[(\omega_{\text{ref}} - \omega_{\text{sig}})t - \theta] - \frac{1}{2}V_0 \cos[\underbrace{(\omega_{\text{ref}} + \omega_{\text{sig}})t + \theta}_{\text{fast}}] + V_{BG} \sin[\underbrace{\omega_{\text{ref}}t}_{\text{fast}}]. \end{aligned}$$

Subsequently, the processed signal passes a low-pass filter, which removes all fast oscillations. In mathematical terms, the signal is averaged over time. In the general case, all terms disappear. However, if the reference frequency coincides with the signal frequency  $\omega_{\text{ref}} = \omega_{\text{sig}}$ , a constant dc-term  $V_X = \frac{1}{2}V_0 \cos \theta$  remains. Copying the input signal and repeating the operations with a reference shifted by  $\pi/2$  yields the second quadrature component  $V_Y = \frac{1}{2}V_0 \sin \theta$ . Both together result in the searched signal amplitude  $V_0$  and phase  $\theta$ . For illustration, the process is sketched in Figure C.1(a). Next to it are two examples.

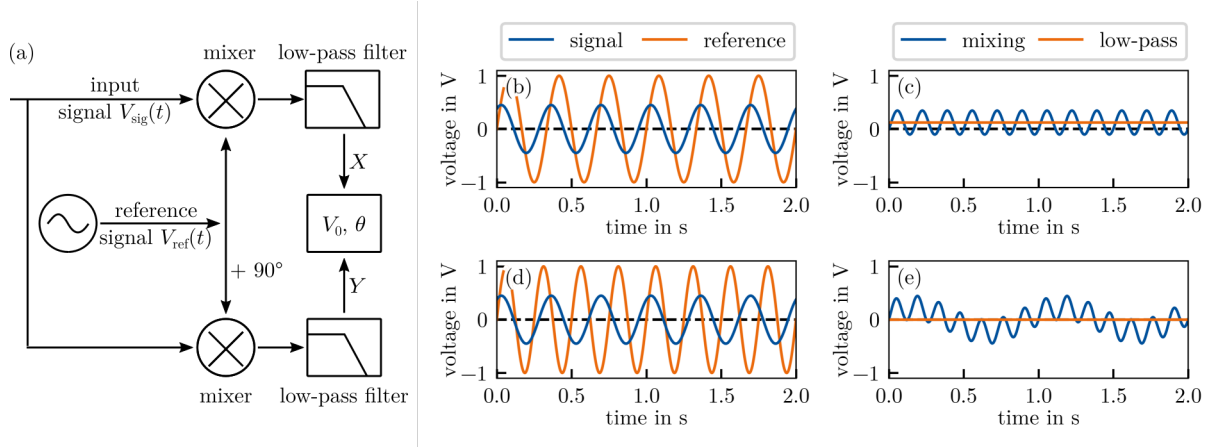


Figure C.1: (a) Sketch of the lock-in measurement. (b) Exemplary input signal with  $f_{\text{sig}} = 3 \text{ Hz}$  and identical reference frequency. (c) Resulting signal after the mixer (blue) and the low-pass filter (orange). (d) Same input signal with mismatched reference  $f_{\text{ref}} = 4 \text{ Hz}$ . (e) The corresponding outputs average to zero.

Figure C.1(b) shows a signal and reference wave with the same frequency of 3 Hz. On the other hand in (c), the mixed signal is plotted in blue. Averaged over time, a constant value remains, which corresponds to the  $V_X$ -quadrature from the above calculation. In the graphs below, the reference frequency does not match that of the signal. The mixed signal shows beatings and averages to zero. The input signal cannot be extracted.

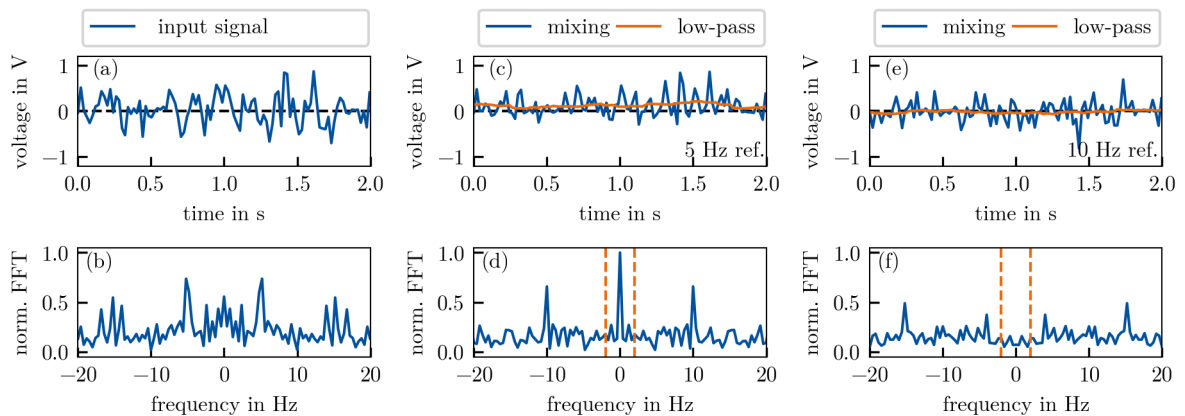


Figure C.2: Left: Noisy input signal with 5 Hz carrier frequency in (a) time and (b) frequency domain. Middle: Same signal after mixing with a matched 5 Hz reference (blue). (c) After the subsequent filtering with a 500 ms time constant a not vanishing output emerges (orange). (d) In the frequency domain, a distinct dc-signal is apparent inside the the 2 Hz filter bandwidth. Right: Mixed signal with an unfitting 10 Hz reference (blue). (e) The lock-in output averages to zero (orange). (f) No signal apparent.

A second example is given in Figure C.2, where a noisy input signal with a 5 Hz carrier frequency is extracted by a lock-in amplifier. The mixed and low-pass filtered signals are shown in blue and orange as in the previous Figure C.1(c) and (e). Additionally, the improvement of the signal-to-noise ratio in the frequency domain is illustrated. In contrast, no signal is detected if the reference frequency is incorrectly chosen.







# Bibliography

- [1] R. Kakkar, “Fundamentals of Spectroscopy,” in *Atomic and Molecular Spectroscopy: Basic Concepts and Applications*, pp. 1–50, Cambridge: Cambridge University Press, 2015.
- [2] J. James, “A brief history of spectroscopy,” in *Spectrograph Design Fundamentals*, pp. 1–5, Cambridge: Cambridge University Press, 2007.
- [3] P. Larkin, “Introduction: Infrared and Raman Spectroscopy,” in *Infrared and Raman Spectroscopy*, pp. 1–5, Elsevier, 2011.
- [4] G. W. Auner, S. K. Koya, C. Huang, B. Broadbent, M. Trexler, Z. Auner, A. Elias, K. C. Mehne, and M. A. Brusatori, “Applications of Raman spectroscopy in cancer diagnosis,” *Cancer and Metastasis Reviews*, vol. 37, pp. 691–717, Dec. 2018.
- [5] T. Vankeirsbilck, A. Vercauteren, W. Baeyens, G. Van der Weken, F. Verpoort, G. Vergote, and J. Remon, “Applications of Raman spectroscopy in pharmaceutical analysis,” *TrAC Trends in Analytical Chemistry*, vol. 21, pp. 869–877, Dec. 2002.
- [6] D. Yang and Y. Ying, “Applications of Raman Spectroscopy in Agricultural Products and Food Analysis: A Review,” *Applied Spectroscopy Reviews*, vol. 46, pp. 539–560, Oct. 2011.
- [7] M. Fries and A. Steele, “Raman Spectroscopy and Confocal Raman Imaging in Mineralogy and Petrography,” in *Confocal Raman Microscopy* (J. Toporski, T. Dieing, and O. Hollricher, eds.), vol. 66, pp. 209–236, Cham: Springer International Publishing, 2018.
- [8] W. Wang, H. Zhang, Y. Yuan, Y. Guo, and S. He, “Research Progress of Raman Spectroscopy in Drug Analysis,” *AAPS PharmSciTech*, vol. 19, pp. 2921–2928, Oct. 2018.
- [9] F. Shahul Hamid, M. S. Bhatti, N. Anuar, N. Anuar, P. Mohan, and A. Periyathamby, “Worldwide distribution and abundance of microplastic: How dire is the situation?,” *Waste Management & Research*, vol. 36, pp. 873–897, Oct. 2018.

- [10] A. A. Koelmans, N. H. Mohamed Nor, E. Hermsen, M. Kooi, S. M. Mintenig, and J. De France, “Microplastics in freshwaters and drinking water: Critical review and assessment of data quality,” *Water Research*, vol. 155, pp. 410–422, May 2019.
- [11] J. Li, H. Liu, and J. Paul Chen, “Microplastics in freshwater systems: A review on occurrence, environmental effects, and methods for microplastics detection,” *Water Research*, vol. 137, pp. 362–374, June 2018.
- [12] C. Araújo, M. Nolasco, A. Ribeiro, and P. Ribeiro Claro, “Identification of microplastics using Raman spectroscopy: Latest developments and future prospects,” *Water Research*, vol. 142, June 2018.
- [13] P. A. Franken, A. E. Hill, C. W. Peters, and G. Weinreich, “Generation of Optical Harmonics,” *Physical Review Letters*, vol. 7, pp. 118–119, Aug. 1961.
- [14] P. Franken, “Interview of Peter Franken by Joan Bromberg,” Mar. 1958.
- [15] R. W. Boyd, *Nonlinear Optics*. Amsterdam ; Boston: Academic Press, 3rd ed., 2008.
- [16] P. E. Powers and J. W. Haus, *Fundamentals of Nonlinear Optics*. Taylor & Francis Group, 2017.
- [17] D. Meschede, “Nichtlineare Optik I: Optische Mischprozesse,” in *Optik, Licht und Laser*, Studium, pp. 493–523, Wiesbaden: Vieweg + Teubner, 3rd ed., 2008.
- [18] C. Manzoni and G. Cerullo, “Design criteria for ultrafast optical parametric amplifiers,” *Journal of Optics*, vol. 18, p. 103501, Aug. 2016.
- [19] M. Ebrahimzadeh, “Mid-Infrared Ultrafast and Continuous- Wave Optical Parametric Oscillators,” in *Solid-State Mid-Infrared Laser Sources*, Topics in Applied Physics, pp. 184–224, Berlin, Heidelberg: Springer, 2003.
- [20] J. Q. Zhao, B. Q. Yao, Y. Tian, Y. L. Ju, and Y. Z. Wang, “High power, continuous wave, singly resonant OPO based on MgO:PPLN,” *Laser Physics*, vol. 20, pp. 1902–1906, Oct. 2010.
- [21] F. J. Furch, T. Witting, A. Giree, C. Luan, F. Schell, G. Arisholm, C. P. Schulz, and M. J. J. Vrakking, “CEP-stable few-cycle pulses with more than 190  $\mu\text{J}$  of energy at 100 kHz from a noncollinear optical parametric amplifier,” *Optics Letters*, vol. 42, pp. 2495–2498, July 2017.
- [22] G. Cerullo and S. De Silvestri, “Ultrafast optical parametric amplifiers,” *Review of Scientific Instruments*, vol. 74, pp. 1–18, Jan. 2003.

- [23] V. G. Dmitriev, G. G. Gurzadjan, and D. N. Nikogosjan, *Handbook of Nonlinear Optical Crystals*. No. 64 in Springer Series in Optical Sciences, Berlin: Springer, 3rd ed., 2010.
- [24] D. S. Hum and M. M. Fejer, “Quasi-phasematching,” *Comptes Rendus Physique*, vol. 8, pp. 180–198, Mar. 2007.
- [25] T. Lang, *Ultrashort Laser Pulses from Optical Parametric Amplifiers and Oscillators*. PhD thesis, Gottfried Wilhelm Leibniz Universität Hannover, Hannover, July 2014.
- [26] T. Lang, A. Harth, J. Matyschok, T. Binhammer, M. Schultze, and U. Morgner, “Impact of temporal, spatial and cascaded effects on the pulse formation in ultra-broadband parametric amplifiers,” *Optics Express*, vol. 21, pp. 949–959, Jan. 2013.
- [27] F. X. Kärtner, U. Morgner, R. Ell, T. Schibli, J. G. Fujimoto, E. P. Ippen, V. Scheuer, G. Angelow, and T. Tschudi, “Ultrabroadband double-chirped mirror pairs for generation of octave spectra,” *JOSA B*, vol. 18, pp. 882–885, June 2001.
- [28] T. Lang, T. Binhammer, S. Rausch, G. Palmer, M. Emons, M. Schultze, A. Harth, and U. Morgner, “High power ultra-widely tuneable femtosecond pulses from a non-collinear optical parametric oscillator (NOPO),” *Optics Express*, vol. 20, pp. 912–917, Jan. 2012.
- [29] P. G. Schunemann, “New Nonlinear Crystals for the Mid-Infrared,” in *Nonlinear Optics (2017)*, Paper NTu2A.1, p. NTu2A.1, Optical Society of America, July 2017.
- [30] J. A. Giordmaine and R. C. Miller, “Tunable Coherent Parametric Oscillation in  $\text{LiNbO}_3$  at Optical Frequencies,” *Physical Review Letters*, vol. 14, pp. 973–976, June 1965.
- [31] C. V. Shank, “Physics of dye lasers,” *Reviews of Modern Physics*, vol. 47, pp. 649–657, July 1975.
- [32] G. Huber, C. Kränkel, and K. Petermann, “Solid-state lasers: Status and future [Invited],” *JOSA B*, vol. 27, pp. B93–B105, Nov. 2010.
- [33] M. H. Dunn and M. Ebrahimzadeh, “Parametric Generation of Tunable Light from Continuous-Wave to Femtosecond Pulses,” *Science*, vol. 286, pp. 1513–1517, Nov. 1999.
- [34] D. E. Spence, P. N. Kean, and W. Sibbett, “60-fsec pulse generation from a self-mode-locked Ti:sapphire laser,” *Optics Letters*, vol. 16, pp. 42–44, Jan. 1991.

- [35] M. Brinkmann, M. Brinkmann, M. Brinkmann, A. Fast, A. Fast, T. Hellwig, T. Hellwig, I. Pence, C. L. Evans, C. Fallnich, and C. Fallnich, “Portable all-fiber dual-output widely tunable light source for coherent Raman imaging,” *Biomedical Optics Express*, vol. 10, pp. 4437–4449, Sept. 2019.
- [36] U. Demirbas and A. Sennaroglu, “Intracavity-pumped  $\text{Cr}^{2+}:\text{ZnSe}$  laser with ultra-broad tuning range between 1880 and 3100 nm,” *Optics Letters*, vol. 31, pp. 2293–2295, Aug. 2006.
- [37] A. V. Shestakov, N. I. Borodin, V. A. Zhitnyuk, A. G. Ohrimtchyuk, and V. P. Gapontsev, “Tunable  $\text{Cr}^{4+}:\text{YAG}$  Lasers,” in *Conference on Lasers and Electro-Optics (1991), Paper CPD11*, p. CPD11, Optical Society of America, May 1991.
- [38] V. G. Baryshevskii, M. V. Korzhik, A. E. Kimaev, M. G. Livshits, V. B. Pavlenko, M. L. Meil’man, and B. I. Minkov, “Tunable chromium forsterite laser in the near IR region,” *Journal of Applied Spectroscopy*, vol. 53, pp. 675–676, July 1990.
- [39] M. Stalder, B. H. T. Chai, and M. Bass, “Flashlamp pumped  $\text{Cr}:\text{LiSrAlF}_6$  laser,” *Applied Physics Letters*, vol. 58, pp. 216–218, Jan. 1991.
- [40] J. Walling, D. Heller, H. Samelson, D. Harter, J. Pete, and R. Morris, “Tunable alexandrite lasers: Development and performance,” *IEEE Journal of Quantum Electronics*, vol. 21, pp. 1568–1581, Oct. 1985.
- [41] G. Rines, H. Zenzie, R. Schwarz, Y. Isyanova, and P. Moulton, “Nonlinear conversion of Ti:sapphire laser wavelengths,” *IEEE Journal of Selected Topics in Quantum Electronics*, vol. 1, pp. 50–57, Apr. 1995.
- [42] C. D. Decker and F. K. Tittel, “Broadly tunable, narrow linewidth dye laser emission in the near infrared,” *Optics Communications*, vol. 7, pp. 155–157, Feb. 1973.
- [43] E. D. Stokes, F. B. Dunning, R. F. Stebbings, G. K. Walters, and R. D. Rundel, “A high efficiency dye laser tunable from the UV to the IR,” *Optics Communications*, vol. 5, pp. 267–270, July 1972.
- [44] J. Sperling, N. Waasem, R. Gärtner, M. Schubert, G. Elgcrona, and K. Hens, “Advances in the spectral coverage of tunable continuous-wave optical parametric oscillators,” in *Nonlinear Frequency Generation and Conversion: Materials and Devices XX*, vol. 11670, pp. 162–168, SPIE, Mar. 2021.

- [45] S. French, M. Ebrahimzadeh, and A. Miller, “Intracavity-frequency-doubled picosecond optical parametric oscillator based on noncritically phase-matched  $\text{LiB}_3\text{O}_5$ ,” in *Summaries of Papers Presented at the Conference on Lasers and Electro-Optics*, pp. 342–343, June 1996.
- [46] M. Ghotbi, A. Esteban-Martin, and M. Ebrahim-Zadeh, “Tunable, high-repetition-rate, femtosecond pulse generation in the ultraviolet,” *Optics Letters*, vol. 33, pp. 345–347, Feb. 2008.
- [47] W. R. Bosenberg and D. R. Guyer, “Broadly tunable, single-frequency optical parametric frequency-conversion system,” *JOSA B*, vol. 10, pp. 1716–1722, Sept. 1993.
- [48] Y. X. Fan, R. C. Eckardt, R. L. Byer, J. Nolting, and R. Wallenstein, “Visible  $\text{BaB}_2\text{O}_4$  optical parametric oscillator pumped at 355 nm by a single-axial-mode pulsed source,” *Applied Physics Letters*, vol. 53, pp. 2014–2016, Nov. 1988.
- [49] L. Kong, M. Ji, G. R. Holtom, D. Fu, C. W. Freudiger, and X. S. Xie, “Multicolor stimulated Raman scattering microscopy with a rapidly tunable optical parametric oscillator,” *Optics Letters*, vol. 38, pp. 145–147, Jan. 2013.
- [50] J. R. C. Andrade, N. Modsching, A. Tajalli, C. M. Dietrich, S. Kleinert, F. Placzek, B. Kreipe, S. Schilt, V. J. Wittwer, T. Südmeyer, and U. Morgner, “Carrier-Envelope Offset Frequency Stabilization of a Thin-Disk Laser Oscillator via Depletion Modulation,” *IEEE Photonics Journal*, vol. 12, pp. 1–9, Apr. 2020.
- [51] R. Mevert, R. Mevert, Y. Binhammer, Y. Binhammer, C. M. Dietrich, C. M. Dietrich, L. Beichert, L. Beichert, J. R. C. de Andrade, J. R. C. de Andrade, T. Binhammer, J. Fan, J. Fan, U. Morgner, and U. Morgner, “Widely tunable, high-power, femtosecond noncollinear optical parametric oscillator in the visible spectral range,” *Photonics Research*, vol. 9, pp. 1715–1718, Sept. 2021.
- [52] C. V. Raman, “A new radiation,” *Indian Journal of physics*, vol. 2, pp. 387–398, 1928.
- [53] C. L. Braun and S. N. Smirnov, “Why is water blue?,” *Journal of Chemical Education*, vol. 70, p. 612, Aug. 1993.
- [54] C. V. Raman, “Physics 1930,” in *Physics 1922–1941*, pp. 261–277, Elsevier, 1st ed., 1965.
- [55] R. C. Prince, R. R. Frontiera, and E. O. Potma, “Stimulated Raman Scattering: From Bulk to Nano,” *Chemical Reviews*, vol. 117, pp. 5070–5094, Apr. 2017.

- [56] J.-X. Cheng and X. S. Xie, eds., *Coherent Raman Scattering Microscopy*. Series in Cellular and Clinical Imaging, CRC Press, Taylor & Francis Group, 2013.
- [57] H. Rigneault and P. Berto, “Tutorial: Coherent Raman light matter interaction processes,” *APL Photonics*, vol. 3, p. 091101, July 2018.
- [58] B. E. A. Saleh and M. C. Teich, “Electromagnetic Optics,” in *Fundamentals of Photonics*, pp. 157–192, John Wiley & Sons, Inc., 2001.
- [59] G. P. Agrawal, “Stimulated Raman Scattering,” in *Nonlinear Fiber Optics*, pp. 295–352, Amsterdam: Elsevier/Academic Press, 5th ed., 2013.
- [60] Y. Ozeki, T. Asai, J. Shou, and H. Yoshimi, “Multicolor Stimulated Raman Scattering Microscopy With Fast Wavelength-Tunable Yb Fiber Laser,” *IEEE Journal of Selected Topics in Quantum Electronics*, vol. 25, pp. 1–11, Jan. 2019.
- [61] J.-X. Cheng, M. Wei, Y. Ozeki, and D. Polli, eds., *Stimulated Raman Scattering Microscopy: Techniques and Applications*. Amsterdam: Elsevier, 2021.
- [62] C. Zhang, K.-C. Huang, B. Rajwa, J. Li, S. Yang, H. Lin, C.-s. Liao, G. Eakins, S. Kuang, V. Patsekina, J. P. Robinson, and J.-X. Cheng, “Stimulated Raman scattering flow cytometry for label-free single-particle analysis,” *Optica*, vol. 4, p. 103, Jan. 2017.
- [63] M. S. Alshaykh, C.-S. Liao, O. E. Sandoval, G. Gitzinger, N. Forget, D. E. Leaird, J.-X. Cheng, and A. M. Weiner, “High-speed stimulated hyperspectral Raman imaging using rapid acousto-optic delay lines,” *Optics Letters*, vol. 42, pp. 1548–1551, Apr. 2017.
- [64] AIST: Spectral Database for Organic Compounds, SDBS, “SDBS No.: 4544, water, InChI=1S/H2O/h1H2,” *National Institute of Advanced Industrial Science and Technology (AIST)*, Mar. 1999.
- [65] D. Lin-Vien, ed., *The Handbook of Infrared and Raman Characteristic Frequencies of Organic Molecules*. Boston: Academic Press, 1991.
- [66] E. Wiercigroch, E. Szafraniec, K. Czamara, M. Z. Pacia, K. Majzner, K. Kochan, A. Kaczor, M. Baranska, and K. Malek, “Raman and infrared spectroscopy of carbohydrates: A review,” *Spectrochimica Acta Part A: Molecular and Biomolecular Spectroscopy*, vol. 185, pp. 317–335, Oct. 2017.
- [67] AIST: Spectral Database for Organic Compounds, SDBS, “SDBS No.: 2149,2-propanol, InChI=1S/C3H8O/c1-3(2)4/h3-4H,1-2H3,” *National Institute of Advanced Industrial Science and Technology (AIST)*, Mar. 1999.

- [68] M. Bergmann, S. Mützel, S. Primpke, M. B. Tekman, J. Trachsel, and G. Gerdts, “White and wonderful? Microplastics prevail in snow from the Alps to the Arctic,” *Science Advances*, vol. 5, p. eaax1157, Aug. 2019.
- [69] S. Reed, M. Clark, R. Thompson, and K. A. Hughes, “Microplastics in marine sediments near Rothera Research Station, Antarctica,” *Marine Pollution Bulletin*, vol. 133, pp. 460–463, Aug. 2018.
- [70] C. Jiang, L. Yin, Z. Li, X. Wen, X. Luo, S. Hu, H. Yang, Y. Long, B. Deng, L. Huang, and Y. Liu, “Microplastic pollution in the rivers of the Tibet Plateau,” *Environmental Pollution*, vol. 249, pp. 91–98, June 2019.
- [71] L. Van Cauwenberghe, A. Vanreusel, J. Mees, and C. R. Janssen, “Microplastic pollution in deep-sea sediments,” *Environmental Pollution*, vol. 182, pp. 495–499, Nov. 2013.
- [72] C. Li, R. Busquets, and L. C. Campos, “Assessment of microplastics in freshwater systems: A review,” *Science of The Total Environment*, vol. 707, p. 135578, Mar. 2020.
- [73] F. De Falco, E. Di Pace, M. Cocca, and M. Avella, “The contribution of washing processes of synthetic clothes to microplastic pollution,” *Scientific Reports*, vol. 9, p. 6633, Apr. 2019.
- [74] P. J. Kole, A. J. Löhr, F. G. A. J. Van Belleghem, and A. M. J. Ragas, “Wear and Tear of Tyres: A Stealthy Source of Microplastics in the Environment,” *International Journal of Environmental Research and Public Health*, vol. 14, p. 1265, Oct. 2017.
- [75] K. Senathirajah, S. Attwood, G. Bhagwat, M. Carbery, S. Wilson, and T. Palanisami, “Estimation of the mass of microplastics ingested – A pivotal first step towards human health risk assessment,” *Journal of Hazardous Materials*, vol. 404, p. 124004, Feb. 2021.
- [76] N. H. Mohamed Nor, M. Kooi, N. J. Diepens, and A. A. Koelmans, “Lifetime Accumulation of Microplastic in Children and Adults,” *Environmental Science & Technology*, vol. 55, pp. 5084–5096, Apr. 2021.
- [77] J. C. Prata, J. P. da Costa, A. C. Duarte, and T. Rocha-Santos, “Methods for sampling and detection of microplastics in water and sediment: A critical review,” *TrAC Trends in Analytical Chemistry*, vol. 110, pp. 150–159, Jan. 2019.

- [78] J.-L. Xu, K. V. Thomas, Z. Luo, and A. A. Gowen, “FTIR and Raman imaging for microplastics analysis: State of the art, challenges and prospects,” *TrAC Trends in Analytical Chemistry*, vol. 119, p. 115629, Oct. 2019.
- [79] A. M. Elert, R. Becker, E. Duemichen, P. Eisentraut, J. Falkenhagen, H. Sturm, and U. Braun, “Comparison of different methods for MP detection: What can we learn from them, and why asking the right question before measurements matters?,” *Environmental Pollution*, vol. 231, pp. 1256–1264, Dec. 2017.
- [80] W. J. Shim, Y. K. Song, S. H. Hong, and M. Jang, “Identification and quantification of microplastics using Nile Red staining,” *Marine Pollution Bulletin*, vol. 113, pp. 469–476, Dec. 2016.
- [81] D. Fabbri, “Use of pyrolysis-gas chromatography/mass spectrometry to study environmental pollution caused by synthetic polymers: A case study: The Ravenna Lagoon,” *Journal of Analytical and Applied Pyrolysis*, vol. 58–59, pp. 361–370, Apr. 2001.
- [82] I. Hintersteiner, M. Himmelsbach, and W. W. Buchberger, “Characterization and quantitation of polyolefin microplastics in personal-care products using high-temperature gel-permeation chromatography,” *Analytical and Bioanalytical Chemistry*, vol. 407, pp. 1253–1259, Feb. 2015.
- [83] O. Faix, “Fourier Transform Infrared Spectroscopy,” in *Methods in Lignin Chemistry* (S. Y. Lin and C. W. Dence, eds.), Springer Series in Wood Science, pp. 83–109, Berlin, Heidelberg: Springer, 1992.
- [84] S. P. Laptенок, C. Martin, L. Genchi, C. M. Duarte, and C. Liberale, “Stimulated Raman microspectroscopy as a new method to classify microfibers from environmental samples,” *Environmental Pollution*, vol. 267, p. 115640, Dec. 2020.
- [85] I. S. John Wiley & Sons, “SpectraBase Compound ID=jr9HzIYUWf SpectraBase Spectrum ID=5yfKePC44GN,” <https://spectrabase.com/spectrum/5yfKePC44GN>, Feb. 2022.
- [86] I. S. John Wiley & Sons, “SpectraBase Compound ID=KNro1f1BHjK SpectraBase Spectrum ID=8RALVRcKfwX,” <https://spectrabase.com/spectrum/8RALVRcKfwX>, Feb. 2022.
- [87] I. S. John Wiley & Sons, “SpectraBase Compound ID=KbyJaTWoQq6 SpectraBase Spectrum ID=8ebotcq2f5O,” <https://spectrabase.com/spectrum/8ebotcq2f5O>, Feb. 2022.



- [88] A.-K. Kniggendorf, C. Wetzel, and B. Roth, “Microplastics Detection in Streaming Tap Water with Raman Spectroscopy,” *Sensors*, vol. 19, p. 1839, Jan. 2019.
- [89] S. Nie and S. R. Emory, “Probing Single Molecules and Single Nanoparticles by Surface-Enhanced Raman Scattering,” *Science*, Feb. 1997.
- [90] S. C. Kumar, P. G. Schunemann, K. T. Zawilski, and M. Ebrahim-Zadeh, “Advances in ultrafast optical parametric sources for the mid-infrared based on CdSiP<sub>2</sub>,” *JOSA B*, vol. 33, pp. D44–D56, Nov. 2016.
- [91] V. Kemlin, B. Boulanger, V. Petrov, P. Segonds, B. Ménaert, P. G. Schunemann, and K. T. Zawilski, “Nonlinear, dispersive, and phase-matching properties of the new chalcopyrite CdSiP<sub>2</sub> [Invited],” *Optical Materials Express*, vol. 1, pp. 1292–1300, Nov. 2011.
- [92] Z. Instruments, “White Paper - Principles of lock-in detection and the state of the art.” [www.zhinst.com](http://www.zhinst.com), Nov. 2016.
- [93] S. R. Systems, “SRS Tech Note - Lock-In Amplifier Basics.” [www.thinkSRS.com](http://www.thinkSRS.com), July 2020.

# List of Publications

## Journal publications

1. **L. Beichert**, Y. Binhammer, J. R. C. Andrade, R. Mevert, A.-K. Kniggendorf, B. Roth, and U. Morgner "Real-time stimulated Raman spectroscopy with a non-collinear optical parametric oscillator" *Optics Express*, (2021)
2. R. Mevert, Y. Binhammer, C. M. Dietrich, **L. Beichert**, J. R. C. Andrade, T. Binhammer, J. Fan, and U. Morgner "Widely tunable, high-power, femtosecond noncollinear optical parametric oscillator in the visible spectral range" *Photonics Research*, (2021)

## Talks at international conferences

1. R. Mevert, Y. Binhammer, C. M. Dietrich, J. R. C. Andrade, **L. Beichert**, T. Binhammer, J. Fan, and U. Morgner "Visible, femtosecond, high power, ultra-broadband noncollinear optical parametric oscillator (VIS-NOPO)" in 10th EPS-QEOD Europhoton Conference (2022), FRI-SSL-6.4
2. **L. Beichert**, Y. Binhammer, J. R. C. Andrade, and U. Morgner "Non-collinear Optical Parametric Oscillator as fast tunable light source for Stimulated Raman Scattering" in Conference on Lasers and Electro-Optics (2021), STu4C.5
3. R. Mevert, Y. Binhammer, C. M. Dietrich, J. R. C. Andrade, **L. Beichert**, T. Binhammer, J. Fan, and U. Morgner "Ultra-broadband, high power, femtosecond non-collinear optical parametric oscillator in the visible" in 2021 Conference on Lasers and Electro-Optics Europe & European Quantum Electronics Conference (2021), CF-1.2
4. **L. Beichert**, Y. Binhammer, J. R. C. Andrade, and U. Morgner, "Non-collinear Optical Parametric Oscillator as fast tuneable light source for Stimulated Raman Scattering" in 9th EPS-QEOD Europhoton Conference (2020), Th-A3.4

5. **L. Beichert**, Y. Binhammer, J. R. Andrade, A. Kniggendorf, B. Roth, and U. Morgner, "Non-collinear Optical Parametric Oscillator for Video Rate Stimulated Raman Spectroscopy of Microplastics," in 2019 Conference on Lasers and Electro-Optics Europe & European Quantum Electronics Conference (2019), CD-2.5

## International conferences, others

1. R. Mevert, Y. Binhammer, C. M. Dietrich, R. C. J. Andrade, **L. Beichert**, T. Binhammer, J. Fan, and U. Morgner, "Femtosecond non-collinear optical parametric oscillator in the visible (VIS-NOPO)," in Conference on Lasers and Electro-Optics (2021), JW1A.12.
2. R. Mevert, Y. Binhammer, J. Fan, T. Binhammer, C. M. Dietrich, J. R. C. Andrade, **L. Beichert**, and U. Morgner "Femtosecond ultra-broadband non-collinear optical parametric oscillator in the visible spectral range (VIS-NOPO)" in 9th EPS-QEOD Europhoton Conference (2020), Tu-P1.5
3. **L. Beichert**, Y. Binhammer, J. R. C. Andrade, A.-K. Kniggendorf, and U. Morgner, "Non-collinear Optical Parametric Oscillator for Video-Rate Stimulated Raman Spectroscopy of Microplastics", in 8th EPS-QEOD Europhoton Conference (2018), WeP.25
4. Y. Binhammer, T. Binhammer, **L. Beichert**, J. R. C. Andrade, A. Tajalli1, and U. Morgner "Scalability of an ultrabroadband non-collinear optical parametric oscillator (NOPO) in the visible", in 8th EPS-QEOD Europhoton Conference (2018), WeP.26

# Curriculum Vitae

## Personal Details

Luise Beichert  
Niddastr. 21  
76229 Karlsruhe

born 5<sup>th</sup> of July, 1988 in Hannover, Germany  
married, 2 children (6 and 8 years old)

## Ph.D. Studies

since 10/2014      **Doctoral Studies**, Leibniz Universität Hannover, research group of Prof. Dr. Uwe Morgner at the Institute of Quantum Optics  
*Focus:* optical parametric oscillators, stimulated Raman spectroscopy, detection of microplastics  
*Award:* Lindemann-Scholarship in recognition of outstanding academic achievements and high potential for scientific innovation in the dissertation project  
*Participation* in the research accompanying program "Promotion plus+ qualifiziert" for the acquisition of management competencies and transferable skills

## Education

10/2011 - 10/2014    **Master of Science** (Physics), Leibniz Universität Hannover  
*Focus:* nonlinear optics, ultrashort laser pulses, thin disk laser  
*Award:* "Deutschlandstipendium" scholarship for talented students with outstanding results during their studies  
*Final grade:* 1.2

10/2008 - 12/2011    **Bachelor of Science** (Physics), Leibniz Universität Hannover  
*Focus:* ultrashort pulse laser  
*Final grade:* 1.7

08/2001 - 07/2008 **Higher Education Entrance Qualification**

Otto-Hahn Gymnasium Springe

*Final grade: 1.7*

## **Professional Experience**

since 06/2022

**IT-Consultant**, TNG Technology Consulting GmbH

Analysis of customer requirements,

Development and optimization of large and complex software systems with high personal responsibility



# Acknowledgements

At last I would like to thank all the people who have supported and accompanied me during my long doctoral period and who have contributed to the success of this work. First of all, I would like to thank my supervisor Uwe Morgner, who gave me the opportunity to work in his group. For me, it was not a matter of course with my newly founded family. Many thank for your belief, guidance and support throughout my PhD journey. Furthermore, I would like to thank Bernhard Roth and Dario Polli for taking over the co-lecture, as well as Prof. Manfred Lein for chairing my examination committee.

Many thanks also to the secretariat, to Mrs. Hünitzsch, Mrs. Pfennig and Mrs. Kaisik. You always helped me with words and deeds and you always kept a cool head in the hustle and bustle of the everyday scientific life. Also a big thanks to Kai-Martin Knaak, who soldered photodiodes together with me in the electronics workshop late at night. As well as to the whole workshop for finishing my parts, sometimes on short call.

A big thank you to the complete workgroup, in which I always felt well. Many thanks to my changing office colleagues Welm, Christian and Robin. For every chat and every encouragement. I thank Jose for his help on the thin disk laser and Christian, Robin and Han for their support and ideas on the NOPO. I thank Sven for his computer assistance, Dmitrii for his bike rides and David for everything I stole from his lab. And thank you to everyone I didn't mention by name, who nevertheless helped me finding my lost measuring head or spectrometer or who accompanied me in the mensa.

I also thank my family for their support. My two children have grown up in this time, from babies to schoolchildren and have let me work sometimes more sometimes less gladly. I thank my parents for their support and all the relief they have given me. I thank my grandma for constantly asking and demanding to finally finish my work. And above all, I thank my husband for accompanying me through this time full of ups and downs.

Thank you all.

